Modeling and Parameter Estimation of Sea Clutter Intensity in Thermal Noise

by

Judith A. Northrop

A Dissertation Presented in Partial Fulfillment
of the Requirements for the Degree
Doctor of Philosophy

Approved March 2019 by the
Graduate Supervisory Committee:

Antonia Papandreou-Suppappola, Chair
Chaitali Chakrabarti
Cihan Tepedelenlioglu
Alexander Maurer

ARIZONA STATE UNIVERSITY

May 2019

ABSTRACT

A critical problem for airborne, ship board, and land based radars operating in maritime or littoral environments is the detection, identification and tracking of targets against backscattering caused by the roughness of the sea surface. Statistical models, such as the compound K-distribution (CKD), were shown to accurately describe two separate structures of the sea clutter intensity fluctuations. The first structure is the texture that is associated with long sea waves and exhibits long temporal decorrelation period. The second structure is the speckle that accounts for reflections from multiple scatters and exhibits a short temporal decorrelation period from pulse to pulse. Existing methods for estimating the CKD model parameters do not include the thermal noise power, which is critical for real sea clutter processing. Estimation methods that include the noise power are either computationally intensive or require very large data records.

This work proposes two new approaches for accurately estimating all three CKD model parameters, including noise power. The first method integrates, in an iterative fashion, the noise power estimation, using one-dimensional nonlinear curve fitting, with the estimation of the shape and scale parameters, using closed-form solutions in terms of the CKD intensity moments. The second method is similar to the first except it replaces integer-based intensity moments with fractional moments which have been shown to achieve more accurate estimates of the shape parameter. These new methods can be implemented in real time without requiring large data records. They can also achieve accurate estimation performance as demonstrated with simulated and real sea clutter observation datasets. The work also investigates the numerically computed Cramér-Rao lower bound (CRLB) of the variance of the shape parameter estimate using intensity observations in thermal noise with unknown power. Using the CRLB, the asymptotic estimation performance behavior of the new estimators is studied and compared to that of other estimators.

To all those who have looked inside to find
the tenacity needed to support their dreams.

And to my family, friends and colleagues,
I could not have completed this degree
without your never ending support.

ACKNOWLEDGMENTS

Without hesitation, I sincerely want to express my deep gratitude to Professor Antonia Papandreou-Suppappola for encouraging my studies and research. This thesis would not be possible without her detailed analysis, recommendations and efforts on my behalf. She has also remained my strongest advocate in representing my needs to the ASU Graduate College. Professor Papandreou-Suppappola's enthusiasm in the field of signal processing and devotion to teaching and her students has truly been inspiring.

I would also like to thank Professors Chaitali Chakrabarti, Cihan Tepedelenlioglu and Alexander Maurer for their interest in my research, and their assistance in serving as members of my supervisory committee.

A very special thank you to both Cynthia Cantrell, Renee Olsen, my daughter Jaclyn and my long time friend Mike McBride for their patience and constant encouragement while supporting me through school, jobs, relocation and all of my endeavors no matter how trying.

Heartfelt thanks are due to Ann Stewart for being so generous with her time while she proctored all of my non-research class exams. I would also like to thank Marty Wishka and Jeff Hansen for their efforts in making sure my tuition reimbursement paperwork and approvals were submitted on time.

I must recognize may colleagues at Northrop Grumman for always showing interest in my work, including Erik Johnson, Stan Zipper, Wes Collier, Catrina Benson, Ken Waring, Kate Klenke, Jean Marie Szakovtis, Pat Neary, Mike Addison, Norm Eng, Ryan Honor, Dan Hare, Andy Ritchie, Don Scheuer, Toni Pardi, Forest Brown, Jake Swanson, Doug Kubo, Justin Hernandez, Bob Peterson, Tim Grasser, Roger Day, Jared Wagner, Jacob Carbajal, Jennifer Britt, David Leopold and Bill Abbley.

Finally, a special thank you to Keith Ward, Robert Tough and Simon Watts for writing the book Sea Clutter: Scattering, the K Distribution and Radar Performance. This textbook provided me with countless hours of study and in-valuable reference for my interest in Sea Clutter.

We acknowledge the help of

- The South African Council for Scientific and Industrial Research, for providing CSIR Sea Clutter and Small Boat Reflectivity databases. The research would not have been possible without the use of this valuable data.

- The Defense Science and Technology Organization DSTO Australia, for providing access to the INGARA system sea clutter database, data collected in Darwin, February 1999. Estimating the parameters of this dataset inspired methods presented in this research.

- McMaster University for providing sea clutter data from the Intelligent PIXel Processing Radar (IPIX) which was positioned along the Grimsby shore line in Ontario, CA for a sea clutter collection campaign, February 1998.

TABLE OF CONTENTS

CHAPTER Page

CHAPTER Page

CHAPTER Page

LIST OF TABLES

Table Page

LIST OF FIGURES

Figure Page

Figure Page

Figure Page

Chapter 1

INTRODUCTION

1.1 Statistical Modeling of Sea Clutter

Fundamental requirements for airborne, ship board, and land based radars operating in maritime or littoral environments include the detection, identification and tracking of targets against an undesirable backscattering caused by the roughness of the sea surface. This backscattering or sea echo reflectivity is often referred to as sea clutter. A characteristic of sea clutter is its spikiness that results from Bragg, whitecap and sea spike scattering [1, 2] and often obscures smaller targets or vessels. This leads to either miss detections or false positives, resulting in degraded radar performance. For this reason, statistical modeling of sea clutter to improve radar performance remains an active area of research. In particular these models are used throughout the engineering design, development, and verification of modern day complex radar systems.

As shown from empirical studies, the sea surface exhibits small and large scale structure components. The small-scale structure or speckle component which are reflections from multiple scatterers with short temporal decorrelation period. The large-scale structure or texture component modulates the speckle component. It accounts for long sea waves that are slowly time-varying and have long temporal decorrelation period [2, 3]. Statistical models based on probability density functions were considered to represent the statistical fluctuations of the amplitude or intensity of the speckle and texture components [4, 5, 6, 7, 8, 9]. A commonly used model is the compound K-distribution (CKD) as it was shown to be a matched fit to sea clutter intensity data under various conditions, including thermal

noise [10, 2].

1.2 ICKD Parameter Estimation Methods

The shape and scale parameters of the intensity-based compound K-distribution (ICKD) have been estimated using the first two intensity moments, assuming known thermal noise power [7]. By also including the third moment, the thermal noise power can be estimated provided very large data sets are available for improved accuracy [2, 10]. Constrained maximum likelihood estimation was also used, but it requires numerical integration and optimization [11]. In [7], windowing and time-averaging of the spectra of sea echo reflectivity in single range-bins was used to estimate the thermal noise power. Methods for estimating all three ICKD parameters include the use of fractional moments that do not require numerical computations [12], and a log-based moment approach that evaluates the resulting nonlinear estimators numerically [13, 14]. A nonlinear curve fitting of the ICKD or the tail of its complementary cumulative distribution function, combined with Nelder-Mead unconstrained nonlinear optimization, was also considered [6, 15, 16]. Though this approach does not require large data sets, it uses non-coherent pulse integration and the required three-dimensional (3-D) search makes it computationally intensive.

1.3 Dissertation Contributions

In this work, two methods are proposed for estimating the parameters of ICKD-modeled sea clutter intensity observations in thermal noise. Marine radar systems cannot avoid the presence of thermal noise as it affects detection performance, especially for small targets. As a result, the effect of thermal noise must be accounted for when modeling sea clutter characteristics to ensure increased radar receiver processing performance [17]. As the thermal noise power cannot always be estimated by averaging Doppler spectra over a sin-

gle range bin [7], more involved methods need to be considered. The goal is to introduce methods that can effectively estimate the ICKD shape, scale and thermal noise power parameters and that can be implemented in real time without requiring a large number of collected sea clutter observations. To that effect, the following summarizes our proposed methods and overall results.

Integration of Integer-based Moments and Nonlinear Curve Fitting: We propose the integrated noise-power estimation intensity moment (NEIM) method for ICKD parameter estimation [18, 19]. This is an iterative method that integrates the estimation of the thermal noise power using 1-D nonlinear curve fitting with the use of the first two integer-based intensity moments to estimate the shape and scale parameters. The method was shown to be about 30 times less computationally intensive than the 3-D curve fitting approach in [6] while maintaining the high estimation accuracy. It also provides more accurate estimation performance than the methods based on integer or fractional intensity moments as, unlike the moment-based methods, it does not require large data records.

CNR Estimated Fractional Intensity Moment: The CNR estimated fractional intensity moment (CEFIM) method [18, 19] is similar to the NEIM approach in that a thermal noise power estimate is iteratively computed to minimize a curve fitting mean-squared error (MSE). However, to obtain the shape parameter estimate, the CNR is first estimated using fractional intensity moments with the thermal noise power estimate.

The performance of the proposed NEIM and CEFIM ICKD-model parameter estimation methods for sea clutter intensity in thermal noise is demonstrated and compared using both simulated ICKD variates and real sea echo reflectivity observations obtained from clifftop radars operating in littoral environments. The computational intensity and estimation MSE performance of the new estimators are also compared using simulated observations and two different sets of sea echo reflectivity.

Cramér-Rao Lower Bounds for the Parameter Estimation and Asymptotic Performance: We provided numerical computation of the Cramér-Rao lower bound (CRLB) for the variance of the ICKD shape parameter estimate for sea clutter intensity observations in thermal noise with unknown power. Using the CRLB, the asymptotic estimation performance behavior of the new estimators is studied and compared to that of other estimators.

1.4 Report Organization

The rest of the dissertation is organized as follows. Chapter 2 reviews the ICKD model with thermal noise, whereas Chapter 3 summarizes the intensity moments, fractional intensity moments, log-based intensity moments and the 3-D nonlinear curve fitting ICKD parameter estimation methods. The new NEIM and CEFIM methods are described in Chapter 4, and Chapter 5 with comparative results provided, both with simulated and real clutter intensity data in the respective chapters.

Note that a list of symbols and abbreviations used throughout the thesis is given in Appendix A.

Chapter 2

COMPOUND K-DISTRIBUTION SEA CLUTTER REFLECTIVITY MODELS

2.1 Introduction to Sea Clutter Models

The detection performance of airborne radars operating in littoral or maritime environments can be impacted by the spikiness of the sea-surface reflectivity or clutter. For this reason, accurate sea clutter models are necessary for the design of radar hardware and signal processing algorithms.

Several probability density functions (PDFs) have been proposed as sea clutter models that can be used with higher resolution low grazing angle radars, including the Rayleigh, log-normal and Weibull [2, 5]. The compound K-distribution (CKD) has been shown to be a well-matched model for sea clutter amplitude statistics. It is a compound distribution that captures both the spikiness and the decorrelation properties of sea clutter returns. Statistical analysis has shown this model to be a good fit to high resolution sea clutter amplitude fluctuations under most conditions [5]. One exception is for horizontally polarized sea clutter reflectivity which exhibits a heaver tail PDF and makes detection more difficult [20, 8]. In addition to accurately modeling sea clutter amplitude statistics, the CKD can also accurately capture both the spatial and temporal correlation aspects of the sea clutter [5]. In addition, this model can be expanded to account for thermal noise. Inclusion of the thermal noise in the model results in an overall increase of the average power of the fast changing speckle component of the distribution [10].

2.2 Statistical Characteristics of Sea Clutter

2.2.1 Sea Scatter and Its Impact on Target Detection

Fundamental requirements for airborne, ship board, and land based radars operating in maritime or littoral environments include the detection, identification and tracking of targets against an undesired backscattering caused by the roughness of the sea surface. Furthermore maritime radars are often required to adapt the target tracking radar parameters as the sea surface changes over a long range, driving the need for accurate environment and sea clutter models. Throughout this thesis, we refer to sea clutter as the radar echo or backscatter from the ocean surface caused by the roughness of the illuminated sea area. This can be further characterized by the wind speed, wind direction, wave speed, fetch, and swell direction. Surface waves can be categorized into capillary of gravity waves [21, 2, 22].

Capillary waves are small ripples that have less than 1.73 cm wavelengths, are modulated by the longer wavelength gravity waves, and are controlled by the surface tension of the sea water. The velocity or propagation of the gravity waves is controlled by gravity, their wavelengths are greater than 1.73 cm, and they are further categorized into sea and swell waves. the sea waves result from a long duration wind blowing over the fetch or large surface area with nearly constant direction and velocity. Swell waves propagate from the local area, and often take the form of long-crested low-frequency sinusoids which can extend over very long distances [21, 1].

In addition to sea waves there are several radar parameters that define the clutter characteristics such as grazing angle, transmit power, carrier frequency, range to the target, area of illumination, polarization, atmospheric and propagation loss, and receiver thermal noise [2, 22, 1, 23].

2.2.2 Scattering from the Ocean Surface

When sea clutter is observed by higher resolution, low grazing angle radars, the backscatter from a single range cell is referred to as a sea spike. This sea spike is non-stationary in time and spatially non-homogeneous, and has been modeled using a non-Rayleigh probability density function. As it can exist for several seconds, it can cause false alarms in Gaussian based detectors [1]. This backscatter from the sea surface primarily consists of three frequency dependent scattering components that are linearly combined and categorized as Bragg, burst and whitecap scattering [2, 24, 25, 26]. Bragg scattering arises from resonate capillary waves caused by many scatters within a range cell accounting for the speckle component of the clutter. It is modeled with Gaussian statistics [2], and can be described by composite surface theory [26]. Burst scattering is caused by the crest of waves before they break, giving rise to a short duration specular reflection or spike. These sea spikes exist for a small fraction of a second, typically 200 ms [2, 24]. Whitecap scattering consists of sea spikes caused by the foamy rough surface of the waves crest before they break. These spike waves do not decorrelate from pulse-to-pulse or with frequency agility [2, 24].

An example of the sea clutter spikes is depicted in Fig. 2.1, which shows the amplitude of a sea clutter observation for a single range bin. The observations are from the CSIR dataset, which consists of sea clutter collected using the Council for Scientific and Industrial Research (CSIR) Fynmeet Clifftop Radar [27]. In particular, the observations are from range bin 58 (corresponding to a range or 3,855.6 m from the radar) of set CFC17-001 of the CSIR database. Note that additional information on the Fynmeet radar parameters are provided in Appendix B. The figure shows examples of the scattering components that appear to be riding on a slow changing mean level or modulation. This combination of modulation and clutter spikes contributes to the non-Gaussian nature of the clutter, often

referred to as *spikiness* [2].

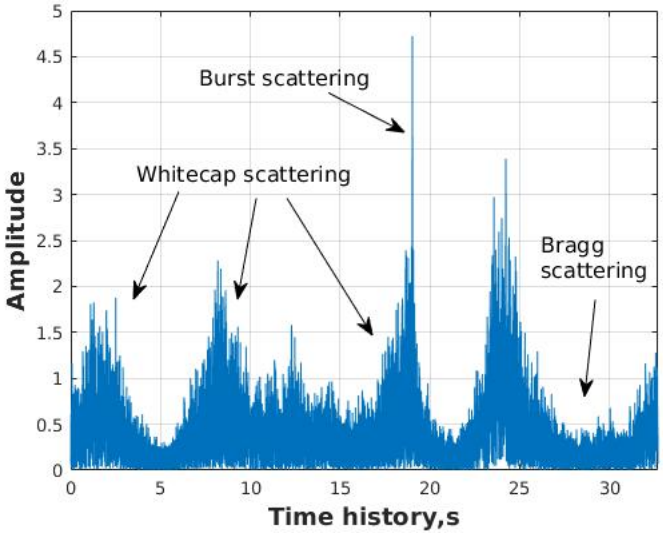

Fig. 2.1: Scattering Components for the Amplitude Response of a Singe Range Bin of Sea Clutter Reflectivity from the CSIR Dataset.

To better understand how an increase in spikiness effects the statistics of the clutter, we provide Fig. 2.2 that compares two different levels of amplitude backscatter using simulated data with unit mean. Fig. 2.2(a) depicts very spiky clutter whereas Fig. 2.2(b) shows clutter that is less spiky and appears to follow a Gaussian distribution.

2.3 Compound K-distribution Model of Sea Clutter Amplitude

The CKD is a compound distribution that is used to model the speckle and texture sea clutter amplitude structures. The speckle is a small-scale structure that accounts for the reflections from multiple scatters with short temporal decorrelation period. The rapid decorrelation is due to the frequency agility or relative motion of the scatters within a cell and it is modeled using a Rayleigh PDF. The texture of local mean level is a large-scale structure tha modulates the speckle component and accounts for the slowly time-varying sea waves and swell [2, 10, 3]. The scatters associated with these long sea waves vary

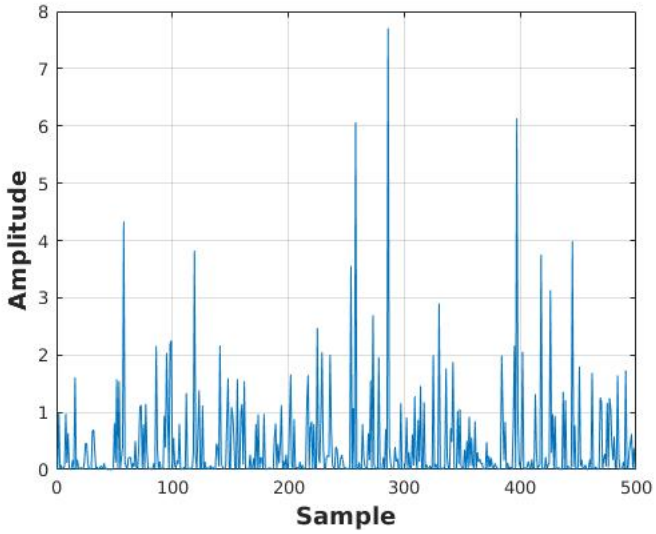

(a)

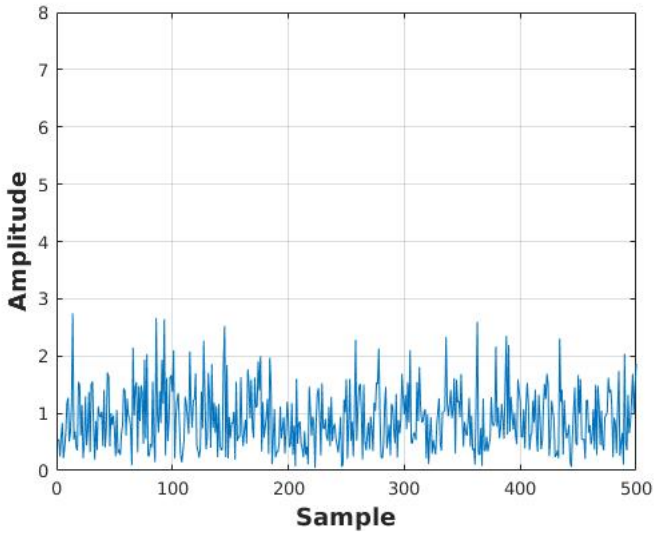

(b)

Fig. 2.2: Clutter Amplitude: (a) Spiky Clutter. (b) Less Spiky Noise Like Clutter.

spatially and have long temporal decorrelation period. The texture amplitude structure is thus modeled using Gamma PDF [2].

Fig. 2.3 shows the amplitude of a single range bin of sea clutter [27]. The sea clutter component is less then 10 ms and it decorrelates, its mean level is changing slowly as it decorrelates in time, in order of several seconds [28, 2]. The CKD amplitude model is characterized by the shape parameter ν and scale parameter b. The shape parameter provides a measure of the amplitude spikiness; the smaller the value of the shape parameter, the sea clutter amplitude is spikier. For high resolution sea clutter, it has been generally observed that the value of the shape parameter ranges from 0.1 to infinity (from very spiky to only thermal noise and no spikes) [29].

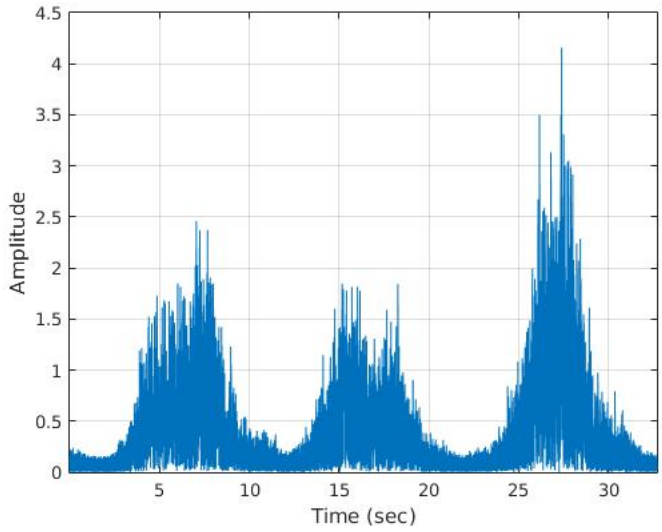

Fig. 2.3: Amplitude Response as a Function of Time of Sea Clutter Reflectivity Obtained from a Single Range-bin from the CSIR CFC17-001 Dataset.

The radar range equation provides the relationship between the received mean level power $p_c = \nu/b$ of sea clutter and the radar transmit power p_t and is given by [2, 30]

$$p_c = \frac{p_t \mu_c G^2 \lambda^2 \sigma^0 A_c}{(4\pi)^3 R^4 L_a L_s}. \tag{2.1}$$

Here, μ_c is the pulse compression gain, G is the antenna gain, λ is the transmitted wavelength, R is the range from the radar to the target, σ^0 is the normalized sea clutter RCS, A_c is the area of illumination, L_a is the atmospheric and propagation loss, and L_s is the system loss. The thermal noise power is defined as

$$p_n = k T_0 B F_n \tag{2.2}$$

where k is the Boltzmann's constant, T_0 is the ambient reference temperature in Kelvin, B is the matched filter bandwidth, and F_n is the radar noise figure accounting for generated received noise above the theoretical thermal noise minimum [2, 30]. Using (2.1) and (2.2), we now define the clutter-to-noise ratio (CNR)

$$\text{CNR} = p_c / p_n. \tag{2.3}$$

The PDF $p_A(a)$ of sea clutter amplitude is given by [2],

$$p_A(a) = \int_0^\infty p(A|x) p_X(x)\, dx, \quad a \geq 0 \tag{2.4}$$

where the speckle component of the PDF for a given texture component x is given by a Rayleigh distribution

$$p(A|x) = \frac{2A}{x} \exp\left(-\frac{A^2}{x}\right). \tag{2.5}$$

The PDF of the texture is given by

$$p_X(x) = \frac{b^\nu}{\Gamma(\nu)} x^{\nu-1} \exp(-bx), \quad x \geq 0 \tag{2.6}$$

where ν is the shape parameter, b is the the scale parameter, $\Gamma(\cdot)$ is the Gamma function. Substituting (2.5) and (2.6) into (2.4) yields the amplitude PDF:

$$p_A(a) = \frac{4b^{(\nu+1)/2}}{\Gamma(\nu)} a^\nu K_{\nu-1}(2a\sqrt{b}), \quad a \geq 0 \tag{2.7}$$

where K_ν is the modified Bessel function.

Fig. 2.4 demonstrates the CKD amplitude model PDF in Equation (2.7) for $b = 1$ and varying shape parameters, 0.3, 1, 3, and 10.

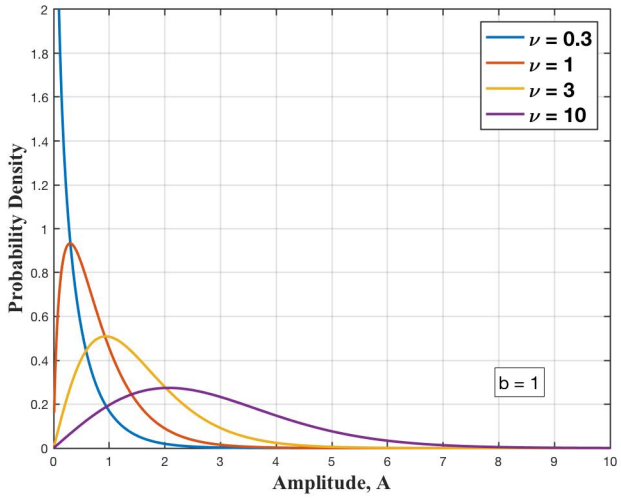

Fig. 2.4: CKD Amplitude Model PDF in (2.7) for Scale Parameter $b = 1$ and for Varying ν.

2.4 Compound K-distribution of Sea Clutter Intensity in Thermal Noise

For realistic scenarios, it is important to consider sea clutter intensity observations in the presence of thermal noise and their corresponding CKD PDF intensity model or ICKD. The ICKD model for clutter intensity $Z = A^2$ is given by

$$p_Z(z) = \int_0^\infty p(z|p_n)p_X(x)dx \tag{2.8}$$

where p_n is the thermal noise power and $p_X(x)$ is given in Equation (2.6). Given a texture value x and a thermal noise power p_n , the conditional PDF of the speckle component can

be defined as [7],

$$p(z|p_n,x) = \frac{1}{p_n+x}\exp\left(-\frac{z}{p_n+x}\right), \quad x \geq 0. \tag{2.9}$$

Combining (2.9), and (2.6), the ICKD model is given by

$$p_Z(z) = \frac{b^\nu}{\Gamma(\nu)}\int_0^\infty \frac{x^{\nu-1}}{p_n+x}\exp\left(-\frac{z}{p_n+x}-bx\right)dx, \quad x \geq 0. \tag{2.10}$$

Note that Equation (2.10) cannot be obtained in closed form and must be solved numerically [2].

The ICKD complementary cumulative distribution function (CCDF) is the probability that a an observation intensity z exceeds a threshold ζ. Specifically, it is given by

$$\Phi(\zeta) = \Pr(Z > \zeta) = \int_\zeta^\infty p_Z(z)dz \tag{2.11}$$

Equation (2.10) also defines the probability of false alarm P_{FA} or probability that a radar target is assumed present even though the observations only include noisy sea clutter intensity data [31, 7].

2.5 Modified Compound K-distribution Models

2.5.1 ICKD for Non-coherent Sum of Pulses

For radar systems that use non-coherent pulse integration, the speckle PDF for a given texture x and N pulses is given by,

$$p(r|x) = \frac{r^{N-1}}{(p_n+x)^N(N-1)!}\exp\left(-\frac{r}{p_n+x}\right), \quad x \geq 0 \tag{2.12}$$

where $r = \sum_{i=1}^{N} z_i$. The resulting P_{FA} for this system is given by

$$\Pr(R > r) = \frac{1}{(N-1)!} \int_0^\infty \Gamma\left(N, \frac{r}{p_n + x}\right) p_X(x) dx \tag{2.13}$$

where $\Gamma(\cdot,\cdot)$ is the incomplete Gamma function and $p_X(x)$ provided with (2.6) [2].

2.5.2 Distribution for Horizontally Polarized Sea Clutter Reflectivity

It has been shown that the CKD model does not provide a good fit to horizontally polarized sea clutter reflectivity which exhibits a heaver tail PDF [20, 8]. To address this shortcoming of the CKD model, the KK-distribution, which is the sum of two compound K-distributions, has been shown to provide a better fit to the tail of the P_{FA}, especially for regions less than 10^{-3} [32]. The KK-distribution has been adapted to include thermal noise [33] and is given by

$$Q(z, p_n) = (1 - k_r) P_1(z; \nu_1, b_1, p_n) + k_r P_2(z; \nu_2, b_2, p_n) \tag{2.14}$$

with $P_i(z; \nu_i, b_i, p_n), i = 1, 2$ correspond to the ICKD PDF in (2.10) with corresponding parameters ν_i, b_i and p_n. Note that the KK-distribution in (2.14) has six parameters. Using real sea clutter observations, the authors in [32, 33] determined $k_r = 0.01$ and reduced the number of parameters to four by selecting $\nu = \nu_1 = \nu_2$. The authors also observed the ratio $\rho_\mu = b_2/b_1$ to be > 1 and determines the degree of separation between the two distributions, whereas the k_r ratio determines the point of and degree of separation.

Chapter 3

COMPOUND K-DISTRIBUTION MODEL PARAMETER ESTIMATION METHODS FOR SEA CLUTTER INTENSITY

3.1 Introduction

The estimation of sea clutter intensity model parameters remains an active area of research, as it is essential to improve the processing of today's complex radar systems in the presence of clutter. It is also necessary to understand the sea surface environment when detection algorithms need to discriminate a target from a spike in sea clutter. There are several methods for estimating the intensity-based compound K-distribution (ICKD) shape and scale parameters some of which are extended to include the thermal noise power [2, 4, 5, 6, 10]. These methods include the use of integer, fractional, or log-based intensity moments [4, 14, 34, 35, 36, 37], and nonlinear least squares curve fitting methods [2, 6, 10, 16, 38, 12].

3.2 K-distribution Shape Parameter Estimation

The focus of our research is to estimate the K-distribution parameters from received sea clutter reflectivity, and we address a few methods that are frequently used. Before doing so, we need to point out that there are also models that can be used to predict radar performance. It is often necessary to understand how a radar performs in relation to the data collection environment and geometry before investing in engineering development. In particular, empirical models were developed for reasonable values of the shape parameter ν of the ICKD model based on a specified radar scene. One such empirical model that can

be used for grazing angles ϕ_{gr} in the range 0.1° to 10.0° is [2, 39]

$$\log_{10}(\nu) = \frac{2}{3}\log_{10}(\phi_{gr}) + \frac{5}{8}\log_{10}(A_c) - k_{pol} - \frac{\cos(2\theta_s)}{3} \tag{3.1}$$

where A_c is the radar resolved area, k_{pol} is the radar transmit and receive polarization parameter, taken to be 1.39 for vertical polarization (VV) and 2.09 for horizontal polarization (HH), and θ_s is the aspect angle with respect to swell direction, which can be omitted if there is no swell.

Equation (3.1) clearly shows that the amplitude or spikiness of the clutter is impacted by the radar collection parameters, in addition to the direction of the sea swell. Other models have been published that factor in swell in the up, down or cross directions; however, these models do not incorporate wind direction or sea state (wave height), and thus include spiky clutter observed for all sea states [2].

3.3 Intensity Moments Method

3.3.1 Thermal Noise Power Estimation Using Higher Order Moments

The intensity moment (IM) method is commonly used to estimate the shape parameter ν and scale parameter b, assuming that the thermal noise power is known [2]. The method uses the first two ICKD moments, $\mu_k = E[Z^m]$, $m = 1, 2$, as they can be obtained in closed form in terms of the two unknown parameters. Here, $E[\cdot]$ denotes statistical expectation. Specifically, for a known thermal noise power p_n, the two moments are given by [2, 7]

$$\mu_1 = \frac{\nu}{b} + p_n \tag{3.2}$$

$$\mu_2 = \frac{2}{b^2}\,\nu(\nu+1) + \frac{4}{b}\,p_n\,\nu + 2\,p_n^2. \tag{3.3}$$

For independent and identically distributed intensity samples z_k, $k = 1, \ldots, N_s$, the mth sample moment estimate is

$$\hat{\mu}_m = \frac{1}{N_s} \sum_{k=1}^{N_s} z_k^m \tag{3.4}$$

Solving (3.2) and (3.3), and using the sample moments, the shape and scale parameters can be estimated in closed form as

$$\hat{\nu} = \frac{2(\hat{\mu}_1 - p_n)^2}{\hat{\mu}_2 - 2\hat{\mu}_1^2} \tag{3.5}$$

$$\hat{b} = \frac{\hat{\nu}}{\hat{\mu}_1 - p_n}. \tag{3.6}$$

In order to also estimate the thermal noise power p_n, the third ICKD intensity moment,

$$\mu_3 = \frac{6\nu(\nu+1)(\nu+2)}{b^3} + \frac{18p_n\nu(\nu+1)}{b^2} + \frac{18p_n^2\nu}{b} + 6p_n^3, \tag{3.7}$$

can be combined combined with μ_1 and μ_2 in (3.2) and (3.3) [10, 2, 13]. Solving three equations with three unknowns yields

$$\hat{\nu} = \frac{18\left(\hat{\mu}_2 - 2\,\hat{\mu}_1^2\right)^3}{\left(12\,\hat{\mu}_1^3 - 9\,\hat{\mu}_1\,\hat{\mu}_2 + \hat{\mu}_3\right)^2} \tag{3.8}$$

$$\hat{p}_n = \hat{\mu}_1 - \sqrt{0.5\,\hat{\nu}\left(\hat{\mu}_2 - 2\,\hat{\mu}_1^2\right)} \tag{3.9}$$

$$\hat{b} = \frac{\hat{\nu}}{\hat{\mu}_1 - \hat{p}_n} \tag{3.10}$$

Using the three estimates and (3.2), the clutter-plus-noise ratio (CNR) $\eta = (\nu/b)/p_n$ can be obtained as

$$\hat{\eta} = (\hat{\nu}/\hat{b})/\hat{p}_n = \frac{\hat{\mu}_1 - \hat{p}_n}{\hat{p}_n}. \tag{3.11}$$

Note that, although the IM is easy to implement, it requires a large number of observations to obtain accurate estimates [2, 10].

3.3.2 Thermal Noise Estimation Using Time-frequency Methods

As noted in the previous section, large sample sizes are required to obtain accurate estimates of the shape parameter when using the first three intensity moments in Equation (3.8). If the thermal noise power is known, the shape and scale parameters can be estimated using the first two moments in Equations (3.5) and (3.6). As was shown in [18], this increases the estimation accuracy of the shape parameter. In [7], a method was considered for estimating the thermal noise power that did not involve higher intensity moments. This method uses the short-time Fourier transform (STFT) time-frequency representation (TFR) to find regions of minimum spectral time-variation. The thermal noise power p_n is then estimated by time-averaging the STFT over these spectral regions.

The TFR-based method is demonstrated in Fig. 3.1(a) that depicts the spectrogram (magnitude-squared of the STFT) TFR of coherent clutter data obtained from the CSIR CFC17-001 range-bin 1 (RB 1). The TFR is shown zoomed in to the region -500 to 500 Hz to emphasize the time changing Doppler spectra. The figure shows clutter spectral regions both with low and high time-frequency variation. As shown with the averaged power spectrum in Fig. 3.1(b), the region between -2,500 and -2,000 Hz exhibits very low time-frequency variation. A different, and less accurate estimate would be obtained if we considered frequencies between -2,000 and -1,500 Hz. In this example the STFT was obtained using the fast Fourier transform (FFT) and a Taylor window. Although different types of windows can be used to compute the STFT [40], we use the Taylor window because it is comparable to the optimal Dolph-Chebyshev window used in [7]. Unlike this optimal window, the Taylor window is realizable and used frequently in practice [21, 41, 42]. The Taylor window parameters include the length of the window N_T, the number of nearly constant sidelobes levels adjacent to the mainlobe $\bar{n}$, and the maximum sidelobe level (in dB) relative to the mainlobe *SLL*. The parameters used for this example include a length

512 FFT, $N_T = 64, \bar{n} = 4$ and $SLL = -55$.

The STFT window and its duration must be carefully selected as they can affect the estimation performance of the thermal noise power. The importance of the selection of the duration of the STFT window is demonstrated using simulated clutter data (as in [7]). We simulated coherent correlated clutter data with a shape parameter of $\nu = 0.1$ and 0 dB CNR (corresponding to $p_n = 0.5$). The time-averaged STFT in Fig. 3.2(a) was obtained using a Taylor window with very short duration $N_T = 2$; the window is thus very broad in the frequency domain. A longer Taylor window, with $N_T = 64$ (and thus narrower in frequency) is used in Fig. 3.2(b). Comparing the two time-averaged STFT power spectra in Fig. 3.2, a different estimate of the thermal noise power is obtained in each case when the region between -2,500 to -2,000 Hz is selected.

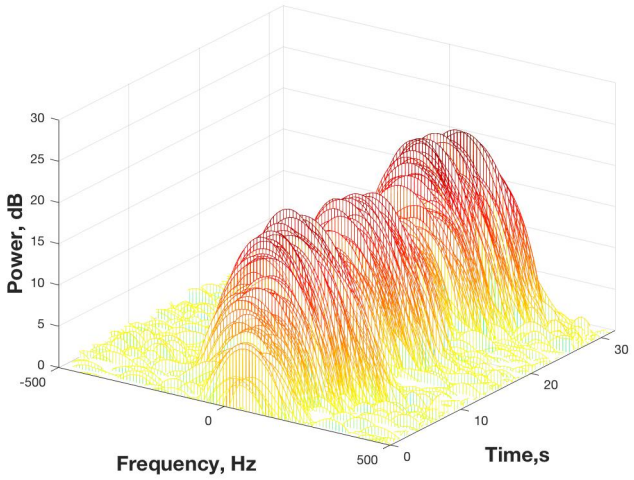

(a)

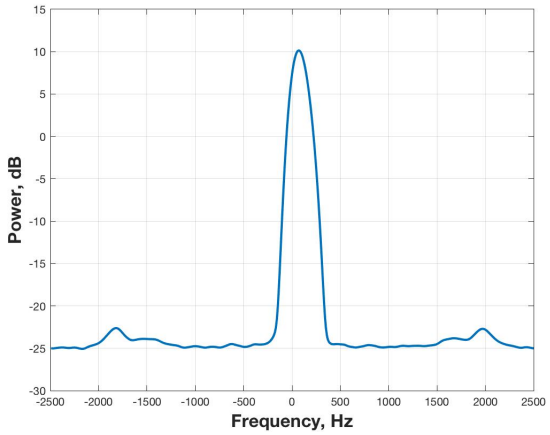

(b)

Fig. 3.1: (a) STFT of clutter data CFC17-001 (RB 1); (b) Time-averaged Power Spectrum Over the Spectral Region Selected Using the STFT.

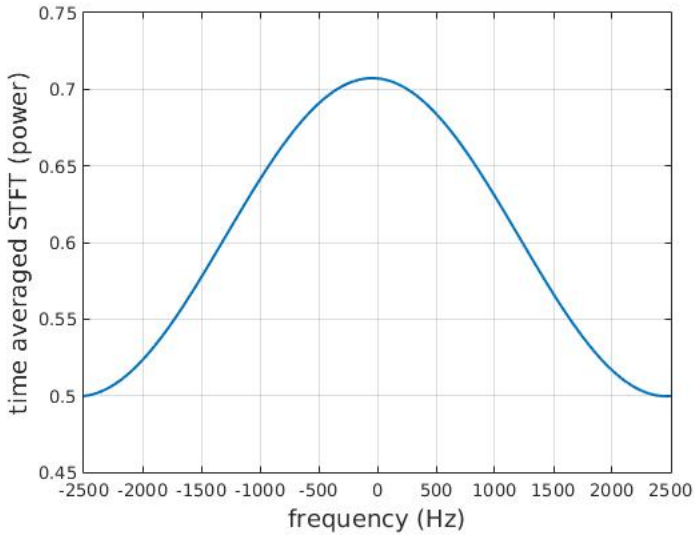

(a)

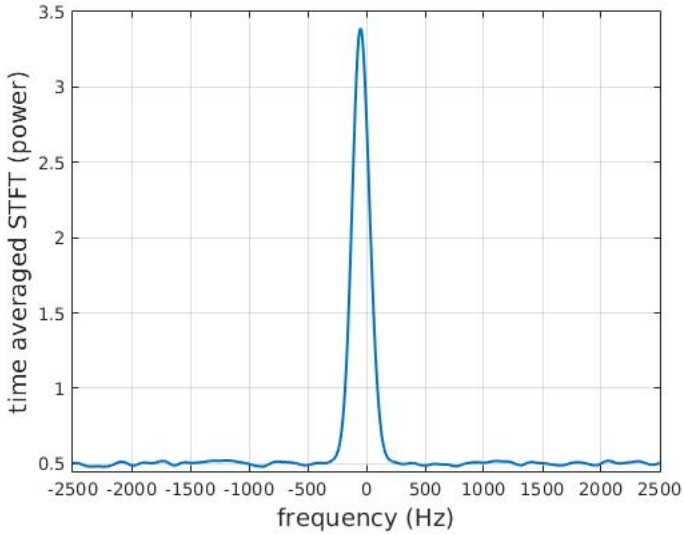

(b)

Fig. 3.2: Time-averaged STFT Power Spectrum using Simulated Clutter with $\nu = 0.1$, CNR ≈ 0 dB; (a) Taylor Window with Length $N_T = 2$. (b) Taylor Window with Length $N_T = 64$.

3.4 Fractional Intensity Moments Method

Instead of using the higher order intensity moments in (3.2) and (3.3), fractional intensity moments (FIMs) were used in [12] to obtain a closed form estimate of the shape parameter. The method is based on the effective shape parameter value, ν_{eff}, that corresponds to the ICKD shape parameter estimate in (3.5) with $p_n = 0$, that is, when it is assumed that no thermal noise is present in the data. The ICKD with no noise and shape parameter ν_{eff} is approximated by an ICKD with shape parameter ν and a given CNR η [10, 2, 12]. Using this approximation, the effective shape parameter is given by

$$\nu_{\text{eff}} = \nu\Big(1+\frac{1}{\eta}\Big)^2 = \frac{2\,\hat{\mu}_1^2}{\hat{\mu}_2 - 2\hat{\mu}_1^2} \tag{3.12}$$

where $\hat{\mu}_1$ and $\hat{\mu}_2$ are the first and second sample moment estimates in (3.4). The method also uses the FIM ratios

$$\alpha_{\rho,q} = \frac{\mu_{(\rho+q)}}{\mu_\rho\,\mu_q}, \quad \beta_{\rho,q} = \frac{\mu_{(\rho-q)}\,\mu_q}{\mu_\rho}, \tag{3.13}$$

for $\rho \in \mathbb{R}^+$ and $q \in \mathbb{Z}$, that can be shown to be independent of the scale b and thermal noise power p_n values. Combining (3.12) and the FIM ratios in (3.13) with $q = 1$, the shape parameter estimate is given in closed form as

$$\hat{\nu} = \frac{\nu_{\text{eff}}\left(1-\rho\,\hat{\beta}_{\rho,1}\right)^2}{\left(\dfrac{\nu_{\text{eff}}}{\rho}\Big(\dfrac{1}{(\rho+1)}\,\hat{\alpha}_{\rho,1}-1\Big)-\rho\,\hat{\beta}_{\rho,1}\right)^2}, \tag{3.14}$$

where $\hat{\alpha}_{\rho,1}$ and $\hat{\beta}_{\rho,1}$ are obtained using (3.13) and the sample moment estimates $\hat{\mu}_{\rho+1}$, $\hat{\mu}_{\rho-1}$, and $\hat{\mu}_\rho$ in (3.4). As shown in [12], the estimated shape parameter in (3.14) has a lower mean-squared error (MSE) when compared to the one obtained using the IM in (3.8). Using (3.12), the CNR estimate is

$$\hat{\eta} = 1/(\sqrt{\nu_{\text{eff}}/\hat{\nu}}-1)\,. \tag{3.15}$$

Using this value and the relation $\hat{\eta} = (\hat{\mu}_1 - p_n)/p_n$, an estimated value of the thermal noise power can be obtained as $\hat{p}_n = \hat{\mu}_1/(1+\hat{\eta})$ and the scale b can be estimated using (3.6).

3.5 Log-based Intensity Moments Method

If the thermal noise power is assumed known, and with multiple number of pulses integrated, an accurate estimate of the shape parameter can be obtained using the first moment and the first moment of the logarithm of the observations [14]. This also assumes that the samples of the speckle component are independent from pulse to pulse. The thermal noise parameter is also estimated using log-based intensity moments (LIMs) in [12]. For a single-pulse system with unknown thermal power, the effective shape parameter in (3.12) is used to estimate the shape parameter $\hat{\nu}$ by solving

$$\frac{\psi_1}{\mu_1} - \xi_1 = 1 + \frac{1}{\sqrt{\hat{\nu}\nu_{\text{eff}}}}\left(1 - {}_2F_0\left(\hat{\nu}, 1; \, ; h(\hat{\nu}, \nu_{\text{eff}})\right)\right) \tag{3.16}$$

where $h(\hat{\nu}, \nu_{\text{eff}}) = -\left(\sqrt{\hat{\nu}\nu_{\text{eff}}} - \hat{\nu}\right)^{-1}$, ${}_2F_0 = (a, b; \, ; z)$ is a hypergeometric function [13], and the LIMs are given by

$$\psi_1 = \int_0^\infty z \log(z)\, p_Z(z)\, dz, \quad \xi_1 = \int_0^\infty \log(z)\, p_Z(z)\, dz \tag{3.17}$$

that can be computed as log-based sample moments. Although both the LIM and FIM estimates $\hat{\nu}$ in (3.16) and (3.14), respectfully, achieve similar MSE estimation performance, the LIM is computationally more intensive than the FIM as it requires numerical zero or root finding methods [12].

3.6 3-D Nonlinear Curve Fitting Method

The nonlinear curve fitting (NCF) method performs a three dimensional (3-D) search to obtain an estimate of the three parameters of the ICKD model in (2.10) [6, 15, 16]. The method is based on fitting the mathematical form of the complementary cumulative

distribution function (CCDF) of Z to simulated sea clutter intensity observations. Using vector notation for the three parameters, $\boldsymbol{\theta} = [\nu \; b \; p_n]$, the CCDF is obtained as

$$\Phi_Z(z;\boldsymbol{\theta}) = \Pr(Z > z;\boldsymbol{\theta}) = \int_z^{\infty} p_Z(\zeta;\boldsymbol{\theta})\, d\zeta\,. \tag{3.18}$$

For a detection statistic $\mathscr{L}(Z)$ that is distributed as in (3.18), a threshold value can be obtained for a given probability of false alarm $\mathrm{P_{FA}}$ using $\mathrm{P_{FA}} = \Phi_Z(\mathscr{L}(z);\boldsymbol{\theta})$ [31, 7]. When a very small value of $\mathrm{P_{FA}}$ is selected, the approach avoids fitting the CCDF tail to regions where the clutter is very spiky [6].

Mean-normalized intensity observations, z_k, $k = 1,\ldots,N_s$ are first used to form simulated CCDF values. The Nelder-Mead unconstrained nonlinear optimization method was selected to numerically obtain the estimated parameters; this is an iterative approach that minimizes the residuals between the model and simulated CCDFs [6, 15, 16]. At each iteration, a 3-D parameter vector estimate of $\boldsymbol{\theta}$ is obtained. Using some convergence tests as iteration stopping criteria, a global minimum is determined that minimizes the overall curve fitting MSE using,

$$\hat{\boldsymbol{\theta}}^{(i)} = \arg\min_{\hat{\boldsymbol{\theta}}^{(i)}} \mathscr{E}_Z(\hat{\boldsymbol{\theta}}^{(i)}), \tag{3.19}$$

where $\mathscr{E}_Z(\hat{\boldsymbol{\theta}}^{(i)})$ is a goodness of fit measure or a curve fitting MSE at the ith iteration given by

$$\mathscr{E}_Z(\hat{\boldsymbol{\theta}}^{(i)}) = \frac{1}{M}\sum_{m=1}^{L-M}\left(\Phi_Z^{\mathrm{sim}}(z_m) - \Phi_Z(z_m;\hat{\boldsymbol{\theta}}^{(i)})\right)^2, \tag{3.20}$$

with L being the length of the CCDF and M the number of selected CCDF values to avoid fitting points in the upper tail where the fit will be poor [6]. Note that only M out of L distribution points are used in (3.20).

Fig. 3.3 outlines the NCF algorithm flow. A summary of the NCF steps is provided in Algorithm 1. The input to the NCF algorithm includes the mean-normalized intensity observations ζ_m and an initial starting estimate for $\boldsymbol{\nu}^{(0)}$, $b^{(0)}$, $p_n^{(0)}$. The algorithm defines a stopping criteria based on the convergence of the estimates MSE. At the i iteration, the stopping criteria is computed as $|\mathscr{E}_Z(\hat{\boldsymbol{\theta}}^{(i+1)}) - \mathscr{E}_Z(\hat{\boldsymbol{\theta}}^{(i)})| < \varepsilon_F$, where $\mathscr{E}_Z(\hat{\boldsymbol{\theta}}^{(i)})$ is defined in Equation (3.20) and ε_F is the smallest difference that can be added to a floating point number provided in Table 3.2.

The minimization approach we employ is the simplex search method from Reference [43]. This is a search that is based on minimizing unconstrained multivariable functions without computing derivatives. In MATLAB; this method is implemented using the function fminsearch; this function allows for a minimal function tolerance, minimal step size, and the maximum number of iterations as termination criteria as described in Table 3.1.

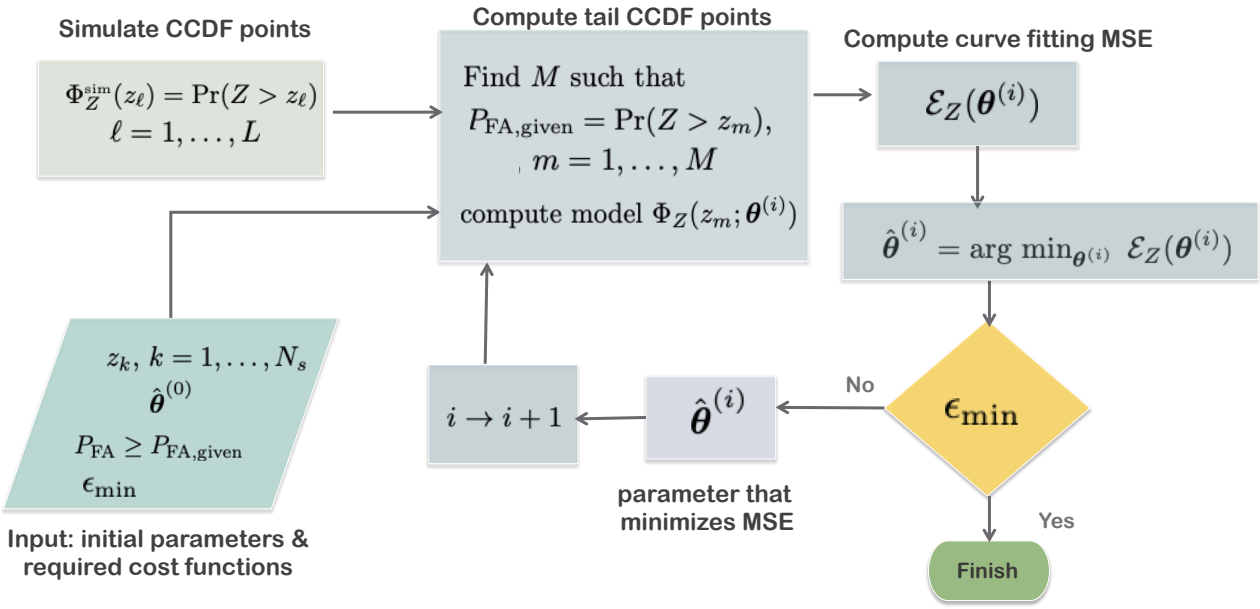

Fig. 3.3: Flowchart of iterative Nonlinear Curve Fitting (NCF) Using the Nelder-Mead Three Dimensional Search Algorithm.

Algorithm 1: Iteration steps of 3-D NCF

- Input: Initial estimate $\hat{\boldsymbol{\theta}}^{(0)}$, mean-normalized intensity observations, z_k, $k = 1, \ldots, N_s$, function tolerance ε, $P_{\text{FA}} \geq 0.003$
- Using z_k, simulate $\Phi_Z^{\text{sim}}(z_\ell)$, $\ell = 1, \ldots, L$, using the intensity data provided; this is simulated as $\Phi_Z^{\text{sim}}(z_\ell) = \Pr(Z > z_\ell)$
- Obtain M (out of L), the number of tail CCDF points, as the number of intensity samples z_m such that $P_{\text{FA}} \geq 0.003$, where $P_{\text{FA}} = \Pr(Z > z_m) = \Phi_Z^{\text{sim}}(z_m)$
- At the ith iteration, $i = 0, \ldots, I_{\max}$, compute the tail M modeled CCDF points $\Phi_Z(z_m); \boldsymbol{\theta}^{(i)}$, $m = 1, \ldots, M$ using $\Phi_Z(z; \boldsymbol{\theta}) = \int_z^\infty p_Z(\zeta; \boldsymbol{\theta})\, d\zeta$, where $p_Z(\zeta; \boldsymbol{\theta})$ is the ICKD model PDF with parameter vector $\boldsymbol{\theta}$. Also, $\boldsymbol{\theta}^{(i)}$ are all allowable vector values of $\boldsymbol{\theta}$ over which the search is performed
- Compute the curve fitting MSE as $\mathscr{E}_Z(\boldsymbol{\theta}^{(i)}) = \frac{1}{M} \sum_{m=1}^{L-M} \left(\Phi_Z^{\text{sim}}(z_m) - \Phi_Z(z_m; \boldsymbol{\theta}^{(i)}) \right)^2$
- Find $\hat{\boldsymbol{\theta}}^{(i)}$ that minimizes the curve fitting MSE, $\hat{\boldsymbol{\theta}}^{(i)} = \arg\min_{\boldsymbol{\theta}^{(i)}} \mathscr{E}_Z(\boldsymbol{\theta}^{(i)})$
- Stopping criteria: for a given ε, stop iteration when $|\mathscr{E}_Z(\hat{\boldsymbol{\theta}}^{(i+1)}) - \mathscr{E}_Z(\hat{\boldsymbol{\theta}}^{(i)})| < \varepsilon_F$

3.7 Simulation Environment and Algorithm Parameters

3.7.1 Simulated Data

For simulating stationary uncorrelated sea clutter intensity observations, we first generated the gamma distributed variable X using the inverse incomplete gamma function whose lower tail is given by $X = \gamma(\nu, q) = (1/\Gamma(\nu)) \int_0^q t^{\nu-1} e^{-t} dt$. Here, q is obtained from a set of uniformly distributed samples between $[0,\ 1]$, ν is the ICKD shape parameter and $\Gamma(\cdot)$ is the gamma function. Using the methods of generating non-uniform random values from [44, 2], the ICKD variable is obtained as the product of the gamma and exponential random variables $Z = \sqrt{-bA \log(R)}$ [35]. Here, R is obtained as q, $A = \gamma^{-1}(\nu, q)$, and b is the ICKD scale parameter. The ICKD amplitude data set is then converted to coherent data with random phase and additive complex zero-mean Gaussian noise to achieve the desired CNR. Unless otherwise stated, $N_s = 10,000$ intensity observations were generated and averaged over 1,000 Monte-Carlo (MC) simulations. The number of simulated points M to fit the CCDF tail was selected to satisfy $P_{FA} \geq 0.003$ in order avoid fitting very spiky clutter [6].

3.7.2 Processor

Our testing configuration is a Mac-Book Pro, running macOS 10.13 with an Intel i7 2.8 GHz processor, and MATLAB R2017a. To improve execution time for both search methods, we implemented (2.10) using MATLAB'S mex API.

3.7.3 Algorithm Termination Criteria

To make direct comparisons of the tested algorithms, we need to understand the termination criteria for each method. We will be comparing a total of three 1-D search methods for use in our proposed NEIM method, and three 3-D NCF methods for direct comparison with the NEIM method. For the six methods tested, the termination criteria will contain some combination of criteria in Table 3.1.

Symbol	Description
ΔX	Step tolerance which is the lower bound on the function step size or, $\lvert x_i - x_{i+1}\rvert < \varepsilon_X$ and is depicted as Step Tolerance in Fig. 3.4
ΔF	Function tolerance which is the lower bound on the change of the evaluated function $f(x)$ or $\lvert f(x_i) - f(x_{i+1})\rvert < \varepsilon_F$ and is depicted as Function Tolerance in Fig. 3.4
MF	Maximum number function evaluations or calls to $f(x)$

Table 3.1: Algorithm Termination Criteria

Fig. 3.4 depicts how both the step and function tolerance is evaluated for a proposed function $f(x)$. For the 1-D search methods $f(x)$ is provided with Equation (4.1) and Equation 3.20 for the 3-D search. For the algorithms that use both step tolerance and function tolerance, the algorithm will terminate if either of the minimum thresholds is reached.

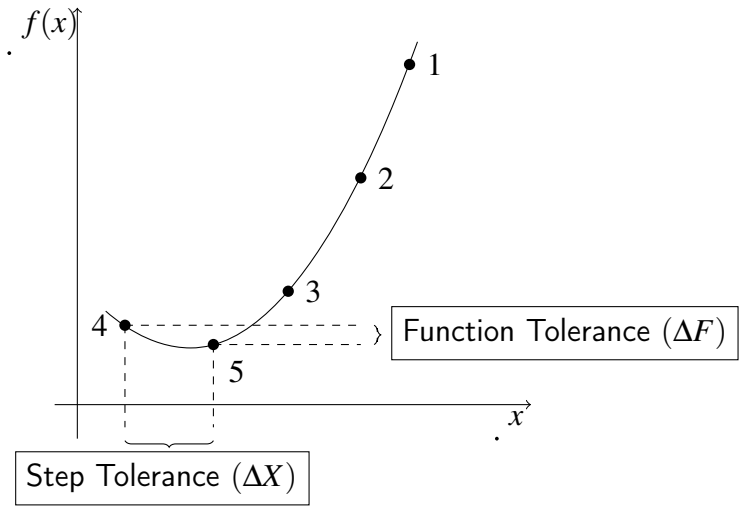

Fig. 3.4: Algorithm Termination Tolerance for the Step Tolerance (ΔX) and Function Tolerance (ΔF). Similar to MATLAB Tolerance and Stopping Criteria Documentation.

3.7.4 Simulated Data Sample Size and Minimum Usable CCDF Levels

A main consideration of using curve fitting methods to estimate the K-distribution parameters is to obtain the estimates using smaller sample sizes. As a result, we need to be careful in fitting the model distributions to the CCDF obtained from the clutter data and not fit the regions at the tail of the distribution where we have few samples that contribute to the CCDF. In [6] the authors recommend setting this level to 10^{-2} for using a sample size of 1,000 samples. Fig. 3.5 depicts the log of CCDF curves for sample sizes $N_s = [10^4, 10^5, 10^6, 10^7]$ using a shape parameter $\nu = 0.1$ and CNR = 5 dB. Except where noted in Section 4.4.4, we will be using $N_s = 10,000$ for all simulations, therefore we will fit the CCDF curves down to a level of 10^{-3}

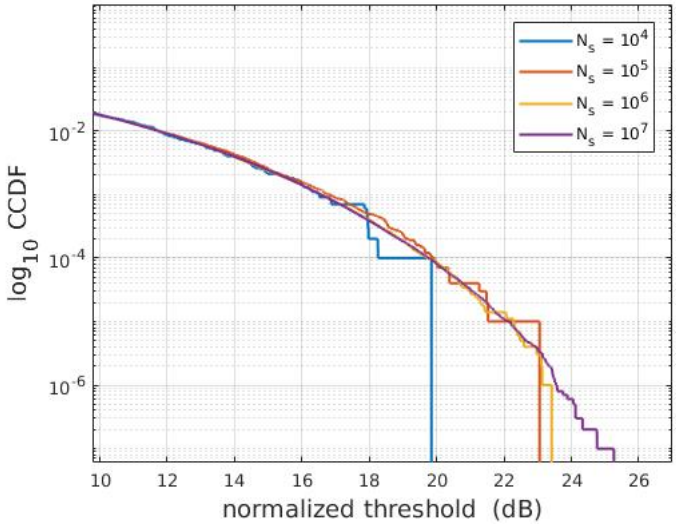

Fig. 3.5: Comparison of CCDF Levels for Simulated K-distribution Clutter Different Sample Lengths (N_s).

3.7.5 Tested CNR Levels

To evaluate both one and three dimensional search algorithms, we will estimate the K-distribution parameters while also gathering performance metrics while sweeping a range of CNR levels. In [6] the authors test CNR levels of -5 dB, 0 dB and 10 dB so for comparison we will extend these levels to include a CNR level of 20 dB. We will see in a following section, that a CSIR Fynmeet Radar dataset will have a CNR of approximately 20 dB for different range-bins of sea echo reflectivity, therefor we need to include this level in our algorithm evaluations.

Unless otherwise stated, we will be using the values in Table 3.2 for all algorithm comparisons

Symbol	Description	Value
N_s	Number of sea clutter samples	10,000
L	Number of CCDF distribution points	2,048
MC	Number of Monte-Carlo simulations	1,000
ε_X	Step size stopping criteria	10^{-4}
ε_F	Function difference stopping criteria	10^{-8}
$I_{\max}$	Maximum number function evaluations	5,000

Table 3.2: Algorithm Run-time Values

3.8 Three Dimensional Search (Nelder-Mead) Algorithm Comparisons

The multi-dimensional Nelder-Mead (NM) search methods seek to find a minimum value for functions containing multiple parameters. For estimating K-distribution clutter parameters, we will be using the NM to minimize a function with three variables. We will compare three different implementations of the NM to understand the performance of each method. For the implementations compared, we need to provided an initial guess of the parameters $\hat{\nu}_0, \hat{b}_0, \hat{p}_{n,0}$ which we initialize to $[0.1, 0.1, 0.1]$. Testing will show these values produce stable results for the compared methods across the tested CNR. The methods evaluated are:

MATLAB fminsearch**:** Is a unconstrained minimum search which uses the Nelder-Mead simplex search as described in [43]. For a two dimension search, the simplex can be defined by the vertices of a triangle. For a three dimension search, the vertices define a tetrahedron. In addition to the initial estimate of the parameters, the method accepts ε_X, ε_F and MF to control the termination criteria.

Mathews, Nelder-Mead: Is a simplex search method with MATLAB implementation provided in [45]. Our implementation accepts ε_X, ε_F. We made slight modifications to this method to allow for the ε_X termination criteria to exit when ΔX is minimized, and to return the total function count. Also, this method accepts as input the initial starting simplex as opposed to an estimate of the initial parameters. We implemented a method to obtain this simplex from the initial parameters as described by L. Pfeffer at Stanford (reference has not been identified) and outlined here [46].

O'Neill, Nelder-Mead: This simplex search method is defined in [47] and our MATLAB implementation was provided with [48]. In addition to the initial estimate of the parameters, the method accepts ε_F and MF for the termination criteria. This method does not use ε_X

to control termination. We made a slight modification to this method to return the total function count.

Fig. 3.6(a) compares the estimated shape parameter $\hat{\nu}$ for the three, 3D search methods and note they all achieve comparable results where the fminsearch method provides the best performance for CNR in the range of -5 to 0 dB with the Mathews method being unstable in the -5 to -3 dB range. All methods diverge from the actual parameter value of $\nu = 0.1$ beginning at a CNR of 12 dB. Fig. 3.6(b) compares the estimated noise parameter $\hat{\rho}_n$ and we compare the algorithm results with the value used to generate the simulated clutter and note that all three methods achieved almost identical results with the exception of where the Mathews method is unstable in the region of -5 to -4 dB.

Fig. 3.7(a) compares the total number of function evaluations and its easy to see, the O'Neill method requires more evaluations in the CNR region of -5 to 7 dB, and this could be related to not including ΔX as a termination criteria. We also note that the Mathews method completes in less time than both the O'Neill and fminsearch methods. Fig. 3.7(b) shows the CT performance and the behavior of the results are understandable considering the number of function evaluations depicted in Fig. 3.7(a). Fig. 3.8 shows the CCDF MSE performance for the compared algorithms with the fminsearch method having and overall lower CCDF MSE throughout the tested CNR region with the exception of the spike at -5 dB.

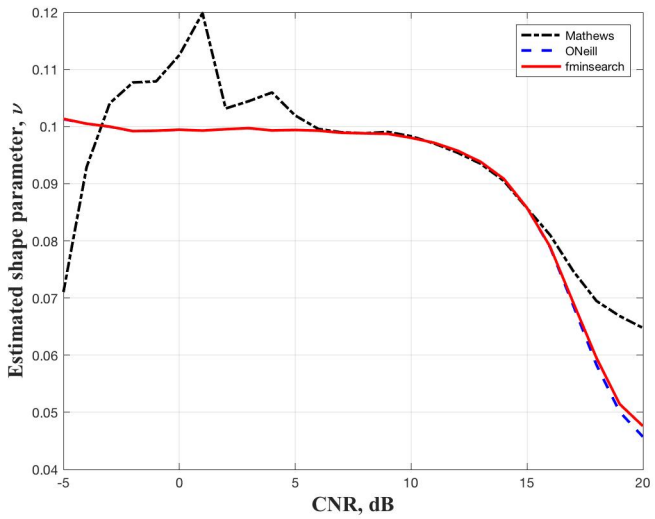

(a)

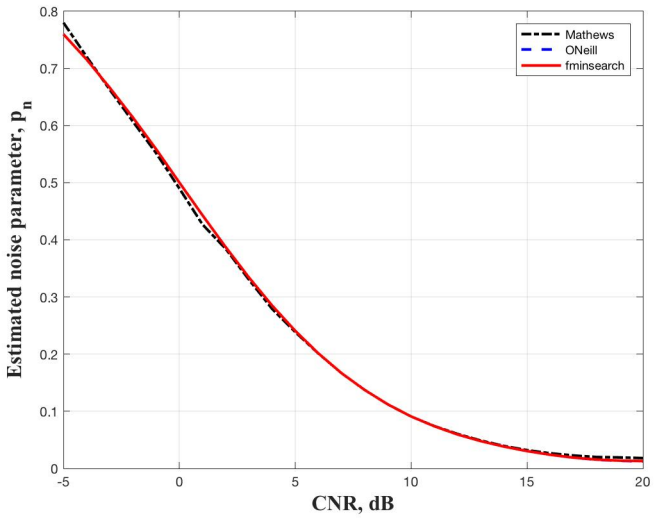

(b)

Fig. 3.6: Comparison of the Three 3-D Search Methods Using Simulated Data with Increasing CNR for a Simulated Shape Parameter $\nu = 0.1$, (a) Estimated Shape Parameter $\hat{\nu}$, (b) Estimated Thermal Noise Parameter $\hat{p}_n$.

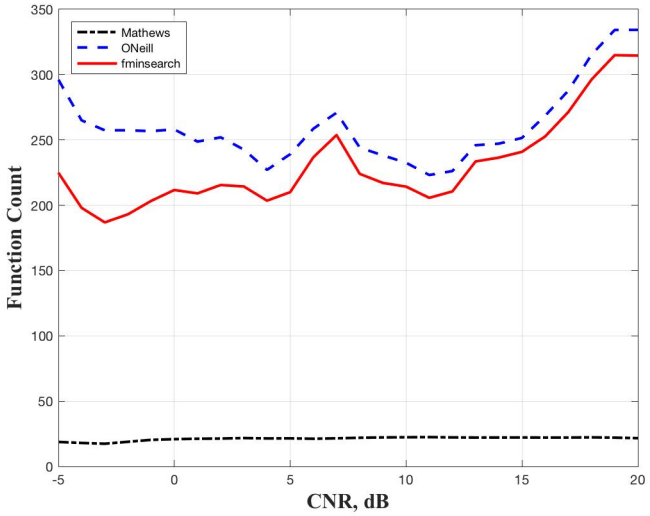

(a)

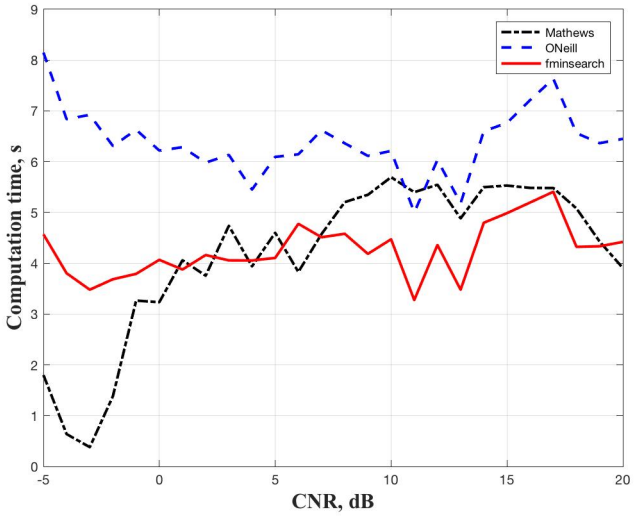

(b)

Fig. 3.7: Comparison of the Three 3-D Search Methods Using Simulated Data with Increasing CNR for a Simulated Shape Parameter $\nu = 0.1$, (a) Algorithm Function Count, (b) Time Performance in Seconds.

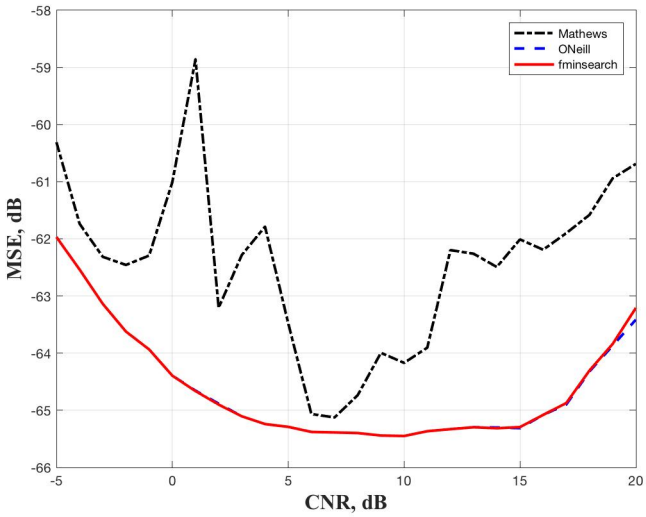

Fig. 3.8: Comparison of the CCDF MSE (dB) for the Three 3-D Search Algorithms with Increasing CNR, Using Simulated Clutter with Shape Parameter $\nu = 0.1$.

3.9.0.1 3-D Search Methods

Unlike the 1-D search methods that use the first two intensity sample moments, the 3-D Nelder-Mead solves for all three parameters using a downhill simplex method [43, 47, 48]. Fig. 3.6(a) compares the estimated shape parameter $\hat{\nu}$ for the three, 3-D search methods and note they all achieve comparable results where both the $\mathrm{fminsearch}$ and O'Neill methods provide the best performance for CNR in the range of -5 to 0 dB with the Mathews method being unstable in the -5 to 0 dB range. All methods diverge from the actual parameter value of $\nu = 0.1$ beginning at a CNR of 12 dB. Fig. 3.6(b) compares the estimated noise parameter $\hat{\rho}_n$ and we compare the algorithm results with the value used to generate the simulated clutter and note that all three methods achieved almost identical results with the exception of where the Mathews method diverges in the region of -5 to -4 dB.

Fig. 3.7(a) compares the total number of function evaluations and its easy to see, the O'Neill method requires more evaluations in the CNR region of -5 to 7 dB, and this could be related to not including ΔX as a termination criteria. We also note that the Mathews method completes with less function evaluations or calls to (3.20). Fig. 3.7(b) shows the computation time performance and the results are not as expected considering the Mathews method is comparable with $\mathrm{fminsearch}$ but has a considerable difference in calls to (3.20) as depicted in Fig. 3.7(a).

Fig. 3.8 shows the CCDF MSE performance for the compared algorithms with both $\mathrm{fminsearch}$ and O'Neill methods having and overall lower CCDF MSE throughout the tested CNR region.

Chapter 4

PARAMETER ESTIMATION USING 1-D NONLINEAR CURVE FITTING AND INTENSITY MOMENTS

4.1 Introduction

We propose a new intensity compound K-distribution (ICKD) model parameter estimation method for sea clutter intensity data with thermal noise. The new method combines the intensity moments (IM) estimation method with a one-dimensional (1-D) nonlinear curve fitting method to iteratively estimate all three model parameters that define the ICKD probability distribution function (PDF). The one parameter search routine to estimate the thermal noise parameter does not suffer from the computational inefficiency of a three-dimensional (3-D) search as in [6]. As the method fits the thermal noise power estimate to the tail of the data ICKD PDF, no *prior* knowledge of the spectral distribution of sea clutter is required. This avoids the use of windowing when estimating the noise power parameter using time-frequency methods as the performance accuracy is then highly dependent on the choice of the duration of the window [7].

4.2 Description of Proposed Method

As demonstrated in Section 3.3, the intensity moment approach for estimating all three ICKD parameters is simple to implement but requires large amounts of data for accuracy. Modified versions of the intensity moment approaches improve the accuracy but assume an effective shape parameter under no noise conditions. On the other hand, the 3-D nonlinear curve fitting (NCF) approach can yield accurate results but it is very computationally

intensive. In order to avoid the computational complexity of the 3-D search while maintaining the low estimation MSE performance, we develop an iterative 1-D search approach integrated with the IM method.

The new integrated noise-power estimation intensity moments (NEIM) method is based on iteratively using 1-D nonlinear curve fitting to estimate the thermal noise power p_n, followed by the IM method to estimate the shape ν and scale b ICKD parameters. The fitting can be performed using any nonlinear least-squares approach, including the Nelder-Mead unconstrained nonlinear optimization method.

The NEIM approach uses N_s sea clutter intensity observations z_k, $k = 1, \ldots, N_s$, that are normalized by their mean. At the ith iteration, the CCDF points $\Phi_Z\left(z_m; \hat{\boldsymbol{\theta}}^{(i)}\right)$, $m = 1, \ldots, M$, are used to select the tail M (out of L) CCDF points. The M CCDF points are used to compute a goodness of fit measure or curve fitting MSE as a function of the thermal noise power given by

$$\mathscr{E}_Z(p_n^{(i)}) = \frac{1}{M} \sum_{m=1}^{L-M} \left(\Phi_Z^{\text{sim}}\left(z_m\right) - \Phi_Z\left(z_m; p_n^{(i)}\right) \right)^2 , \tag{4.1}$$

where $\Phi_Z(z; p_n) = \int_z^\infty p_Z(\zeta; p_n)\, d\zeta$. The noise power $\hat{p}_n^{(i)}$ is obtained by minimizing the curve fitting MSE in (4.1) using

$$\hat{p}_n^{(i)} = \arg \min_{p_n^{(i)} \in R_p} \mathscr{E}_Z(p_n^{(i)}) . \tag{4.2}$$

where the minimization is performed over the range R_p of expected thermal noise power values.

The NEIM approach uses the estimated thermal noise power estimate $\hat{p}_n^{(i)}$ at the ith iteration to estimate the shape parameter $\hat{\nu}^{(i)}$ in (3.5) and the scale parameter $\hat{b}^{(i)}$ in (3.6) using the first and second sample moments. Note that the sample moments can be computed

using

$$\hat{\mu}_1 = E[Z] = \frac{1}{N_s}\sum_{k=1}^{N_s} z_k \tag{4.3}$$

$$\hat{\mu}_2 = E[Z^2] = \frac{1}{N_s}\sum_{k=1}^{N_s} z_k^2 \,. \tag{4.4}$$

The resulting shape and scale parameter estimates are obtained, following (3.5) and (3.6), as

$$\hat{\nu}^{(i)} = \frac{2(\hat{\mu}_1 - \hat{p}_n^{(i)})^2}{\hat{\mu}_2 - 2\,\hat{\mu}_1^2} \tag{4.5}$$

$$\hat{b}^{(i)} = \frac{\hat{\nu}^{(i)}}{\hat{\mu}_1 - \hat{p}_n^{(i)}} \,. \tag{4.6}$$

The estimated parameter vector $\hat{\boldsymbol{\theta}}^{(i)} = [\hat{\nu}^{(i)}\ \hat{b}^{(i)}\ \hat{p}_n^{(i)}]$ is then used to simulate the CCDF points $\Phi_Z\big(z_m; \hat{\boldsymbol{\theta}}^{(i)}\big)$, $m = 1, \ldots, M$ for use in the next iteration.

The parameters of the fitted model are updated at each iteration until convergence to a global minimum. Convergence depends on some pre-determined stopping criteria such as a maximum number of iterations $I_{\max}$ or a minimum desirable value of the curve fitting MSE. Assuming convergence is reached at iteration $I_{\max}$, the estimated thermal noise power is

$$\hat{p}_n = \hat{p}_n^{(I_{\max})} \tag{4.7}$$

with curve fitting MSE $\mathscr{E}_Z(p_n^{(I_{\max})})$. The final estimates of the shape $\hat{\nu}$ and scale $\hat{b}$ are obtained using (4.5) and (4.6) with $i = I_{\max}$ and $\hat{\boldsymbol{\theta}} = [\hat{\nu}\ \hat{b}\ \hat{p}_n]$. The estimated CNR is

$$\hat{\eta} = (\hat{\mu}_1 - \hat{p}_n)/\hat{p}_n = \frac{\hat{\nu}/\hat{b}}{\hat{p}_n} \,. \tag{4.8}$$

Fig. 4.1 provides a block diagram of the NEIM algorithm steps. The input to the algorithm includes mean-normalized clutter intensity observations and the estimates of the first two sample moments in Equations (4.3) and (4.4). In addition, it requires a range of values

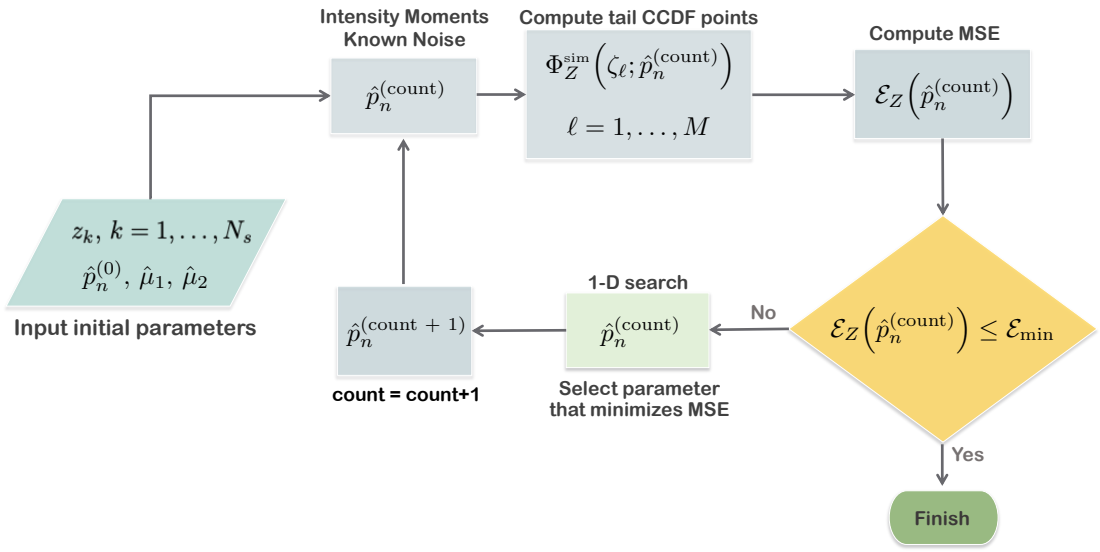

Fig. 4.1: Noise-power Estimation Intensity Moments (NEIM), Flowchart Using a One Dimensional Search Algorithm.

for the thermal noise power parameter $p_n \in R_p$. The steps of the iterative NEIM approach are also summarized in Algorithm 2. The algorithm uses a stopping criteria that is based on the convergence of the $\hat{p}_n$ estimates. The convergence requires that the difference between two consecutive iterations satisfies $|\hat{p}_n^{(i+1)} - \hat{p}_n^{(i)}| < \varepsilon_X$, where ε_X is the minimum step size provided in Table 3.2. The optimization algorithm used in this method finds the minimum of a single-variable function over a fixed interval using the golden search method and parabolic interpolation [49]. In MATLAB, the function that implements this minimization is fminbnd.

Algorithm 2: Iteration steps for NEIM

- Input: Initial range of $p_n \in Rp$, mean-normalized intensity observations, z_k, $k = 1, \ldots, N_s$, minimum step size ε_X, $P_{\text{FA}} \geq 0.003$
- Using z_k, simulate $\Phi_Z^{\text{sim}}(z_\ell)$, $\ell = 1, \ldots, L$, using the intensity data provided; this is simulated as $\Phi_Z^{\text{sim}}(z_\ell) = \Pr(Z > z_\ell)$
- Obtain M (out of L), the number of tail CCDF points, as the number of intensity samples z_m such that $P_{\text{FA}} \geq 0.003$, where $P_{\text{FA}} = \Pr(Z > z_m) = \Phi_Z^{\text{sim}}(z_m)$
- At the ith iteration, $i = 0, \ldots, I_{\max}$, compute the tail M modeled CCDF points $\Phi_Z(z_m); \boldsymbol{\theta}^{(i)}$, $m = 1, \ldots, M$ using $\Phi_Z(z; \boldsymbol{\theta}) = \int_z^\infty p_Z(\zeta; \boldsymbol{\theta})\, d\zeta$, where $p_Z(\zeta; \boldsymbol{\theta})$ is the ICKD model PDF with parameter vector $\boldsymbol{\theta}$. Also, $\boldsymbol{\theta}^{(i)}$ are all allowable vector values of $\boldsymbol{\theta}$ over which the search is performed. This is accomplished by first obtaining the optimal $\hat{p}_n^{(i)}$ (4.2), then creating $\hat{\boldsymbol{\theta}}^{(i)}$ with (4.5) and (4.6)
- Compute the curve fitting MSE as $\mathscr{E}_Z(\boldsymbol{\theta}^{(i)}) = \frac{1}{M} \sum_{m=1}^{L-M} \left(\Phi_Z^{\text{sim}}(z_m) - \Phi_Z(z_m; \boldsymbol{\theta}^{(i)}) \right)^2$
- Find $\hat{p}_n^{(i)}$ that minimizes the curve fitting MSE, $\mathscr{E}_Z(p_n^{(i)}) = \frac{1}{M} \sum_{m=1}^{L-M} \left(\Phi_Z^{\text{sim}}\left(z_m\right) - \Phi_Z\left(z_m; p_n^{(i)}\right) \right)^2$
- Stopping criteria: for a given ε_X, stop iteration when $|\hat{p}_n^{(i+1)} - \hat{p}_n^{(i)}| < \varepsilon_X$

4.3 Performance of NEIM Method

The estimation performance of the new NEIM method is demonstrated using both simulated and real sea clutter intensity observations. For this processing, we followed the simulation environment and algorithm parameters described in Section 3.7.

4.3.1 1-D Search Algorithm Comparisons

We considered three methods to perform the 1-D search for the thermal noise power, as discussed next. These methods seek to find a minimum value on a defined interval; we selected the interval corresponding to the minimum intensity and the power value 0.8.

Method 1: This method, called Matthew's method, uses the golden search and is discussed in [45]. Its input includes the search interval, a minimum step size ε_X, and a minimum function difference ε_F as input. We modified this algorithm to use ε_X as a stopping criterion and to return the number of function evaluations.

Method 2: This method uses the golden search and parabolic interpolation; in MATLAB, it is implemented by the function $\mathrm{fminbnd}$. The stopping criteria include the search interval, ε_X, and a maximum number of function evaluations.

Method 3: This is a root-finding method, called Brent's method, that combines root-bracketing, bisection and interpolation to locate the minimum value [50]. We implemented this method following Reference [51]. The method requires the search interval, ε_X, ε_F, an initial estimate of the minimum value, and an estimate on the upper bound of the second derivative as inputs. We also modified it to return the number of function evaluations.

Fig. 4.2(a) compares the estimated shape parameter $\hat{\nu}$ for varying CNR obtained using the three 1-D search methods; as it can be observed, all three methods achieved nearly identical results. All three methods also perform similarly when we compare the estimated

noise power parameter $\hat{\rho}_n$ for varying CNR in Fig. 4.2(b). Note that all methods result in estimates that differ from the actual value around 12 dB CNR. Fig. 4.3(a) compares the total number of function evaluations. As it can be observed, Method 1 is stable for all CNR and converges using a smaller number of function evaluations, when compared to Method 2 and Method 3. Fig. 4.3(b) shows the computation time (CT) performance for each of the methods; the CT is relative high as a high number of functions need to be evaluated. Fig. 4.4 shows that the three methods have similar CCDF MSE performance; Method 3 has less than 1 dB difference from 10 to 20 dB CNR.

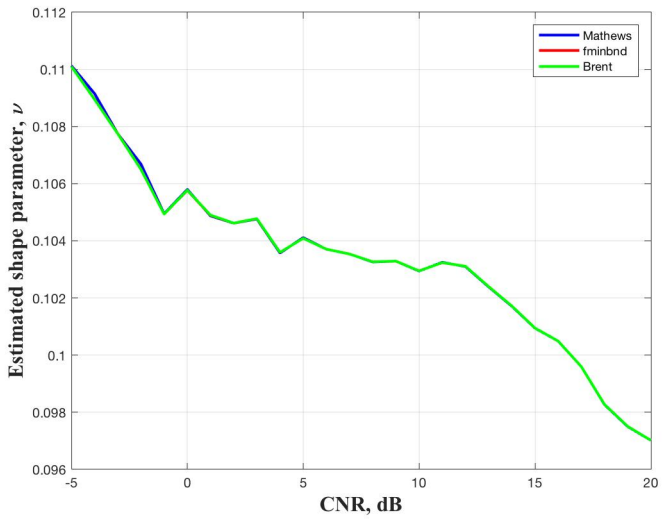

(a)

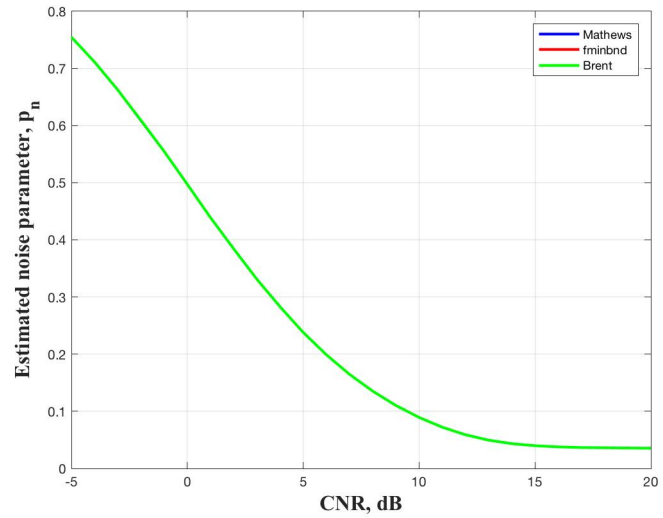

(b)

Fig. 4.2: Comparison of the Three 1-D Search Methods Using Simulated Data For Increasing CNR for a Simulated Shape Parameter $\nu = 0.1$: (a) Estimated Shape Parameter $\hat{\nu}$; (b) Estimated Thermal Noise Parameter $\hat{p}_n$.

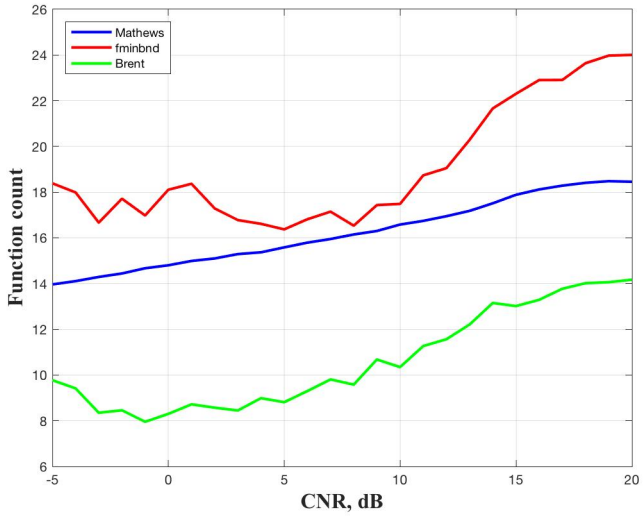

(a)

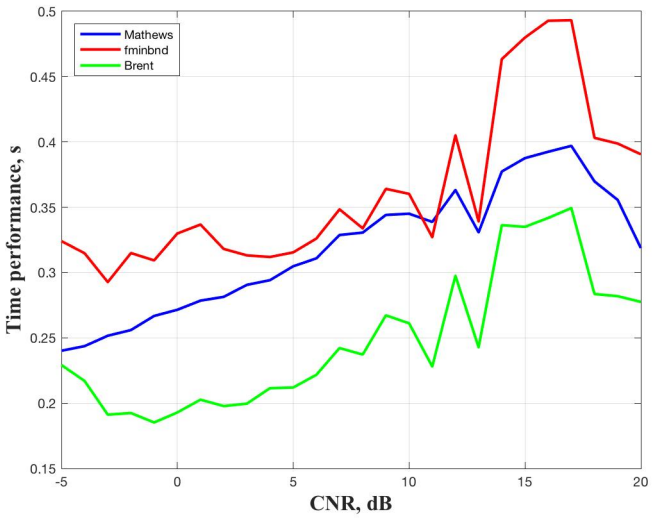

(b)

Fig. 4.3: Comparison of the Three 1-D Search Methods Using Simulated Data For Increasing CNR for a Simulated Shape Parameter $\nu = 0.1$: (a) Algorithm Function Count; (b) Time Performance in Seconds.

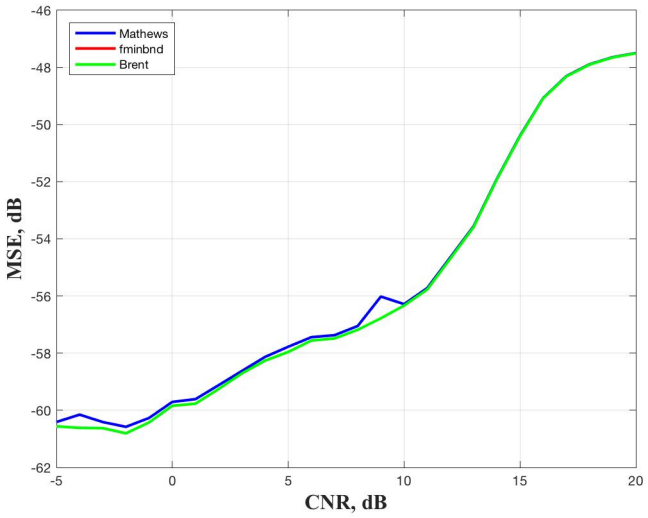

Fig. 4.4: Comparison of the CCDF MSE (dB) for the Three 1-D Search Algorithms, For Increasing CNR, using Simulated Clutter with Shape Parameter $\nu = 0.1$.

4.4 Performance Comparisons using Simulated Sea Clutter Intensity

4.4.1 Comparisons For Shape Parameter $\nu = 0.1$

Based on the performance results in Sections 4.3.1 and 3.8, we compare Method 2 (using MATLAB function fminbnd) for the 1-D NEIM approach and the Nelder-Mead search (using MATLAB function fminsearch) for the 3-D NCF approach.

Fig. 4.5 depicts the thermal noise power $\hat{p}_n$ NEIM and NCF estimation results for increasing CNR and a fixed simulated shape parameter $\nu = 0.1$. The estimated values are compared with the actual value of the power parameter used in the simulation. As it can be observed, both methods perform well; the NEIM shows a slight error at 11 dB CNR.

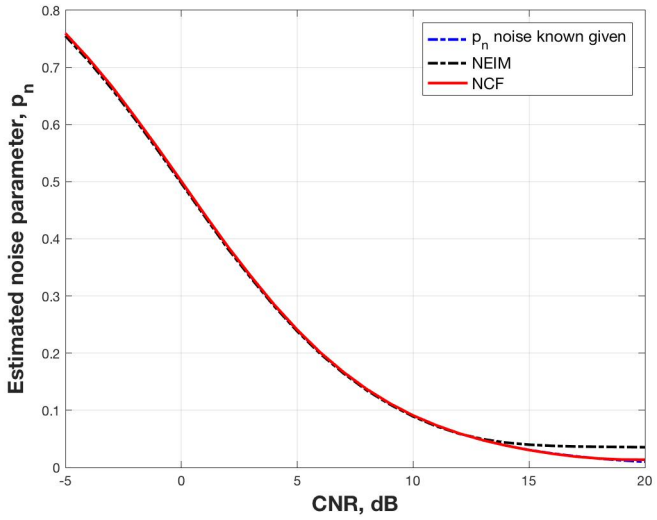

Fig. 4.5: Comparison of the Estimated Thermal Noise Power $\hat{p}_n$ Obtained Using the NEIM and NCF Methods with the Actual p_n Value, for Increasing CNR; the Simulated Clutter was $N_s = 100,000$ Samples and Had a fixed Shape Parameter $\nu = 0.1$.

Fig. 4.6(a) depicts the shape parameter $\hat{\nu}$ estimation results when the actual simulated

value was $\nu = 0.1$. The three methods compared, IM, NCF and NEIM, perform relatively well; the NCF performance diverges after 10 dB CNR. Fig. 4.6(b) depicts the CCDF MSE in dB; the NCF method is shown to have the best overall performance, whereas the IM and NEIM methods diverge after 5 dB CNR.

Fig. 4.7(a) compares the CT performance, in seconds, of the NCF and NEIM algorithms. It can be observed that the NEIM CT remains almost constant at less than 1 s. The NCF CT varies between about 2.8 s and 4.3 s. Fig. 4.7(b) is a direct comparison of the CCDF MSE for the NEIM and NCF methods; although the NCF performs better than the NEIM from 5 to 20 dB CNR, it is computationally intensive as demonstrated in Fig. 4.7(a).

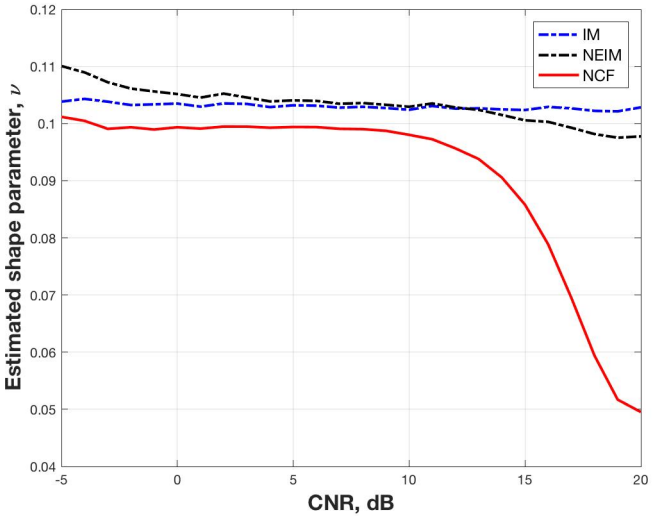

(a)

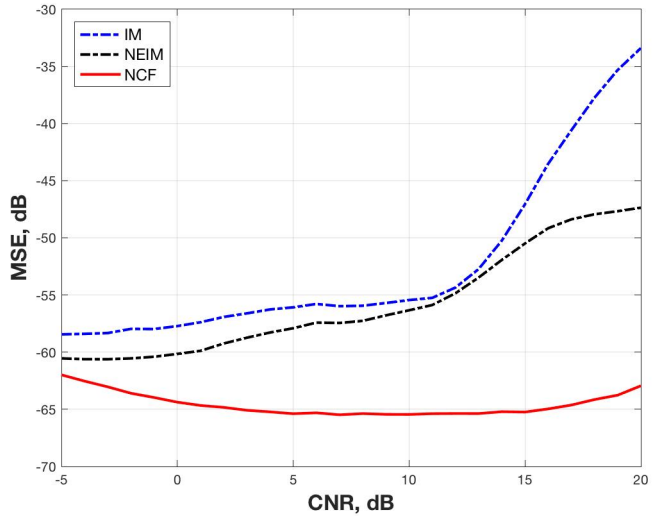

(b)

Fig. 4.6: Comparison of the IM, NCF, and NEIM Methods for Increasing CNR using Simulated Clutter with Shape Parameter $\nu = 0.1$: (a) Estimated Shape Parameter $\hat{\nu}$; (b) CCDF MSE (dB).

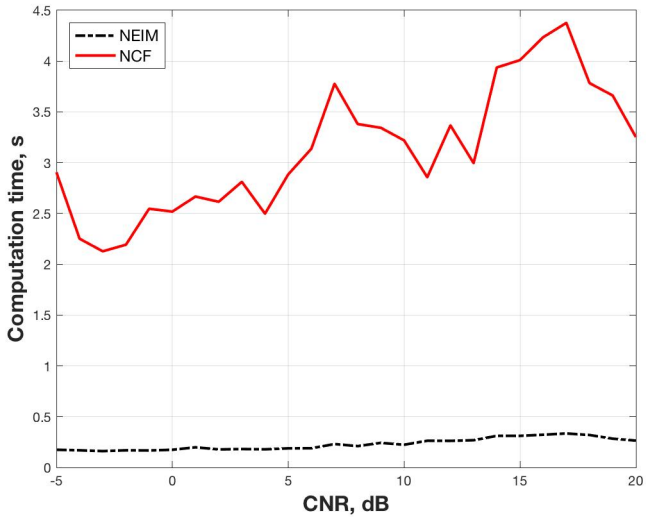

(a)

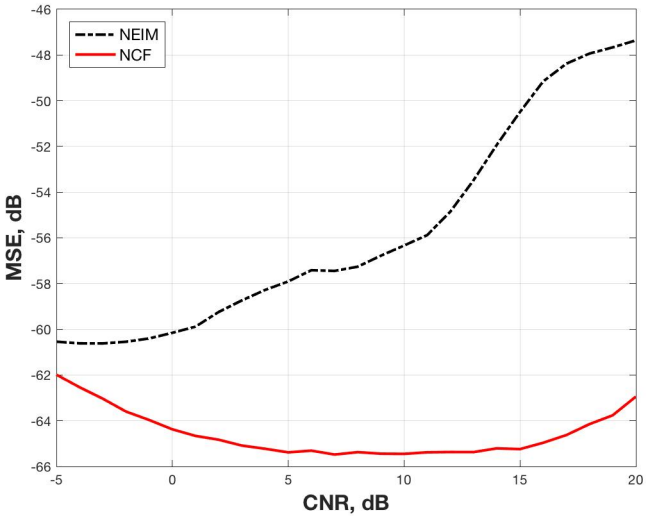

(b)

Fig. 4.7: Comparison of IM, NEIM and NCF Methods Using Simulated Clutter with Increasing CNR, and Shape Parameter $\nu = 0.1$. (a) Time Performance in Seconds, (b) CCDF MSE (dB).

4.4.2 *Comparisons For Shape Parameter* $\nu = 0.5$

Fig. 4.8 depicts the thermal noise $\hat{p}_n$ estimation results for increasing CNR levels with a simulated shape parameter of $\nu = 0.5$ using the NEIM and NCF methods. In this figure, we compare these estimated values with the simulated p_n noise value. We see good agreement with the estimated $\hat{p}_n$ with slight deviation in the NCF method beginning at a CNR of -1 dB.

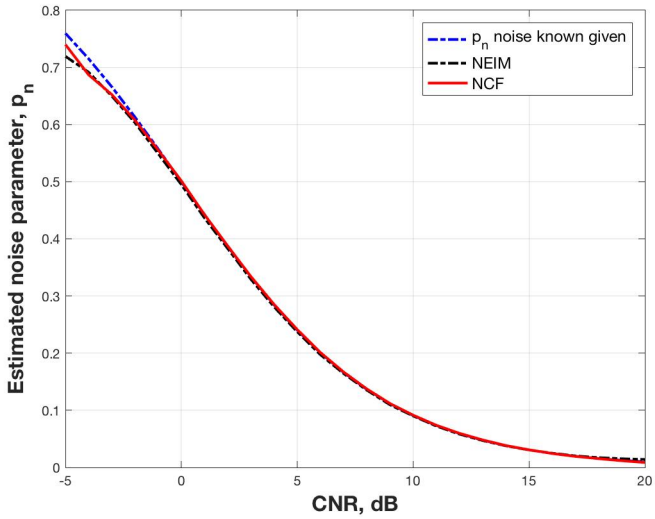

Fig. 4.8: Comparison of the Estimated Thermal Noise $\hat{p}_n$ for the NEIM and NCF Methods with the Known Value p_n, Using Simulated Clutter with Increasing CNR, and Shape Parameter $\nu = 0.5$.

Fig. 4.9(a) depicts the shape parameter $\hat{\nu}$ estimation results for a value $\nu = 0.5$; we notice the thee estimation methods work well from 0 to 13 dB CNR. We also see a slight deviation in the estimated shape parameter for the NEIM method between CNR region of -5 dB and 0 dB and very minor separation for the NEIM above 17 dB. The figure also depicts the NCF method is unstable in the CNR region of -5 dB to 2 dB with the estimated shape

parameter diverging from the simulated value beginning at a CNR of 13 dB. Fig. 4.9(b) depicts the CCDF MSE in dB for the IM, NEIM and NCF methods; we notice good agreement between the IM and NEIM methods. The NCF method has an overall lower CCDF MSE; however, it becomes unstable from -5 to -2 dB CNR and starting at 18 dB CNR.

Fig. 4.10(a) compares the CT performance in seconds between the NEIM and NCF methods; we notice that the NEIM method is almost constant at less than 1 whereas the NCF decreases from 7.2 s at -5 dB CNR, reaches a low of 1.5 s at 4 dB CNR and increases back to approximately 2.3 s at 19 dB CNR. Fig. 4.10(b) is a direct comparison of the CCDF MSE of the NEIM and NCF methods; it can be observed that the NCF method has an overall lower CCDF MSE.

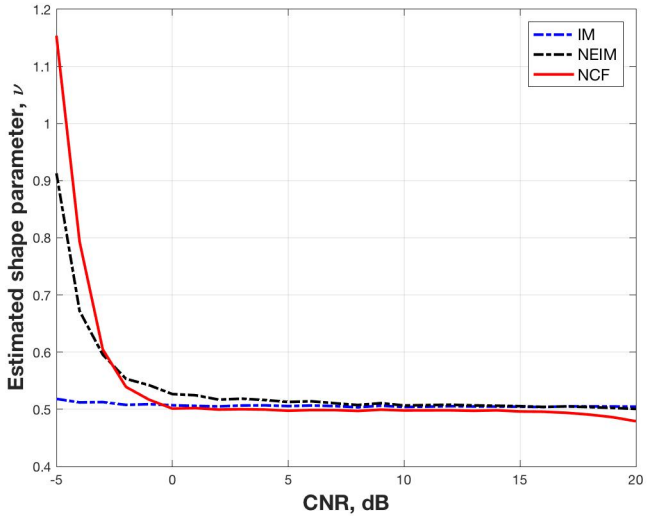

(a)

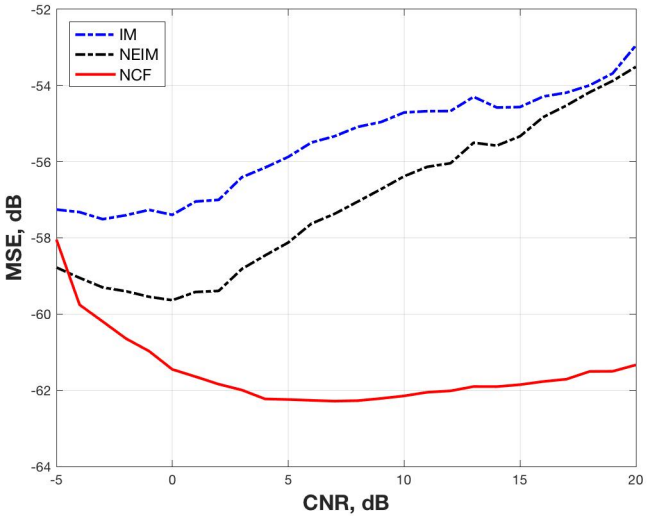

(b)

Fig. 4.9: Comparison of IM, NEIM and NCF Methods Using Simulated Clutter with Increasing CNR, and Shape Parameter $\nu = 0.5$: (a) Estimated Shape Parameter $\hat{\nu}$; (b) CCDF MSE (dB).

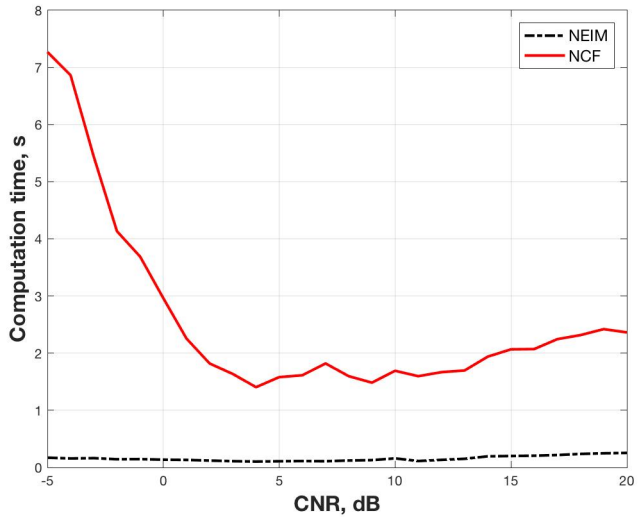

(a)

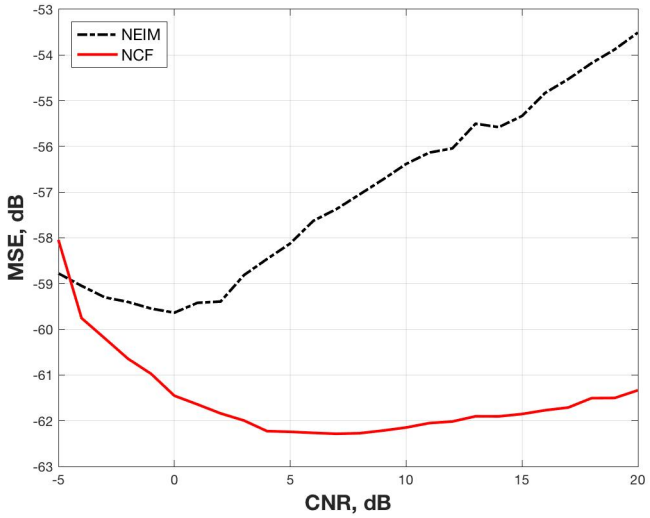

(b)

Fig. 4.10: Comparison of IM, NEIM and NCF Methods Using Simulated Clutter with Increasing CNR, and Shape Parameter $\nu = 0.5$: (a) Time Performance in Seconds, (b) CCDF MSE (dB).

4.4.3 *Comparisons For Shape Parameter $\nu = 1$*

Fig. 4.11 depicts the shape parameter $\hat{\nu}$ estimation results for increasing CNR levels with a simulated shape parameter of $\nu = 1.0$ using the NEIM and NCF methods. We compare these estimated values with the simulated p_n noise value and see good agreement with the estimated $\hat{p}_n$ with deviation for both the NEIM and NCF methods for -5 to -3 dB CNR.

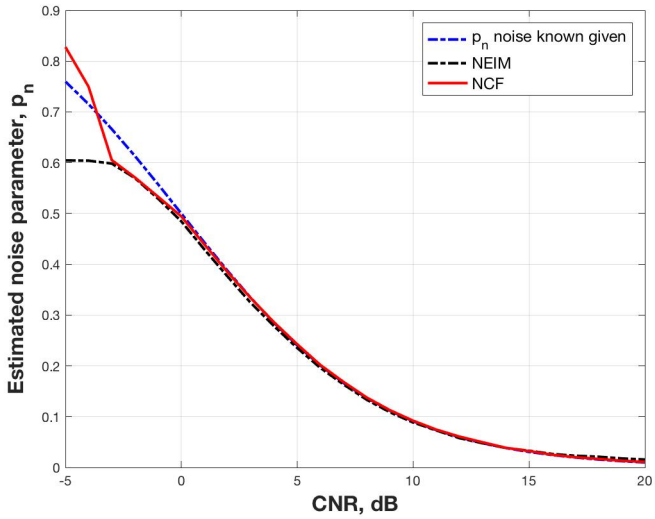

Fig. 4.11: Comparison of the Estimated Thermal Noise $\hat{p}_n$ for the NEIM and NCF Methods with the Actual p_n Value, Using Simulated Clutter with Increasing CNR and Shape Parameter $\nu = 1$.

Fig. 4.12(a) depicts the shape parameter $\hat{\nu}$ estimation results for $\nu = 1$; we notice that the three estimation methods work well, except from -5 to -2 dB CNR, where the performance of both methods deteriorates; the NEIM shows a larger divergence. Fig. 4.12(b) depicts the CCDF MSE in dB; it can be observed that the NCF method provides an overall lower CCDF MSE when compared to the IM and NEIM methods.

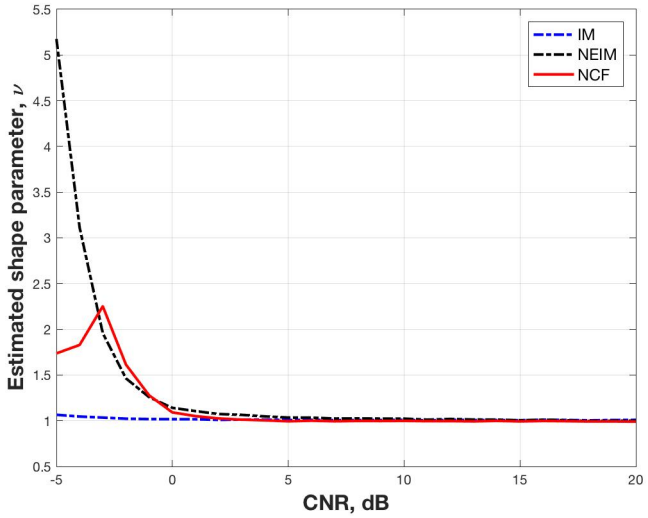

(a)

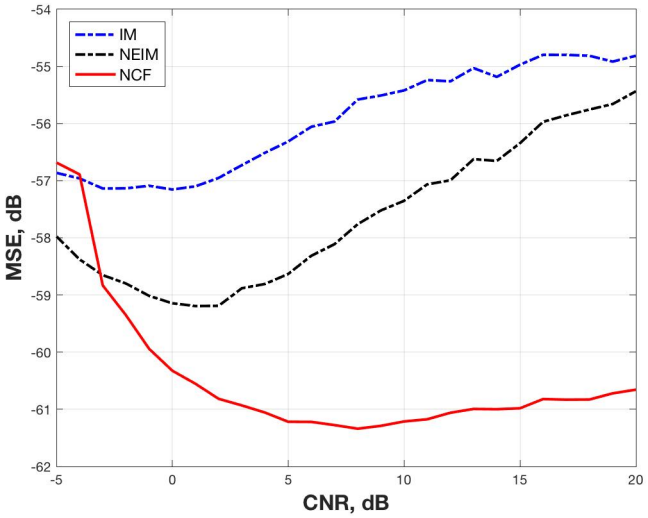

(b)

Fig. 4.12: Comparison of IM, NEIM and NCF Methods Using Simulated Clutter with Increasing CNR and Shape Parameter $\nu = 1$: (a) Estimated Shape Parameter $\hat{\nu}$; (b) CCDF MSE (dB).

Fig. 4.13(a) compares the CT performance in seconds between the NEIM and NCF methods; we notice that the CT for the NEIM method is almost constant at less than 1 s whereas the NCF CT decreases from 7.5 s at -3 dB, reaches a low of 1 s at 12 dB, then climbs back to 2 s to 20 dB. Fig. 4.13(b) is a direct comparison of the CCDF MSE of the NEIM and NCF methods; the NCF has an overall lower CCDF MSE but becomes unstable at 0 dB CNR.

4.4.4 Estimation Comparison for Varying Parameters

To further investigate the ICKD parameter estimation accuracy of the IM, NCF and NEIM methods, we varied different simulation variables, including the number N_s of simulated observation samples. Note that the estimation results were averaged over 1,000 Monte Carlo (MC) simulations. Table 4.1 compares the three methods when $N_s = 10,000$ samples, for varying shape and CNR values. Table 4.2 compares the methods using $N_s = 100,000$ samples The estimation results in Table 4.1 match the curve fitting results in Fig. 4.14. We note that, as CNR increases or $\hat{p}_n$ decreases, $\hat{b}$ approaches $\hat{v}$; this is expected, as shown in Equation (3.2).

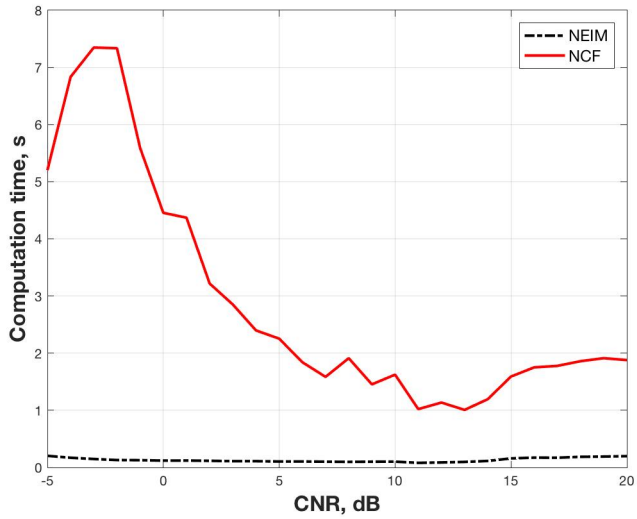

(a)

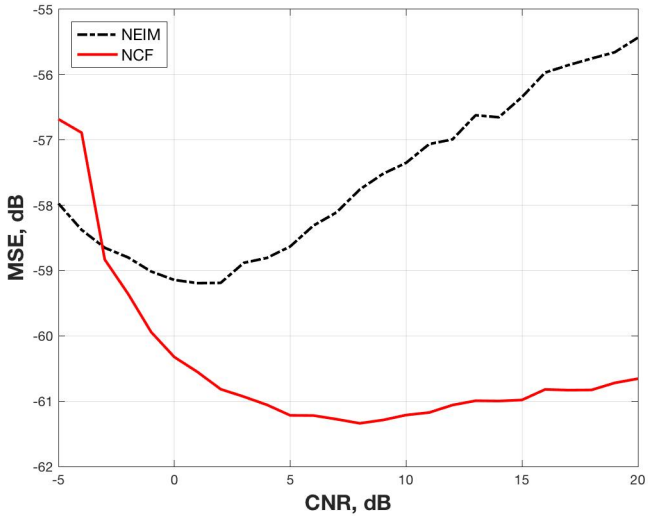

(b)

Fig. 4.13: Comparison of IM, NEIM and NCF Methods Using Simulated Clutter with Increasing CNR, and Shape Parameter $\nu = 1$: (a) Time Performance in Seconds; (b) CCDF MSE (dB).

Shape ν	Simulated clutter intensity parameters: Scale b	Noise p_n	CNR (dB)	Estimation method	$\hat{\nu}$	$\hat{b}$	$\hat{p}_n$	CCDF MSE (dB)
0.1	0.5	0.5	0	IM	0.1031	0.2078	NA	-59.38
				NCF	0.0990	0.1968	0.5008	-65.95
				NEIM	0.1048	0.2076	0.4972	-61.72
	0.09	0.09	10	IM	0.1034	0.1137	NA	-56.91
				NCF	0.0981	0.1088	0.0912	-66.80
				NEIM	0.1040	0.1140	0.0891	-57.74
0.5	0.5	0.5	0	IM	0.5066	1.0133	NA	-58.58
				NCF	0.5115	0.9993	0.4966	-60.61
				NEIM	0.5308	1.0333	0.4928	-60.78
	0.09	0.09	10	IM	0.5043	0.5548	NA	-56.18
				NCF	0.4968	0.5461	0.0918	-63.41
				NEIM	0.5073	0.5563	0.0899	-57.84
1.0	0.5	0.5	0	IM	1.0177	2.0355	NA	-58.23
				NCF	1.1158	2.0535	0.4895	-61.33
				NEIM	1.1693	2.145	0.4784	-60.25
	0.09	0.09	10	IM	1.0105	1.1116	NA	-56.68
				NCF	1.0009	1.0976	0.0909	-61.18
				NEIM	1.0256	1.119	0.0872	-58.49

Table 4.1: Estimated Intensity Clutter Parameters Using N_s=10,000 Simulated Samples.

In Table 4.2, two shape values and two CNR values are considered with the increased number of samples. The estimation accuracy of the three methods is similar. However, for $\nu = 0.1$ and 20 dB CNR, the accuracy of the NCF estimated shape parameter $\hat{\nu}$ decreases; this is also depicted in Fig. 4.6(a).

Shape ν	Simulated clutter intensity parameters: Scale b	Noise p_n	CNR (dB)	Estimation method	$\hat{\nu}$	$\hat{b}$	$\hat{p}_n$	CCDF MSE (dB)
0.1	0.2403	0.7597	-5	IM	0.1000	0.4163	NA	-68.00
				NCF	0.1002	0.4161	0.7596	-71.82
				NEIM	0.1003	0.4167	0.7597	-70.17
	0.9901	0.0099	20	IM	0.1001	0.1011	NA	-29.56
				NCF	0.0380	0.0877	0.0186	-65.55
				NEIM	0.0914	0.0966	0.0543	-47.13
0.5	0.2403	0.7597	-5	IM	0.5019	2.0891	NA	-67.22
				NM	0.4865	1.9428	0.7708	-64.61
				NEIM	0.5198	2.1124	0.7573	-68.75
	0.9901	0.0099	20	IM	0.5007	0.5057	NA	-51.65
				NCF	0.4663	0.4863	0.0089	-67.02
				NEIM	0.4913	0.5009	0.0194	-56.11

Table 4.2: Estimated Intensity Clutter Parameters Using N_s=100,000 Simulated Samples.

4.4.5 CCDF Fit Performance

Fig. 4.14 shows the parameter estimation performance fitting the estimated CCDF to the actual data. Equation (2.10) is used to create the estimated CCDF. The IM, NCF and NEIM methods are compared, using N_s=10,000 samples.

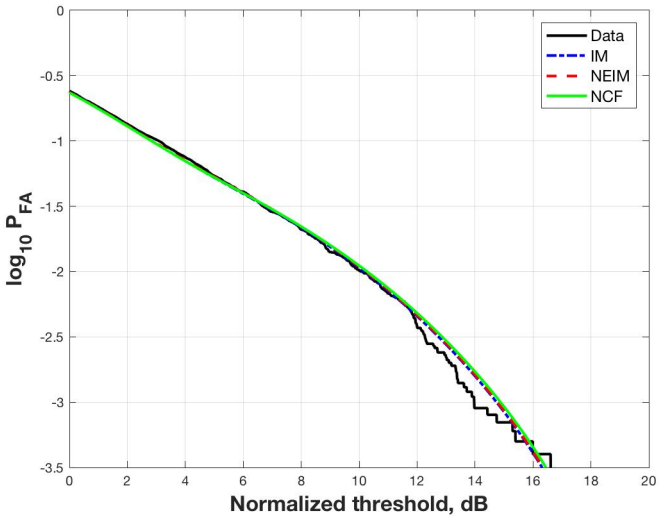

(a)

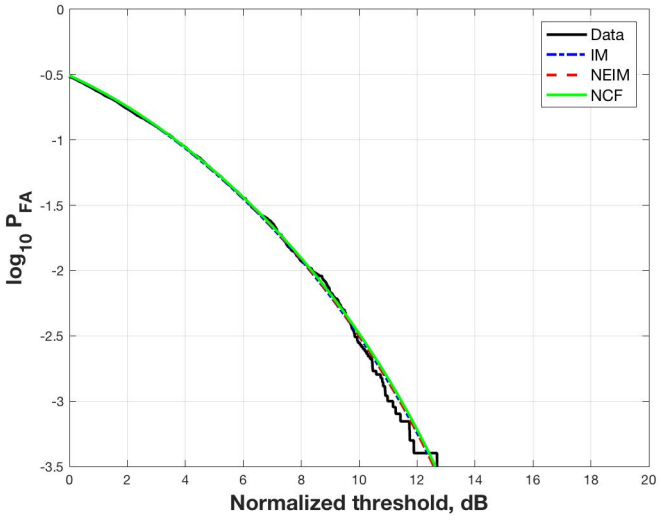

(b)

Fig. 4.14: CCDF Using Estimated Parameters for Simulated Data with CNR = 0 dB ; (a) Shape Parameter $\nu = 0.1$; (b) Shape Parameter $\nu = 0.5$.

4.4.6 *Simulation of Correlated Coherent Sea Clutter*

In estimating the ICKD parameters, we showed the dynamics of the sea surface that have an impact on both the moment based and nonlinear curve fitting estimators. In [7], the authors provide a method to simulate correlated coherent (CC) sea clutter which also captures the time-varying spectral characteristics of specific range bins in the provided CSIR datasets. This is an important model because it adequately captures the time changing nature of the Doppler spectra, thereby simulating the non-Gaussian statistics that occur near the spectral edges. The model also generates data in the time domain, thereby preserving the continuity of both amplitude and phase. Additional work is required in this area to understand the limitations (if any) to this important model.

Fig 4.15 compares the simulated Doppler spectra with the modeled spectra obtained from CSIR CFC17_001 (RB 1) we see very good agreement in the time changing Doppler spectra. Fig. 4.16 compares the amplitude and phase data between the real CSIR CFC17_001 (RB 1) dataset and the simulated data using the method in [7]. It is important to note, that this model also captures a good continuity in amplitude and phase, meaning there are no drop-outs or abrupt changes.

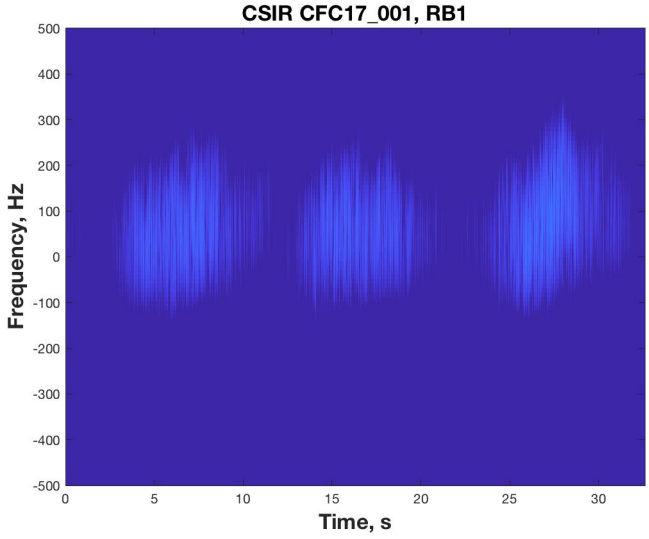

(a)

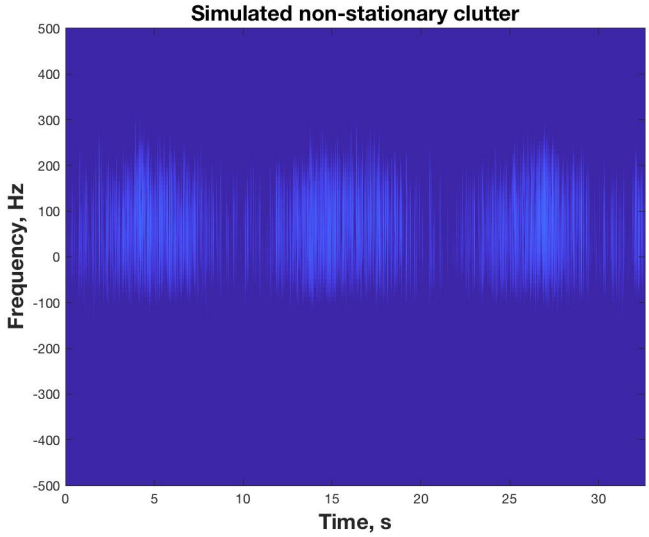

(b)

Fig. 4.15: Doppler Spectra Using a FFT Size of 512 Samples, a Taylor Window with $N_T = 64, \bar{n} = 4$ and SLL $= -55$; (a) CFC17_001 (RB 1); (b) Simulated CFC17_001 (RB 1).

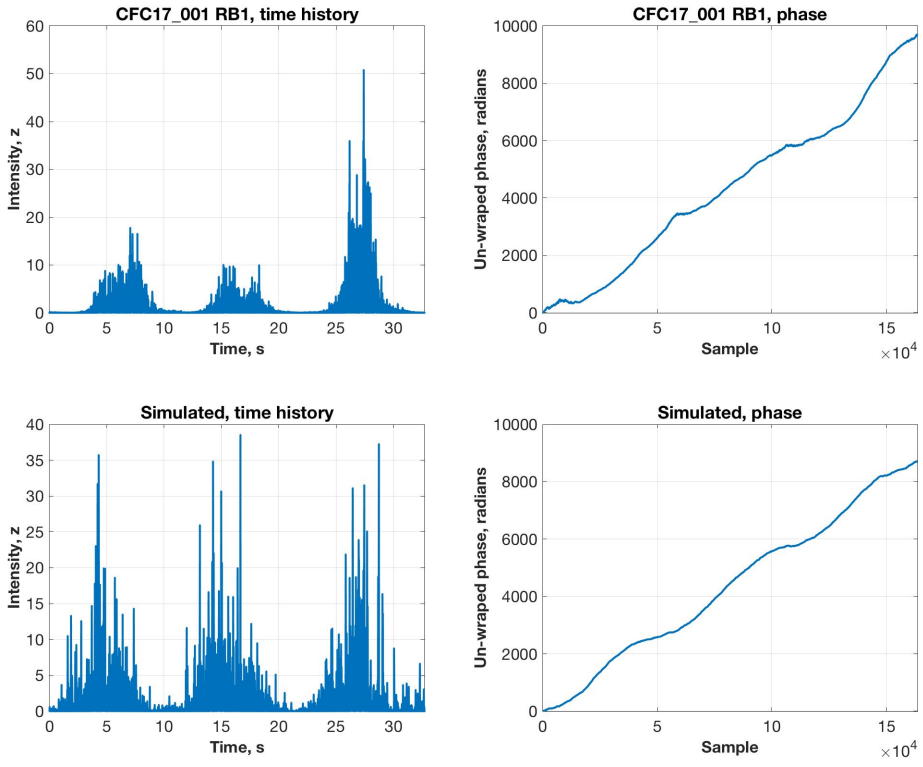

Fig. 4.16: Comparison of the Amplitude and Phase Between the Simulated and Real CSIR CFC17_001 RB1 Sea Clutter.

Fig. 4.17 depicts the P_{FA}, results for the IM, NCF and NEIM methods using the simulated CC time history data in Fig. 4.16. The goal for this simulation was to match the intensity statistics along with the temporal characteristics of the CSIR CFC17_001 (RB 1) dataset [7], therefore we simulated a shape parameter $\nu = 0.4$ and $p_n = 0.01$. Table 4.3 provides the estimated parameters and we notice the estimation methods can successfully estimate the parameters using the CC data.

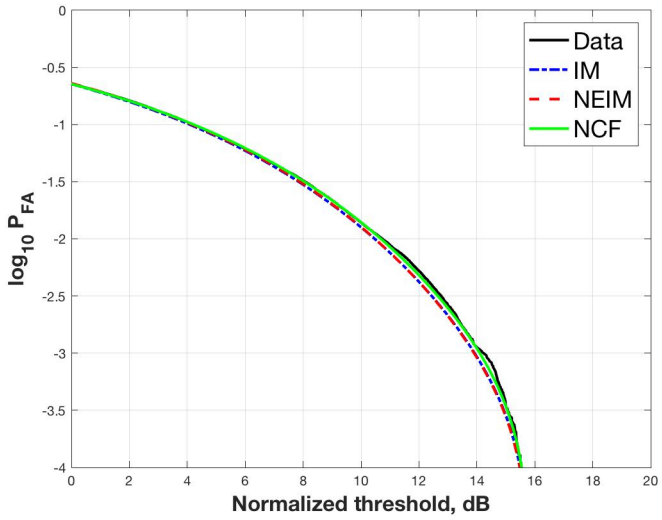

Fig. 4.17: CCDF Using Estimated Parameters for Correlated Coherent Simulated Data with CNR = 20 dB, Shape Parameter $\nu = 0.4$.

Estimation Method	Estimated $\hat{\nu}$	Estimated $\hat{p}_n$	CNR (dB)	MSE (dB)
IM	0.3738	0.0603	11.93	-57.18
NCF	0.3679	0.0176	17.48	-69.65
NEIM	0.4002	0.0274	15.50	-58.85

Table 4.3: Estimated Parameters Using Simulated Correlated Coherent Sea Clutter.

4.5 K-distribution Parameter Estimation with Real Data

We performed additional NEIM testing using sea echo reflectivity observations using datasets collected with the Fynmeet RCS measurement facility provided by the Defense, Peace, Safety, and Security Unit of the Council for Scientific and Industrial Research (CSIR) in Pretoria, South Africa. We also used datasets collected with the IPIX radar provided by McMaster University located in Hamilton, Ontario, Canada.

4.5.1 CSIR Fynmeet Radar 3 August 2006

For real sea clutter data, both the NEIM and CEFIM estimators performed similarly for the same datasets. As a result, we only provide comparisons using the NEIM. Similar results for the CEFIM method are provided in [18].

4.5.1.1 CSIR Fynmeet Radar

The ICKD parameter estimation methods were used to model sea echo reflectivity datasets collected by the Fynmeet Radar deployed at Measurement Station 3 in the Denvel Overberg Test Range facility in 2006 [27, 52]. The datasets were provided by the Defense, Peace, Safety, and Security Unit of the Council for Scientific and Industrial Research (CSIR) in Pretoria, South Africa. The radar used a 9 GHz RF center frequency, 100 ns pulse width, 5 kHz pulse repetition frequency and VV polarization. Table 4.4 provides information on the selected range bins, including environmental conditions. The sea surface dynamics must be accounted for when modeling real sea echo reflectivity, as they can affect the performance of both the moment and nonlinear curve fitting estimators. An in-depth analysis of the CSIR data is provided in [7], together with a method to simulate correlated coherent sea clutter that can capture the time-varying temporal characteristics of specified range bins.

Dataset Information	CFC17_010	CFC17_009	CFC17_001
Date	08/03/2006	08/03/2006	08/03/2006
Time	14:46:43	14:45:08	13:20:23
Number range cells	48	48	96
Starting range	7,000 m	5,000 m	3,000 m
Selected range bin (RB)	19	32	26, 58, 72
Range resolution	15 m	15 m	15 m
Range bin duration	59.9488 s	59.9636 s	32.7038 s
Total observations (sweep)	299,745	299,819	163,520
Antenna azimuth angle	93.95°	93.95°	165.5°
Antenna elevation angle	−0.48°	−0.49°	−1.06°
Wind speed (Instantaneous)	15 kn	15 kn	15.5 kn
Wind Gusts	26 kn	26 kn	29.2 kn
Wind direction	262.6°	262.3°	246.9°
Significant Wave height	2.38 m	2.37 m	2.22 m
Wave direction	141.3°	141.3°	134.5°

Table 4.4: CSIR Fynmeet Radar Dataset Information

For intensity model parameters, we need to investigate whether the time-varying spectra from the sea surface can affect estimation accuracy. This includes backscatter from the rough sea surface and surface waves Using empirical data, sea backscattering was modeled as the linear combination of Bragg, whitecap, and sea-spike scattering [25, 2, 53]. Bragg scattering results form resonate capillary waves that are modulated by longer duration gravity waves [26, 54]. The non-Bragg whitecap and sea-spike scattering is due to rough surface created by breaking waves. The whitecap can be very short in duration typically less the

200 ms, whereas the sea-spike can last for several seconds and does not decorrelate from pulse to pulse [2, 24].

Fig. 4.18(a) shows CSIR sea clutter intensity data from a single range bin with a non-Bragg spike component at about 19 s that decorrelates quickly and can affect the curve shape of the CCDF model. This can result in a poor fit of the ICKD tail as shown in Fig. 4.18(b). Fig. 4.19(a) shows the same data but with the non-Bragg spike replaced with data from neighboring cells; this is done in order to demonstrate the impact of sea-spikes when modeling the CCDF tail, as the better fit is demonstrated in Fig. 4.19(b).

The longer duration gravity waves are typically characterized by the height, velocity and periodicity of the waves. For radars that stare in range, this periodic behavior can cause a strong temporal modulation, thereby reducing the effective number of time samples [7, 55]. Fig. 4.20(a) demonstrates the long time intensity autocorrelation for range-bin 72 (RB 72) of the CSIR CFC17_001 dataset. Fig. 4.20(b) shows the IM, NCF, and NEIM estimated ICKD model distributions. As it can be seen, there is a poor data fit at the tail; this may be attributed to the reduced number of effective samples due to the strong temporal correlation [7].

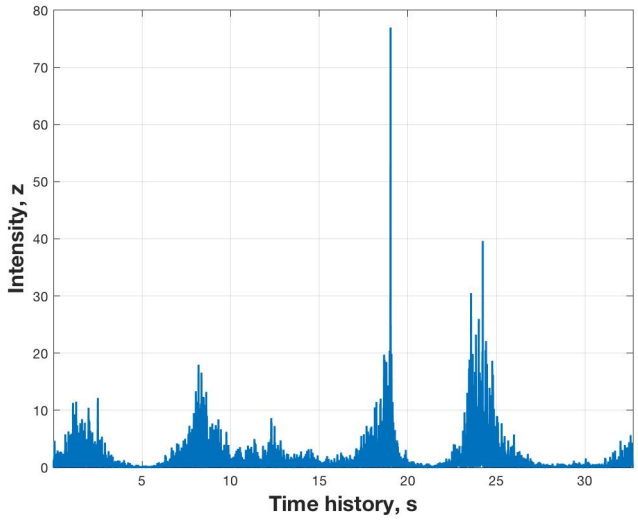

(a)

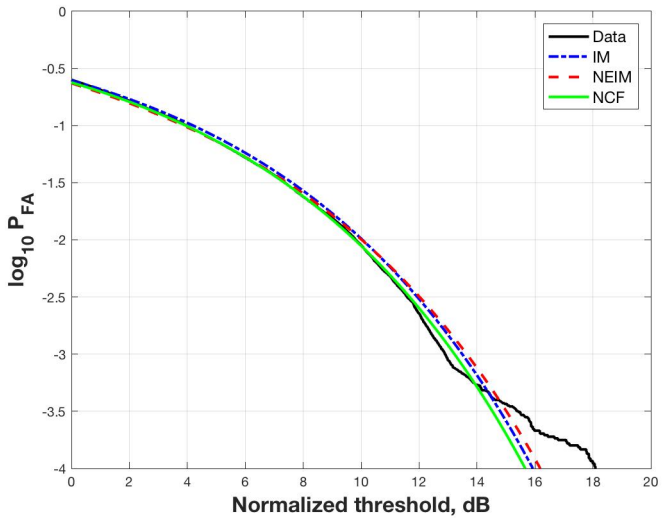

(b)

Fig. 4.18: CSIR CFC17_001 (RB 58) with Spike: (a) Time History Intensity Data, (b) Estimated P_{FA} with Spike.

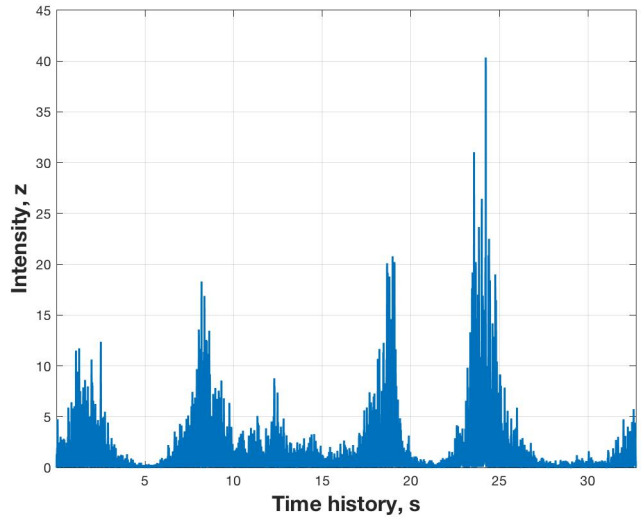

(a)

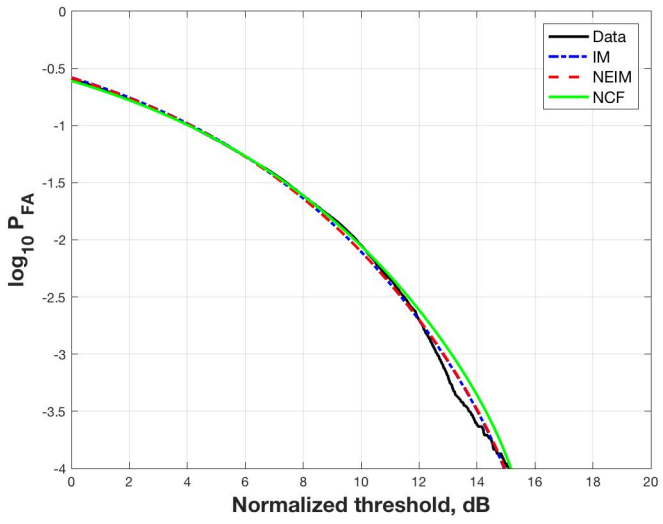

(b)

Fig. 4.19: CSIR Reflectivity CFC17_001 (RB 58) Suppressed Spike: (a) Time History Intensity Data, and (b) Estimated P_{FA}.

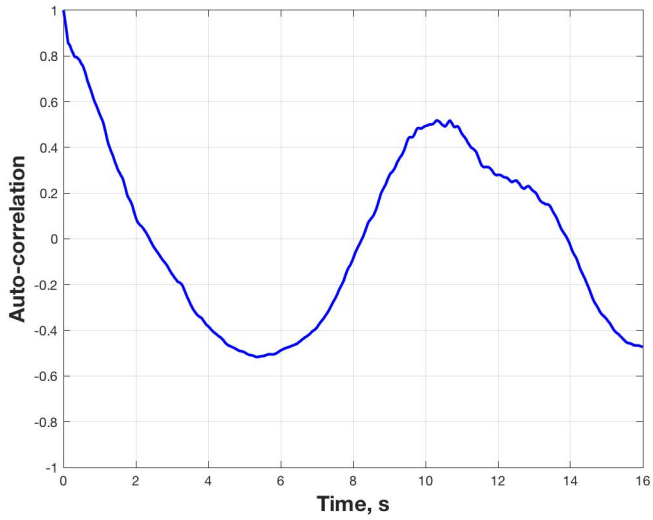

(a)

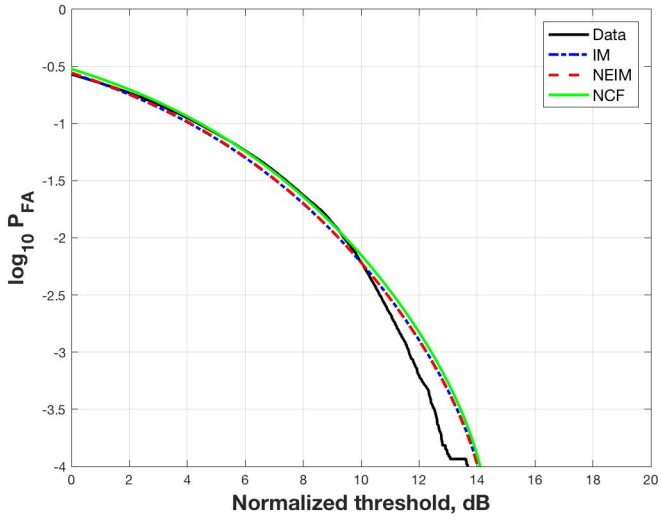

(b)

Fig. 4.20: CSIR Reflectivity CFC17_001 (RB 72) : (a) Intensity ACS , and (b) IM, NCF and NEIM Estimated Probability of False Alarm.

As the non-Bragg sea spike components affect the fit of the ICKD model, we concentrate on analyzing only specific types of datasets. For example, we do not consider data with horizontal polarization as the ICKD model was shown to fail at low grazing angles (less than 30°) [8, 9, 56]. Table 4.5 provides the estimated shape parameter $\hat{\nu}$, thermal noise power $\hat{p}_n$, and CNR from (4.8) using the IM, NCF, and NEIM methods. The corresponding P_{FA} curves provided in Fig. 4.21 through Fig. 4.23 demonstrate that the NEIM accuracy is comparable to that of the IM and NCF.

Range Bin	Estimation Method	$\hat{\nu}$	$\hat{p}_n$	CNR, dB
	IM	2.7006	0.2085	5.79
RB 19	NCF	3.1419	0.1211	8.61
	NEIM	2.4811	0.2413	4.97
	IM	1.2795	0.0146	18.28
RB 26	NCF	1.2684	0.0001	39.45
	NEIM	1.3106	0.0027	25.16
	IM	1.7624	0.0724	11.08
RB 32	NCF	1.8158	0.0466	13.10
	NEIM	1.9366	0.0276	15.47

Table 4.5: CSIR Fynmeet Radar Estimated Range Bins

The P_{FA} curves in Fig. 4.21 through Fig. 4.23 show good tail fits for the selected range bins while the CNR values in Table 4.5 indicate variability between the IM, NCF, and NEIM methods. To better understand this, we provide Fig. 4.24(a) which shows the estimated shape parameter $\hat{\nu}$ for all range bins in the CFC17_010 dataset that show reasonable agreement between the IM, NCF, and NEIM methods. However Fig. 4.24(b) shows a disparity in $\hat{p}_n$. The IM non-parametric spectral estimate increases with range, whereas

the noise estimates for the NCF and NEIM methods are obtained by minimizating (3.20). This is emphasized in Fig. 4.23 that shows excellent agreement of the P_{FA} curves for the methods tested. Note, however, that there is variability in the estimated $\hat{p}_n$ in Table 4.5. Fig. 4.24(a) and Fig. 4.24(b) show very good agreement between the NCF and the computational efficient NEIM.

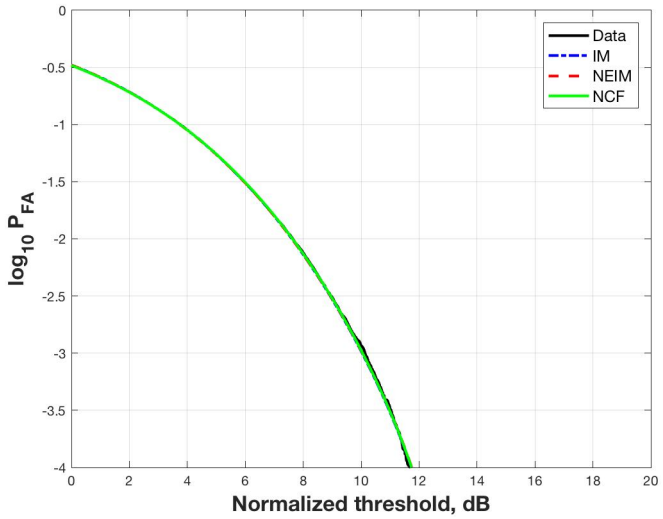

Fig. 4.21: IM, NCF and NEIM Estimated P_{FA}, CFC17_010 (RB 19).

Sea clutter time-varying spectral components can affect estimation accuracy [57, 58, 59, 31, 60, 61]. It was shown in [62] that time-variation caused different P_{FA} values between measured and modeled sea clutter. They also cause non-Gaussian amplitude statistics near the spectrum edges resulting in spiky ICKD estimates. In order to compare the performance of the new estimators with the IM under this scenario, we re-produced some P_{FA} results in Watts paper [7]. Specifically, we used the averaged spectrogram time-frequency representation (TFR) based approach in [7] to estimate the noise power for the IM before using it to estimate the shape in (3.5) and scale in (3.6). In our implementation of the spectrogram (short-time Fourier transform magnitude squared), a length 512 fast Fourier transforms (FFT) was used on data segmented using a Taylor window. The window pa-

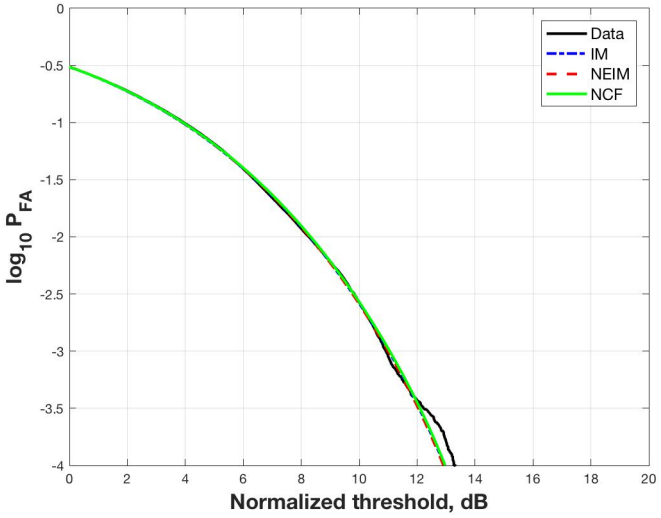

Fig. 4.22: IM, NCF and NEIM Estimated P_{FA}, CFC17_009 (RB 32).

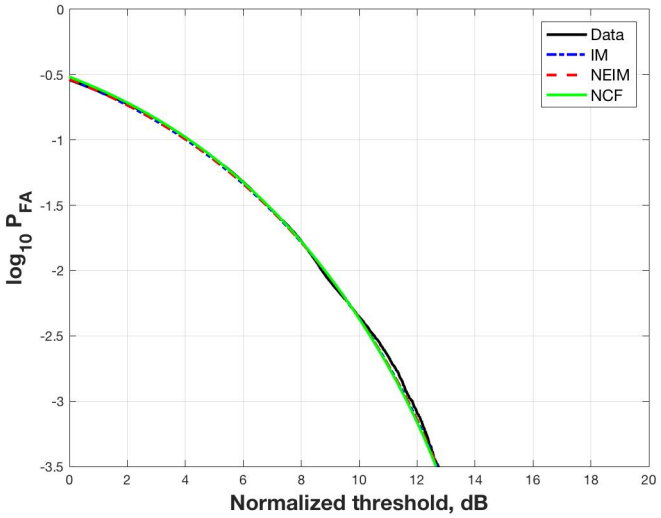

Fig. 4.23: IM, NCF and NEIM Estimated P_{FA}, CFC17_001 (RB 26).

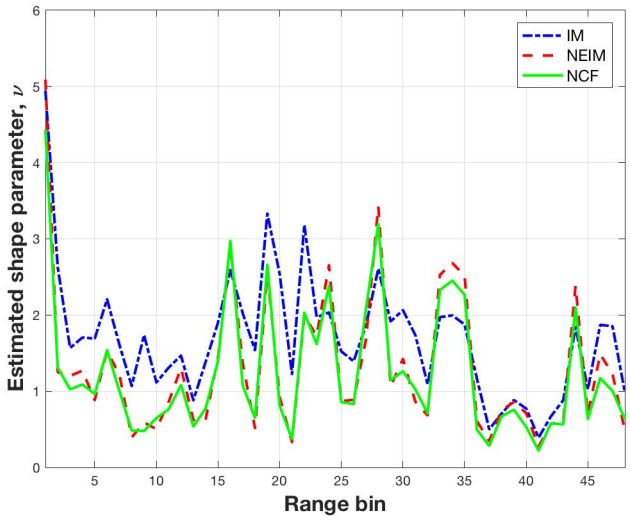

(a)

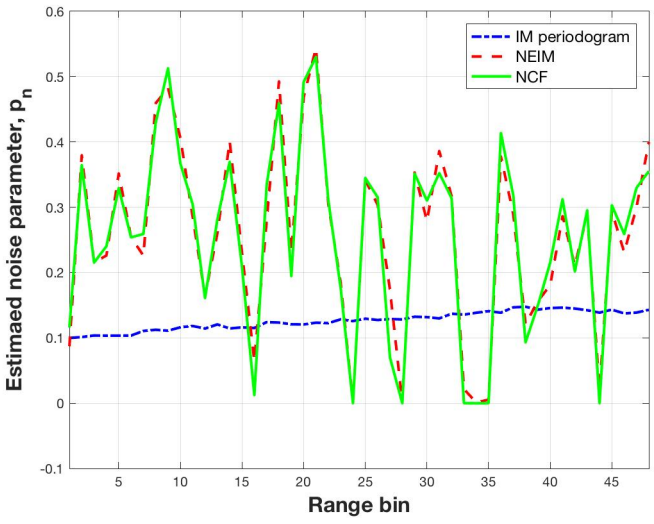

(b)

Fig. 4.24: (a) Shape Parameter $\hat{\nu}$ Estimation for All Range-bins in CFC17_010. (b) Thermal Noise Estimate $\hat{p}_n$ for All Range-bins in CFC17_010.

rameters were selected as $N_T = 64$ sample duration, $\bar{n} = 4$ nearly constant-level sidelobes adjacent to the mainlobe and -55 dB *SLL* (maximum sidelobe level relative to the mainlobe peak) [21]. The Taylor window is a variation of the Dolph-Chebyshev window used in [7]; it was used so as to reduce windowing discontinuities effects. Also, the average power of the window was normalized to select data within the same spectral region and to minimize noise power estimation bias [63]. Fig. 4.25(a) (Figure 2 in [7]) shows the spectrogram TFR of the CFC17_001 (RB 1) data. Fig. 4.25(b) (Figure 4 in [7]) shows the CNR that was estimated from the data using individual Doppler bins for use in the IM.

For our comparisons, we selected noisy data in the -2,500 Hz to -2,100 Hz region. Fig. 4.26(a) and Fig. 4.27(a) (similar to Figure 6 in [7]) show a data segment of duration 32.7 s (corresponding to 2,555 intensity data samples per Doppler bin); they were respectively obtained from the 0 Hz Doppler bin (with 32.34 dB CNR) and the 302.7 Hz Doppler bin (with 11.43 dB CNR) in Fig. 4.25(a).

The estimated models provide an adept fit for the two datasets, as shown in Fig. 4.26(b) and Fig. 4.27(b) for the IM, NCF and NEIM estimators; these figures are similar to those for the IM in Figure 9 in [7]. Note that the NCF performance is somewhat reduced for lower P_{FA} values for the 0 Hz Doppler bin data. The accuracy of the estimated model parameters for the 302.7 Hz Doppler bin data does not seem to be affected despite the reduced shape and CNR values. Table 4.6 provides the estimated ICKD shape and noise parameters for the IM, NCF, and NEIM methods used to generate the P_{FA} curves in Figs. 4.26(b) and 4.27(b).

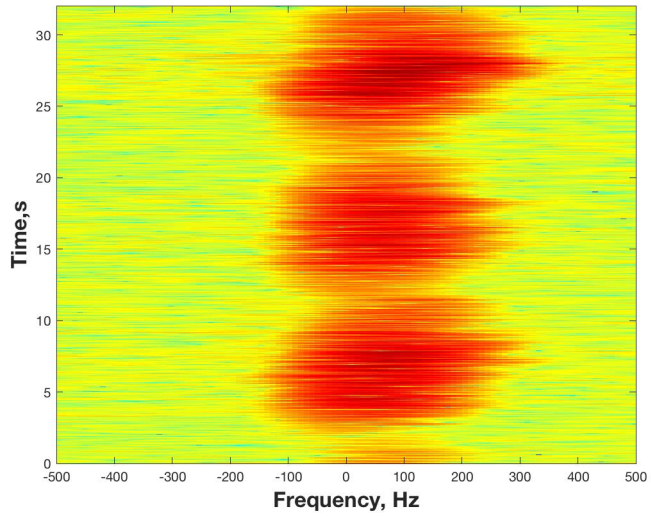

(a)

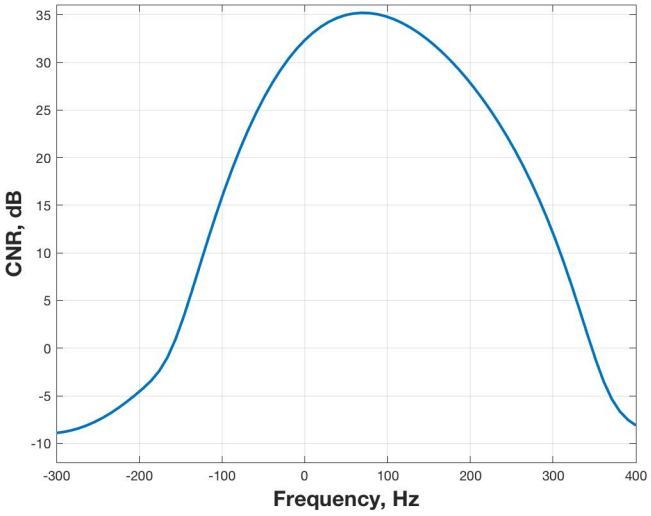

(b)

Fig. 4.25: CFC17_001 (RB 1): (a) Spectrogram TFR; (b) CNR for varying averaged Doppler spectra.

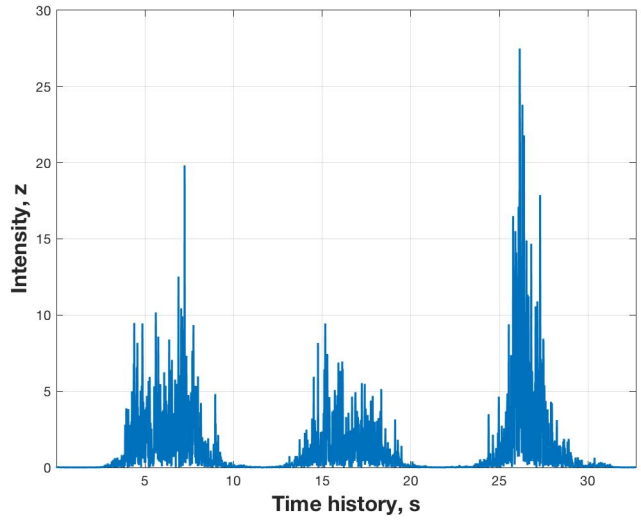

(a)

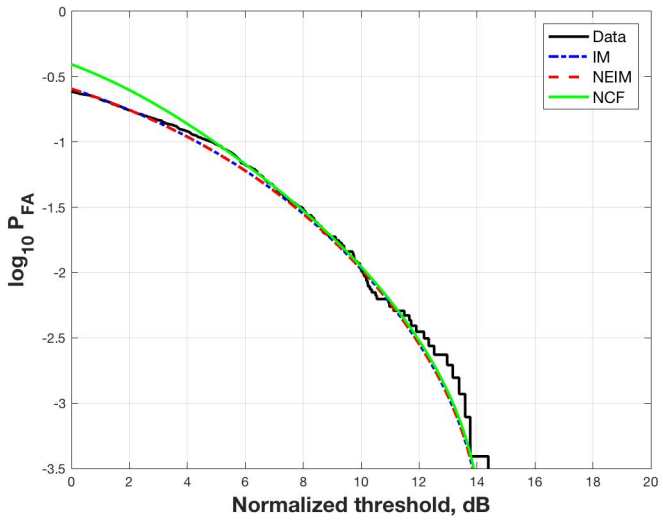

(b)

Fig. 4.26: CSIR reflectivity CFC17_001 (RB 1) : (a) Intensity Data in Doppler Bin 0.0 Hz with CNR = 32.3 dB. (b) IM, NCF and NEIM Estimated Probability of False Alarm.

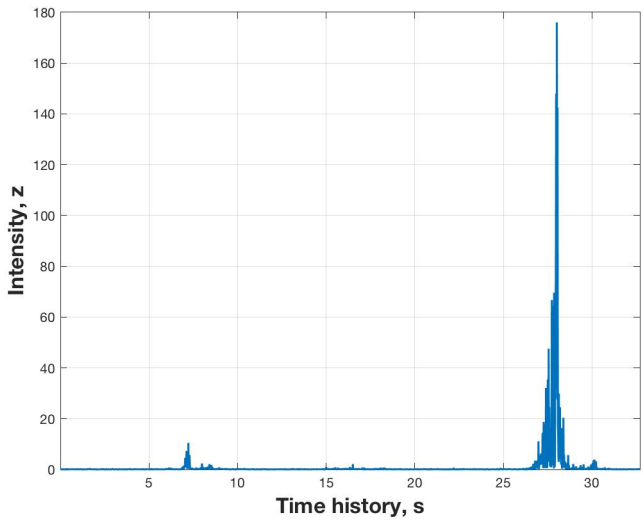

(a)

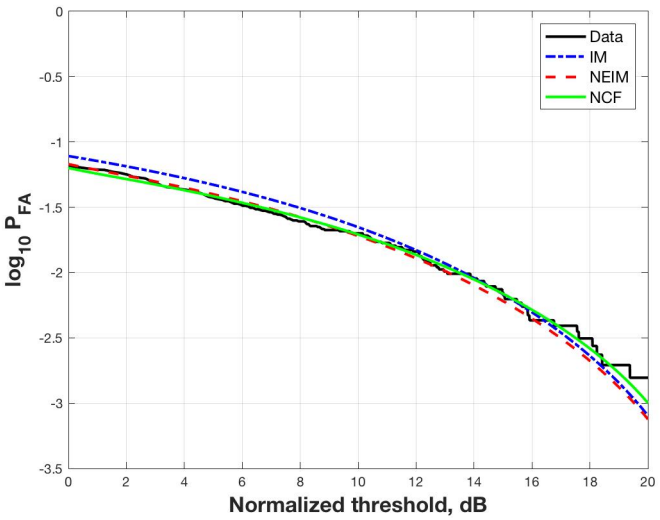

(b)

Fig. 4.27: CSIR Reflectivity CFC17_001 (RB 1) : (a) Intensity Data in Doppler Bin 302.7 Hz with CNR = 11.4 dB. (b) IM, NCF and NEIM Estimated Probability of False Alarm.

Doppler bin	Estimation Method	$\hat{v}$	$\hat{p}_n$	CNR, dB
0 Hz	IM	0.5424	0.0006	32.34
CFC17_001	NCF	0.4358	0.0068	21.62
RB 1	NEIM	0.5375	0.0009	30.24
302.7 Hz	IM	0.0322	0.0671	11.43
CFC17_001	NCF	0.0255	0.1034	9.38
RB 1	NEIM	0.0299	0.1001	9.53

Table 4.6: CSIR Fynmeet Radar Estimation Doppler Bins

4.5.2 McMaster University IPIX Radar, Grimsby Ontario 1998

For this analysis, we use datasets collected by the McMaster University Intelligent PIXel Processing Radar (IPIX) which was positioned in Grimsby Ontario (Latitude 43.2114° N, Longitude 79.5985° W), looking at lake Ontario from a height of 20 m [64, 58] . The Grimsby collection campaign occurred between 4 February and 4 March 1998 resulting in 222 10-bit, coherent, dual polarized, X-band datasets with different range resolutions (ρ). Additional IPIX system parameter are provided in APPENDIX C. The radar used the following parameters for the selected datasets: 9.39 GHz RF center frequency, 100 ns pulse width, 1 kHz pulse repetition frequency, with both VV and HH polarization.

4.5.2.1 Grimsby VV Polarization

This analysis uses two different resolution datasets collected on February 5, 1998. Range bins were specifically chosen to have different sea clutter spike and CNR levels. Table 4.7 provides the radar parameters for each range bin. Environmental data was not available for the wind and sea states. Table 4.8 provides the estimated shape parameter $\hat{\nu}$, thermal noise power $\hat{p}_n$, and the resulting estimated CNR for the IM, NCF, and NEIM methods. The corresponding P_{FA} curves are provided in Fig. 4.28. The plot shows that the accuracy of the new NEIM method is comparable to the established IM and NCF methods. For the IM result, we estimated the thermal noise power with the procedure described in Section 4.5.1 using the spectral region between -500 and -300 Hz on the centered Doppler spectrum.

Dataset	19980205_191043	19980205_184733
Date	02/05/1998	02/05/1998
Time	19:10:43	18:47:33
Polarization	VV	VV
Number range cells	28	28
Starting range	3600 m	3201 m
Selected range bin (RB)	3	20
Range resolution (ρ)	15 m	9 m
Range bin duration	60.0 s	60.0 s
Total observations (sweep)	60000	60000
Antenna azimuth angle	357.11°	45.11°
Antenna elevation angle	359.775°	359.769°

Table 4.7: IPIX Grimsby Scene Collection Information

Range Bin	ρ	Estimation method	$\hat{\nu}$	$\hat{p}_n$	CNR (in (4.8)) (dB)
RB 3	15 m	IM	0.163	0.187	6.38
		NCF	0.120	0.358	2.54
		NEIM	0.129	0.276	4.18
RB 20	9 m	IM	0.109	0.105	9.29
		NCF	0.088	0.139	7.92
		NEIM	0.102	0.137	7.99

Table 4.8: Estimated Sea Clutter Parameters From Real Sea Reflectivity Collection in Table 4.7.

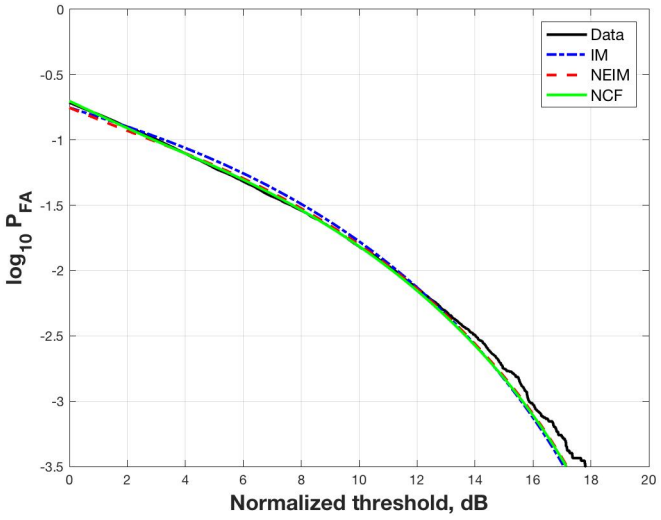

(a)

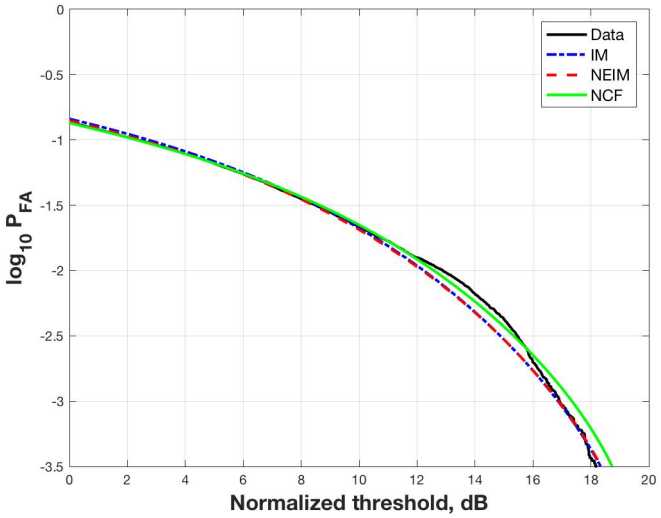

(b)

Fig. 4.28: IM, NCF, and NEIM Estimated Probability of False Alarm Using Grimsby Reflectivity Observations: (a) 19980205_191043 (RB 3), $\rho = 15\,\text{m}$, and (b) 19980205_184733 (RB 20), $\rho = 9\,\text{m}$.

4.5.2.2 Grimsby HH Polarization

As previously noted, the ICKD provides a well-matched model using real sea clutter samples with VV polarization but does not provide a matched fit using heavier-tail HH polarization [8]. To test (2.14), we use HH datasets obtained with the IPIX radar deployed at Grimsby CA staring into Lake Ontario at a hight of 20 m above the surface. Since this is a land-based radar, the grazing angles ϕ_{gr} are smaller resulting in heavier-tail or spikier clutter as captured with Equation (3.1), in that smaller values of ϕ_{gr} result in spikier clutter.

We compare two different methods to estimate the (2.14) parameters. In Section 3.8, we used the MATLAB function fminsearch that implements the 3-D Nelder-Mead search. Since this is a multi-dimension unconstrained search method, we use it to estimate the seven parameters of the KK distribution
$\theta_{KK} = [k_r, \nu_1, b_1, p_{n1}, \nu_2, b_2, p_{n2}]$,

$$\text{NCFK7: } p_{K7}(z) = (1-k_r)p_1(z;\nu_1,b_1,p_{n1}) + k_r p_2(z;\nu_2,b_2,p_{n2}). \tag{4.9}$$

We also test a similar method provided in [56] by using the same shape and thermal noise parameters for the two KK distributions with one difference in that we also fit the ratio parameter k_r, providing,

$$\text{NEIMK: } p_{K5}(z) = (1-k_r)p_1(z;\nu_1,b_1,p_{n1}) + k_r p_2(z;\nu_1,b_2,p_{n1}). \tag{4.10}$$

For this analysis, range bins were specifically chosen to have different sea clutter spike and CNR levels. Table 4.9 provides the radar parameters for each range bin. Environmental data was not available for the wind and sea states. Fig. 4.29(a) displays the time-history intensity data for the HH dataset 19980223_184853, (RB10) and Fig. 4.29(b) compares the fitted results for the NEIM, NCFK7 and NEIMK methods. Since this is an extreme heavy-tail example, we notice the NEIM and NEIMK do not provide a good fit to the tail. Fig. 4.30 displays the time-history intensity data and fitted results for the compared methods

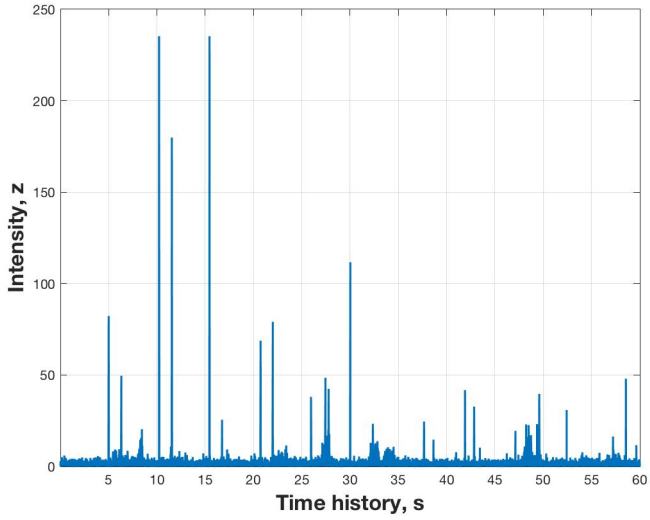

(a)

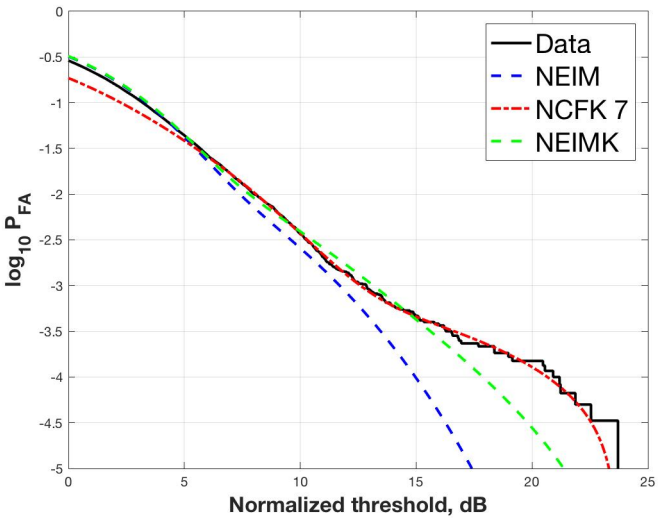

(b)

Fig. 4.29: Grimsby HH Polarization Heavy Tail Clutter Example, Dataset 19980223_184853, (RB10): (a) Spikey or Heavy Tail Time History Intensity Data, and (b) Heavy Tail Clutter Probability of False Alarm Estimation Results.

Dataset	19980223_184853	19980227_214328
Date	02/23/1998	02/27/1998
Time	18:48:53	21:43:28
Polarization	HH	HH
Number range cells	34	28
Starting range	3300 m	3660 m
Selected range bin (RB)	10	1
Range resolution (ρ)	3 m	9 m
Range bin duration	60.0 s	60.0 s
Total observations (sweep)	60000	60000
Antenna azimuth angle	0.11°	45.09°
Antenna elevation angle	359.78°	359.81°

Table 4.9: IPIX Grimsby Scene Collection Information

using the 19980227_214328 (RB1) dataset. We see in this result that both the NCFK7 and NEIMK provided a good match in the tail, whereas the NEIM does not. Table 4.9 provides the estimated parameters $\theta_{KK} = [k_r, \nu_1, b_1, p_{n1}, \nu_2, b_2, p_{n2}]$ for the tested methods for (RB 1) using dataset 19980223_184853.

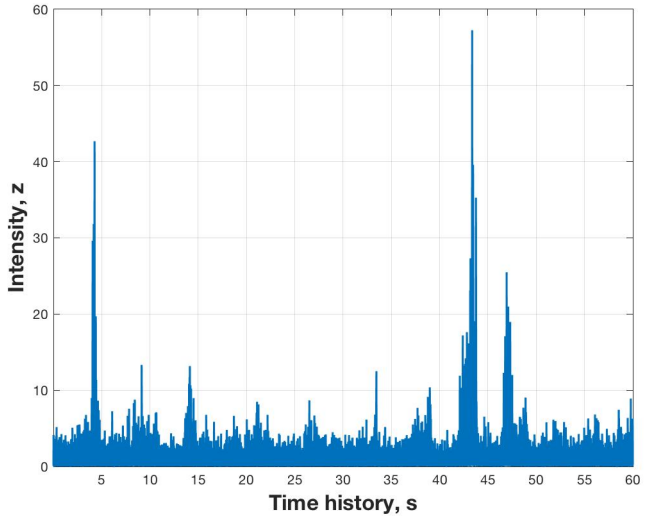

(a)

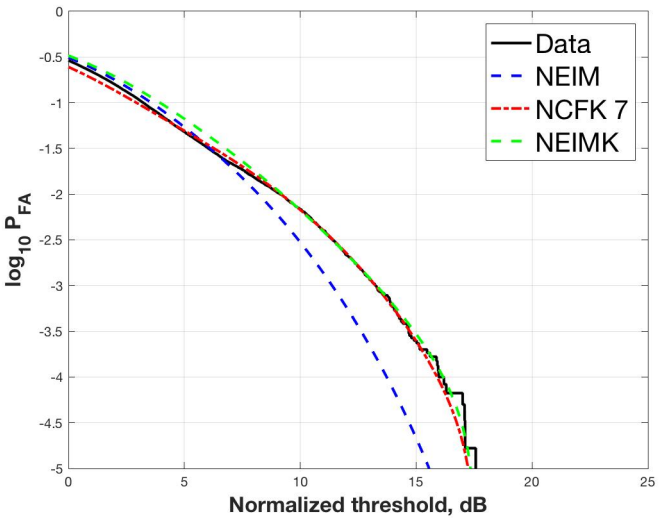

(b)

Fig. 4.30: Grimsby HH Polarization Heavy Tail Clutter Example, Dataset 19980227_214328, (RB1): (a) Spikey or Heavy Tail Time History Intensity Data, and (b) Heavy Tail Clutter Probability of False Alarm Estimation Results.

Estimation method	Shape $\hat{v}_1$	Scale $\hat{b}_1$	Noise $\hat{p}_{n1}$	$\hat{k}_r$	Shape $\hat{v}_2$	Scale $\hat{b}_2$	Noise $\hat{p}_{n2}$	MSE (dB)
NEIM	0.4143	0.9534	0.5654	0.0	N/A	N/A	N/A	-56.00
NCFK7	0.1502	0.3598	0.5108	0.0692	0.3817	0.4932	0.1683	-86.22
NEIMK	0.4143	0.9534	0.5654	0.1012	0.4143	0.2515	0.5654	-82.12

Table 4.10: Estimated Sea Clutter Parameters From Real Sea Reflectivity Collection, in Table 4.9.

4.5.3 DSTO Ingara Radar 15 February 1999

To model maritime surveillance radar performance for systems operating in Australian environmental conditions, the Australian government Defense Science and Technology Organization (DSTO), conducted sea trails ESRL 38/97 off the Northern Australian coastline in February 1999 [65]. To collect the reflectivity datasets and model the Anti-Submarine Warfare mode of the Elta EL/M 2022A(V)3 radar, the Surveillance Systems Division (SSD) Ingara airborne radar system was installed on a Beech King Air 350 aircraft.

Three sea clutter datasets were provided from Flight-19, 15 February 1999, when the radar was operated in its stare mode, with the data being range compressed with a conjugate chirp, providing 3297 samples at 1.5 meter resolution. We identified specific range-bins in two of the datasets by using the maximum echo return for each dataset and verifying the clutter data is free of radio-frequency interference (RFI) or spoking due mainly to the simultaneous operation of the weather radar of the aircraft and the Ingara radar [65]. We also verified by analysis of both the time history and spectral response data, that there were no strong targets captured in the sea echo reflectivity. The available scene collection and environmental information is provided in Table 4.11.

Our motivation for developing the combined NEIM parameter estimation procedure was to estimate the parameters for this dataset where we could not clearly identify a noise floor using the same spectral estimation procedure provided in [7]. This could be due to the lower CNR for the Ingara datasets or could related to the stare mode of the radar. We know [65] that the provided data is range compressed, but we have no information concerning the Doppler or azimuth time processing.

Fig. 4.31(a) shows the STFT for range-bin 11 of the DSTO R22985A dataset, and Fig. 4.31(b) is the averaged power spectral density. We do see what looks like a minimum

Dataset Information	R22985A	R22986
Date	02/15/1999	02/15/1999
Flight	19	19
Number range cells	3297	3297
Starting range	8,307 m	8,028 m
Selected range bin (RB)	11	51
Range resolution	1.5 m	1.5 m
Antenna azimuth angle	93.95°	93.95°
Antenna elevation angle	−1.893°	−1.957°
Wind speed (Instantaneous)	13 kn	13 kn
Wind Gusts	26 kn	26 kn
Wind direction	260.0°	260.0°
Significant Wave height	1 m	1 m
Wave direction	290.0°	290.0°

Table 4.11: DSTO Ingara Radar Dataset Information

value around -200 Hz, but without having all the processing parameters we cannot compensate for any process or filter gain. Fig 4.32 shows the tail fitted curves for the two data segments used, and the figures do show a good fit to the actual data. Table 4.12 provides the estimated parameters for the Ingara reflectivity datasets compared, and we had to use the estimated $\hat{p}_n$ obtained with the one parameter search in (4.2) to provided the estimated CNR.

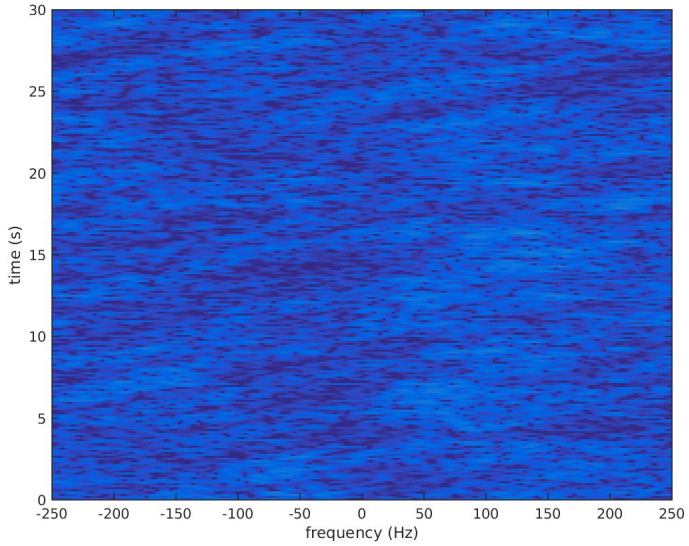

(a)

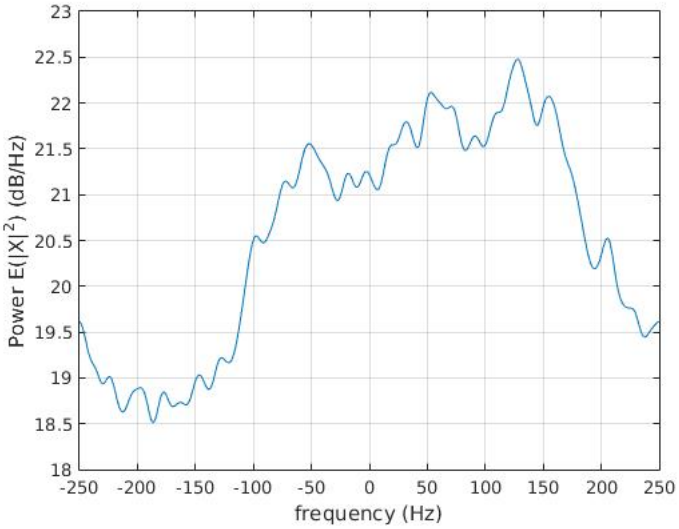

(b)

Fig. 4.31: (a) STFT of DSTO R22985A (RB 11), (b) Power Spectrum DSTO R22985A (RB 11).

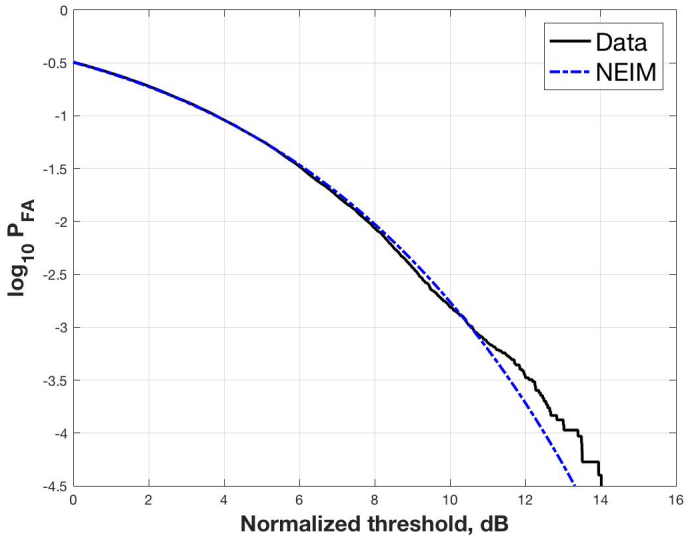

(a)

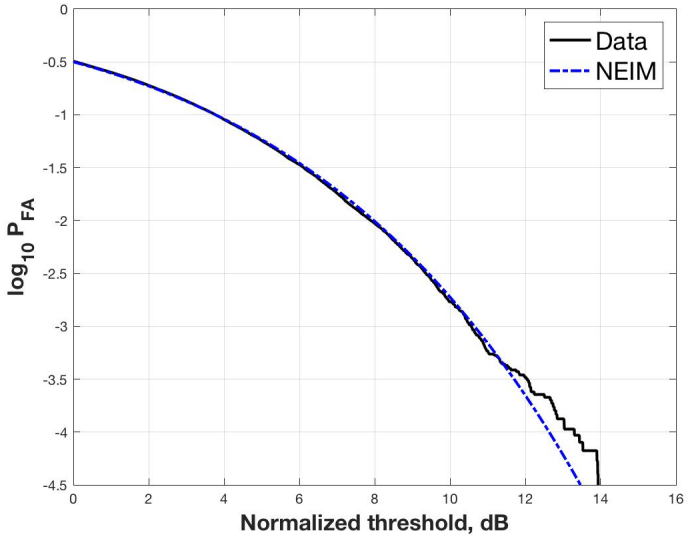

(b)

Fig. 4.32: (a) P_{FA} Using Estimated Parameters for R22985A, (RB 11); (b) P_{FA} Using Estimated Parameters for R22986, (RB 51).

Dataset	CNR (dB)	NEIM $\hat{v}$	NEIM $\hat{b}$	NEIM $\hat{p}_n$
R22985a (RB 11)	0.1549	1.0572	2.0773	0.4911
R22986 (RB 51)	4.7130	1.5553	2.0807	0.2525

Table 4.12: NEIM Parameter Estimation Using Ingara Sea Echo Reflectivity Data.

4.6 Results Discussion

4.6.1 Testing with Simulated Data

Since there are many algorithms available for nonlinear curve fitting or minimizing a MSE, we wanted to provided a comparison of a few methods that are easy to implement and do not require the use of derivatives. Our comparisons will contrast the parameter estimation accuracy and computation time performance between both 1-D and 3-D search methods, we will choose readily available methods to allow a good comparison.

4.6.2 1-D Search Methods

The three 1-D parameter search methods are compared in Fig. 4.2 through Fig. 4.4. We see in Fig. 4.2(b) that the three methods have almost identical thermal noise parameter estimation results, meaning the estimated shape and scale parameters derived by fitting the ICKD using the first two sample intensity moments $\hat{\mu}_1$, $\hat{\mu}_2$ with equations (4.5), (4.7) will have minimum error between the results. We see Fig. 4.3(a) compares the total number of function evaluations being the number of times the goodness of fit measure (4.1) was called. It is easy to see, the Mathews golden search is stable throughout the CNR range and completes with less evaluations than $\mathrm{fminbnd}$ but more evaluations than the Brent method. Fig. 4.3(b) shows the time performance and the results are understandable considering the number of function evaluations depicted in Fig. 4.3(a).

4.6.3 One and Three Dimension Search

In Section 4.4 we compare the 1-D and 3-D estimation methods with the intensity moments (IM) method with known thermal noise using (3.5) and (3.6). The plots compare

the estimated shape parameter $\hat{\nu}$, thermal noise parameter $\hat{p}_n$, computation time (CT) and curve fitting MSE for CNR in the range of -5 dB to 20 dB and shape parameters $\nu = [0.1,\ 0.5,\ 1.0]$. For all comparisons in the section, we are using MATLAB's $\mathrm{fminsearch}$ for the NCF method and $\mathrm{fminbnd}$ for the NEIM method. For the IM method we use (3.8) and (3.10) with known thermal noise p_n. We summarize the compared shape parameters below.

Section 4.4.1, ($\nu = 0.1$): Overall the NCF method provided better parameter estimation accuracy with the exception $\hat{\nu}$ diverages beginning at a CNR > 13 dB. The computation time (CT) performance is overall 30 times better using the NEIM and we are not comparing the IM since it is a closed form solution, not a curve fitted result.

Section 4.4.2, ($\nu = 0.5$): Overall the NCF method provided better parameter estimation accuracy. The CT performance varies between 60 and 15 times improved for the NEIM method where the difference is maximum at CNR -5 dB.

Section ??, ($\nu = 1.0$): Overall the NCF method provided better parameter estimation accuracy with the NEIM method improved below -2 dB. The CT performance varies between 70 and 10 times improved for the NEIM method where the difference is maximum at CNR -2 dB.

The results provided in Table 4.1 and Table 4.2 are as expected and we note Table 4.2 correctly captures how the estimated shape parameter $\hat{\nu} = 0.1$ diverges from the actual value for a CNR = 20 dB.

4.6.4 Simulation of Correlated Coherent Sea Clutter

In Section 4.4.6 we provide a test case using simulated correlated coherent (CC) clutter with the same statistical and temporal properties of the CSIR CFC17_001 (RB 1) dataset. The TFR comparison in Fig. 4.15 clearly shows that the simulated method [7] captures the

same non-stationarity depicted in the real CC dataset. The importance of this model cannot be overstated as the non-stationarity caused by the quickly changing sea surface continue to challenge the modeling of the sea surface for use in detection algorithms [7, 62].

4.6.5 Real Data Results

In this section we provide ICKD parameter estimation results using real sea echo reflectivity data provided with the CSIR Fynmeet, McMaster University IPIX and DSTO Ingara radars. Having characterized the estimation accuracy and and CT performance, we what to show that the 1-D search method will have comparable estimation accuracy performance with the IM method with known thermal noise and 3-D NCF. To that end, we provide different test cases to show 1-D search result.

Section 4.5.1, CSIR Fynmeet Radar 3 August 2006: The CSIR datasets were specifically chosen to show the estimation accuracy of the estimators across a range of ν while also displaying sea clutter phenomenon that result in poor CCDF fits in the tail of the distribution. For the simulated parameter estimation tests, we knew all the values we were simulating allowing us to provide direct comparisons with the estimated values. For the real datasets, we do not have any information concerning the ICKD parameters, therefor we use the fit to the CCDF or P_{FA} curves as a goodness measure. Also for all estimations using the IM method, we start by estimating the thermal noise using the non-parametric spectral estimation method provided in Section 3.3.2. We provide Fig. 4.18(b) through Fig. 4.20(b) to show the impacts of the sea surface on the returned clutter and how well the IM, NCF and NEIM methods fit the data sets. We next provide P_{FA} curves in Fig. 4.21 through Fig. 4.23 that show good tail fits for the selected range bins while the CNR values in Table 4.5 indicate variability between the IM, NCF, and NEIM methods. To better understand this vari-

ably in CNR, we provide Fig. 4.24(a) which shows the estimated shape parameter $\hat{\nu}$ for all range bins in the CFC17_010 dataset that show reasonable agreement between the IM, NCF, and NEIM methods. However Fig. 4.24(b) shows a disparity in $\hat{p}_n$. The IM non-parametric spectral estimate increases with range, whereas the noise estimates for the NCF and NEIM methods are obtained by minimizing (3.20). This is emphasized in Fig. 4.23 that shows excellent agreement of the P_{FA} curves for the methods tested. Note, however, that there is variability in the estimated $\hat{p}_n$ in Table 4.5. Fig. 4.24(a) and Fig. 4.24(b) show very good agreement between the NCF and the computationally efficient NEIM.

Section 4.5.2, McMaster University IPIX Radar, Grimsby Ontario 1998: For the IPIX Grimsby datasets, we chose specific datasets to compare the estimated ICKD parameters using VV polarization at different range resolutions ρ and datasets to test an initial implementation of a heavy-tail ICKD model using HH polarization. We see the same good parameter estimation accuracy using the tested IM, NCF and NEIM methods. Fig. 4.28 depicts the P_{FA} curves of the compared methods with specific values in Table 4.8. Fig. 4.29 provides an example of heavier-tail sea clutter and the need to models to accurately capture the parameters. Fig. 4.30(a) depicts the time history intensity data for a HH polarization collection, with Fig. 4.30(b) showing a good fit using both a seven parameter search estimating the parameters in (4.9) and a five parameter fit (4.10). Both of these methods provide reasonable results for this chosen dataset, however the results did not completely agree with the results in [56] which we believe to be a result of the Grimsby dataset having a very low grazing angle.

Section 4.5.3, DSTO Ingara Radar 15 February 1999: As we mentioned our motivation for developing the combined NEIM parameter estimation procedure was to es-

timate the parameters for this dataset where we could not clearly identify a noise floor using the same spectral estimation procedure provided in [7]. This could be due to the lower CNR for the Ingara datasets or could related to the stare mode of the radar. Fig. 4.31(b) depicts the averaged Doppler spectra for the DSTO R22985A (RB 11) dataset and it is easy to see, the noise floor is not as clearly defined as in Fig. 3.1(b). Fig. 4.32 clearly depicts that the NEIM method accurately models the two datasets, with the exception of the heavier tail occurring above the normalized threshold $\zeta \geq 11\,\text{dB}$.

Chapter 5

PARAMETER ESTIMATION USING 1-D NONLINEAR CURVE FITTING AND FRACTIONAL INTENSITY MOMENTS

5.1 Introduction

As demonstrated in [12], more accurate estimates of the intensity compound K-distribution (ICKD) sea clutter model parameters are obtained using the fractional intensity moment (FIM) approach (see Section 3.4) than the integer intensity moment (IM) approach (see Section 3.3). We thus propose a new estimation method that is similar to the noise-power estimation intensity moments (NEIM) approach, presented in Chapter 4, in that a thermal noise power estimate is iteratively computed to minimize the curve fitting mean-squared error (MSE). However, the clutter-to-noise ratio (CNR) estimated fractional intensity moment (CEFIM) method obtains the shape and scale parameter estimates using the FIM.

5.2 Description of Proposed Method

Similar to the iterative NEIM method, the simulated complementary cumulative density function (CCDF) $\Phi_Z\left(z_k; \hat{\boldsymbol{\theta}}^{(i)}\right)$ is used at the ith iteration to select M (out of L) tail CCDF points. These points are then used to compute the curve fitting MSE in (3.20). The noise power estimate $\hat{p}_n^{(i)}$ is obtained using the one-dimensional (1-D) search in Equation (4.2). This estimate is used in (3.11) to obtain the CNR estimate as

$$\hat{\eta}^{(i)} = \frac{\hat{\mu}_1 - \hat{p}_n^{(i)}}{\hat{p}_n^{(i)}} \tag{5.1}$$

where $\hat{\mu}_1$ is computed using(4.3). To obtain the shape parameter estimate, we use the relationship $\nu/\eta = \sqrt{\nu\,\nu_{\text{eff}}} - \nu$ from Equation (3.12) to replace ν_{eff} with the estimated η in

(3.14). The resulting estimated shape parameter is given by [12, 18]

$$\hat{\nu}^{(i)} = \frac{\rho(\rho+1)\hat{\eta}^{(i)}}{\left(\hat{\eta}^{(i)}+1\right)}\left(\frac{1-\rho\,\hat{\beta}_{\rho,1}/(\hat{\eta}^{(i)}+1)}{\hat{\alpha}_{\rho,1}-1-\rho}\right) \tag{5.2}$$

where $\hat{\beta}_{\rho,1}$ and $\hat{\alpha}_{\rho,1}$ are obtained using sample moment estimates $\hat{\mu}_{\rho+1}$, $\hat{\mu}_{\rho-1}$, and $\hat{\mu}_{\rho}$, computed using

$$\hat{\mu}_p = \frac{1}{N_s}\sum_{k=1}^{N_s} z_k^p. \tag{5.3}$$

The estimated scale parameter $\hat{b}^{(i)}$ is obtained using (4.6) and $\hat{\boldsymbol{\theta}}^{(i)} = [\hat{\nu}^{(i)}\ \hat{b}^{(i)}\ \hat{p}_n^{(i)}]$, is used to simulate the CCDF points $\Phi_Z^{\text{sim}}(z_m)$, $m = 1,\ldots,M$ for use in the next iteration. Iteration convergence is again based on pre-determined stopping criteria, and the final estimated $\hat{\boldsymbol{\theta}}$ is obtained after convergence.

Fig. 5.1 provides a flowchart of the CEFIM algorithm. For input, it requires the mean-normalized clutter intensity observations, the fractional moment ratios $\hat{\beta}_{\rho,1}$ and $\hat{\alpha}_{\rho,1}$, in Equation (3.13), the estimated first moment $\hat{\mu}_1$ in (4.3), and a range of values for the thermal noise power parameter $p_n \in R_p$. The steps of the algorithm are summarized with Algorithm 3. Similar to the NEIM, the stopping criteria of the iterative algorithm are based on the convergence of estimated thermal noise term $\hat{p}_n$. At the ith iteration, the difference in step size is $|\hat{p}_n^{(i+1)} - \hat{p}_n^{(i)}| < \varepsilon_X$, where ε_X is the minimum step size provided in Table 3.2. The optimization algorithm used in this method finds the minimum of a single-variable function over a fixed interval using the golden search method and parabolic interpolation [49]. In MATLAB, the function that implements this minimization is fminbnd.

Algorithm 3: Iteration Steps for CEFIM

- Input: Initial range of CNR η and range of CNR $\eta \in R_p$, mean-normalized intensity observations, z_k, $k = 1, \ldots, N_s$, minimum step size ε_X, $P_{\text{FA}} \geq 0.003$
- Using z_k, simulate $\Phi_Z^{\text{sim}}(z_\ell)$, $\ell = 1, \ldots, L$, using the intensity data provided; this is simulated as $\Phi_Z^{\text{sim}}(z_\ell) = \Pr(Z > z_\ell)$
- Obtain M (out of L), the number of tail CCDF points, as the number of intensity samples z_m such that $P_{\text{FA}} \geq 0.003$, where $P_{\text{FA}} = \Pr(Z > z_m) = \Phi_Z^{\text{sim}}(z_m)$
- At the ith iteration, $i = 0, \ldots, I_{\max}$, compute the tail M modeled CCDF points $\Phi_Z(z_m); \boldsymbol{\theta}^{(i)}$, $m = 1, \ldots, M$ using $\Phi_Z(z; \boldsymbol{\theta}) = \int_z^\infty p_Z(\zeta; \boldsymbol{\theta})\, d\zeta$, where $p_Z(\zeta; \boldsymbol{\theta})$ is the ICKD model PDF with parameter vector $\boldsymbol{\theta}$. Also, $\boldsymbol{\theta}^{(i)}$ are all allowable vector values of $\boldsymbol{\theta}$ over which the search is performed. This is accomplished by first obtaining the optimal $\hat{p}_n^{(i)}$ (4.2), computing CNR from $p_n^{(i)}$ using (5.1), then calculating the estimated shape $\hat{\nu}^{(i)}$ and scale $\hat{b}^{(i)}$ using (5.2) and (4.6)
- Compute the curve fitting MSE as $\mathscr{E}_Z(\boldsymbol{\theta}^{(i)}) = \frac{1}{M} \sum_{m=1}^{L-M} \left(\Phi_Z^{\text{sim}}(z_m) - \Phi_Z(z_m; \boldsymbol{\theta}^{(i)}) \right)^2$
- Find $\hat{p}_n^{(i)}$ that minimizes the curve fitting MSE, $\mathscr{E}_Z(p_n^{(i)}) = \frac{1}{M} \sum_{m=1}^{L-M} \left(\Phi_Z^{\text{sim}}\left(z_m\right) - \Phi_Z\left(z_m; p_n^{(i)}\right) \right)^2$
- Stopping criteria: for a given ε_X, stop iteration when $|\hat{p}_n^{(i+1)} - \hat{p}_n^{(i)}| < \varepsilon_X$

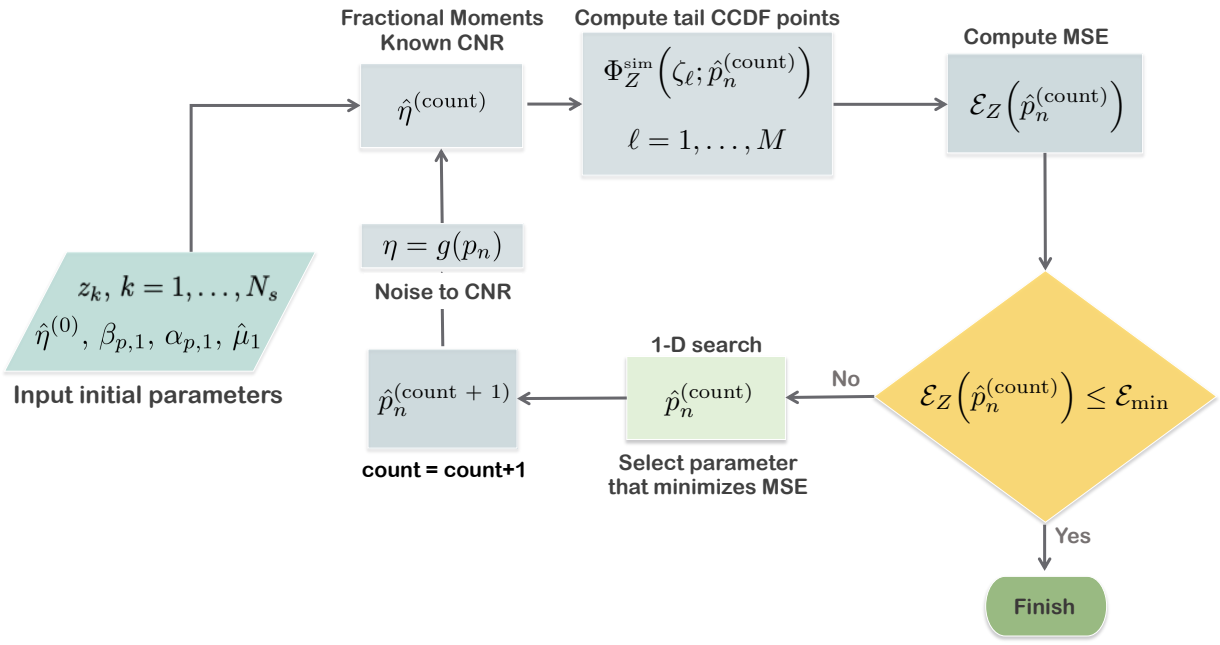

Fig. 5.1: CNR Estimated Fractional Intensity Moment (CEFIM), Flowchart Using a One Dimensional Search Algorithm.

5.3 Performance of CEFIM Method Using Simulated Sea Clutter Intensity

We compare the IM and FIM ICKD model parameter estimation methods with the NEIM and the new CEFIM method. We simulate clutter intensity observations following the simulation environment and algorithm parameters described in Section 3.7. We selected CNR values between 0 and 10 dB and a shape parameter value between 0.1 and 3. We selected L CCDF points such that the minimum probability of false alarm in (3.18) satisfies $\mathrm{P_{FA}} = \Phi(z_\ell) \geq 0.003$, $\ell = 1, \ldots, L$. This is important in order to avoid fitting the tail of the CCDF to regions where the clutter is very spiky with minimal samples and where the fit is poor [6, 19].

According to Reference [12], the fractional order $p = 0.5$ provides the minimum MSE with single-pulse data. It was also observed that negative CNR values resulted from large estimated values of the shape parameter. As we also observed this behavior, we provide minimum comparison of the CEFIM with the FIM method. We concentrate instead on comparing the parameter estimation performance between the intensity moment method with known thermal noise (IMN), the fractional moment method with known CNR (FMC), the three-dimensional (3-D) nonlinear curve fitting (NCF), the NEIM and the new CEFIM. Unless otherwise noted, we use N_s=10,000 samples and run 1,000 Monte Carlo simulations. For the FMC and CEFIM, single-pulse data was used and fractional order $p = 0.5$. All the simulated observations are also normalized by their mean.

Table 5.1 and Table 5.2 provide the estimated shape and thermal noise parameters, along with the variance and bias estimates for different shape and CNR levels. For the estimated bias measure, we use the squared difference $(E[\hat{\theta}] - \theta)^2$, where the parameter θ can correspond to the shape parameter ν, scale b or noise power p_n.

Simulated parameters			Estimation method	Estimation results			
Shape ν	Noise p_n	CNR (dB)		$E[\hat{\nu}]$	Var($\hat{\nu}$) (log10)	$(E[\hat{\nu}]-\nu)^2$ (log10)	Time (sec)
0.1	0.5000	0	IMN	0.1034	-3.59	-4.91	0.0000
			FMC	0.1017	-3.67	-5.49	0.0025
			NCF	0.1596	-1.58	-2.45	5.0252
			NEIM	0.1054	-3.37	-4.52	0.1463
			CEFIM	0.1024	-3.68	-5.21	0.2207
0.5	0.0909	10	IMN	0.5058	-2.73	-4.50	0.0000
			FMC	0.5024	-3.16	-5.27	0.0025
			NCF	0.5023	-1.95	-5.50	4.2329
			NEIM	0.5085	-2.21	-4.17	0.1012
			CEFIM	0.5024	-2.41	-5.40	0.1001
1.5	0.2303	5	IMN	1.5164	-1.74	-3.75	0.0000
			FMC	1.5101	-1.95	-4.28	0.0025
			NCF	1.5154	-0.44	-4.47	8.7020
			NEIM	1.5979	-0.68	-2.07	0.0871
			CEFIM	1.5704	-0.82	-2.39	0.0856

Table 5.1: Estimated Shape, Variance and Squared-bias for the IMN, FMC, NCF, NEIM and CEFIM Methods.

Simulated parameters			Estimation method	Estimation results			
Shape ν	Noise p_n	CNR (dB)		$E[\hat{p}_n]$ (log10)	Var($\hat{p}_n$) (log10)	$(E[\hat{p}_n] - p_n)^2$ (sec)	Time
0.1	0.5000	0	IMN	known	NA	NA	0.0000
			FMC	known	NA	NA	0.0025
			NCF	0.4695	-2.06	-3.03	5.0252
			NEIM	0.4969	-3.41	-5.01	0.1463
			CEFIM	0.4990	-3.64	-5.98	0.2207
0.5	0.0909	10	IMN	known	NA	NA	0.0000
			FMC	known	NA	NA	0.0025
			NCF	0.0920	-3.20	-5.80	4.2329
			NEIM	0.0901	-3.45	-6.41	0.1012
			CEFIM	0.0913	-4.07	-6.57	0.1001
1.5	0.2303	5	IMN	known	NA	NA	0.0000
			FMC	known	NA	NA	0.0025
			NCF	0.2490	-1.68	-4.11	8.7020
			NEIM	0.2300	-2.17	-3.98	0.0871
			CEFIM	0.2334	-2.30	-4.32	0.0856

Table 5.2: Estimated Thermal Noise p_n, Variance and Squared-bias for the IMN, FMC, NCF, NEIM and CEFIM Methods.

5.4 Performance of CEFIM Method Using Real Sea Clutter

We validated the CEFIM performance using sea clutter observations from a database provided by the Council for Scientific and Industrial Research (CSIR) [66]. The data was collected using the Fynmeet Radar deployed at Measurement Station 3 in the Overberg Test Range. The trials were conducted between 25 July and 4 August 2006 [27]. Table 5.3 provides information on the selected range bins, including environmental conditions. The sea surface dynamics must be accounted for when modeling real sea echo reflectivity, as they can affect the performance of both the moment and nonlinear curve fitting estimators. An in-depth analysis of the CSIR data is provided in [7], together with a method to simulate correlated coherent sea clutter that can capture the time-varying spectral characteristics of specified range bins.

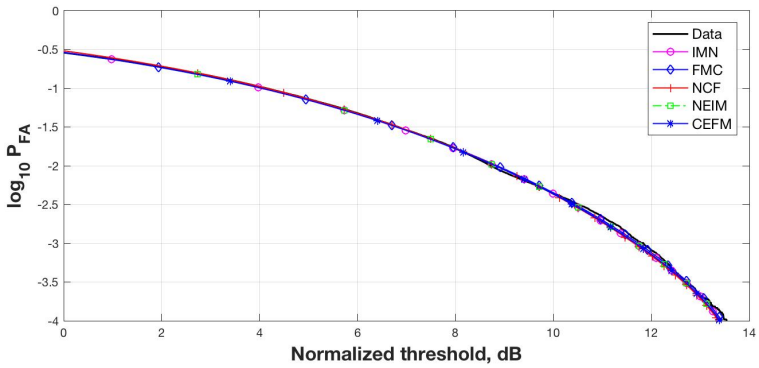

Fig. 5.2: IM, FMC, NEIM and CEFIM Estimated Probability of False Alarm Using CSIR Sea Clutter Observations CFC17_001 (RB 26).

Dataset Information	CFC17_010	CFC17_001
Date	08/03/2006	08/03/2006
Time	14:46:43	13:20:23
Number range cells	48	96
Starting range	7,000 m	3,000 m
Selected range bin (RB)	19	2, 26
Range resolution	15 m	15 m
Range bin duration	59.9488 s	32.7038 s
Total observations (sweep)	299,745	163,520
Antenna azimuth angle	93.95°	165.5°
Antenna elevation angle	−0.48°	−1.06°
Wind speed (Instantaneous)	15 kn	15.5 kn
Wind Gusts	26 kn	29.2 kn
Wind direction	262.6°	246.9°
Significant Wave height	2.38 m	2.22 m
Wave direction	141.3°	134.5°

Table 5.3: CSIR Fynmeet Radar Dataset Information

Table 5.4 provides the estimated shape parameter $\hat{\nu}$, thermal noise power $\hat{p}_n$, and the resulting estimated CNR for the IMN, FMC, NCF, NEIM and CEFIM methods. The corresponding P_{FA} curves are provided in Figure 5.2, where the accuracy of the NEIM and CEFIM methods is comparable to that of the IMN and NCF methods. For the IMN and FMC results, we estimated the thermal noise power using the time-averaging spectral estimation method in [7].

Dataset Range Bin	Estimation method	$\hat{\nu}$	$\hat{p}_n$	CNR ((4.8)) (dB)	MSE ((3.20)) (dB)
RB 2	IMN	0.356	0.014	18.53	-67.86
	FMC	0.337	0.014	18.53	-73.83
	NCF	0.304	0.005	23.18	-75.47
	NEIM	0.358	0.011	19.59	-68.33
	CEFIM	0.331	0.017	17.54	-74.58
RB 26	IMN	1.279	0.015	18.28	-62.46
	FMC	1.240	0.015	18.28	-63.84
	NCF	1.379	0.035	14.34	-72.06
	NEIM	1.311	0.002	26.36	-63.06
	CEFIM	1.277	0.003	25.66	-64.28
RB 19	IMN	3.332	0.121	8.62	-65.46
	FMC	3.441	0.121	8.62	-66.66
	NCF	3.142	0.121	8.60	-63.85
	NEIM	2.478	0.241	4.96	-68.28
	CEFIM	2.354	0.266	4.41	-78.43

Table 5.4: Estimated Sea Clutter Parameters for CSIR Datasets.

5.5 Results Discussion

It is expected that the CEFIM estimation method will have similar performance when compared to the NEIM.

5.5.1 Testing with Simulated Data

We see in Table 5.1 and Table 5.2 we see the variance and squared-bias of the estimated shape $\hat{\nu}$ and thermal noise $\hat{p}_n$ values are improved for the CEFIM estimator for all tested levels. Also, the CEFIM has overall lower computation time (CT) for the curve fitting methods with the exception of the $\nu = 0.1, p_n = 0.5$ test case.

5.5.2 Real Data Results

We validate the CEFIM performance using the CSIR datasets in Table 5.3. We see very good agreement between all compared methods in the P_{FA} curves provided in Figure 5.2. Table 5.4 provides the estimation results for the compared methods and see the MSE is lowest for the NCF and CEFIM methods. This is a good result because we can obtain almost identical results using the CEFIM without the CT burden of the 3-D search NCF method. We also see for (RB 19), the CEFIM had the best MSE performance.

Chapter 6

ESTIMATION ERROR ANALYSIS

6.1 Variance Analysis and the Cramér Rao Lower Bound

As demonstrated in [18], both the IM and FIM based estimators of the ICKD model parameters provide consistent estimation error performance, even for smaller sample sizes, when an accurate thermal noise estimate is available. Note that, according to [67], moment-based estimators are asymptotically consistent and asymptotically unbiased. As the new NEIM and CEFIM estimators use the IM and FIM, respectively, to iteratively provide improved estimates, we want to investigate their asymptotic estimation error performance. This is performed by numerically computing the CRLB of the shape parameter estimate that provides a lower bound on the variance of unbiased shape estimates. Since there is no closed form solution of the CKD PDF in (2.10), we use numerical methods to calculate the CRLB of the shape parameter estimate as [68]

$$\mathrm{CRLB}(\nu) = \frac{1}{N_s \int_0^\infty \left(\frac{\partial}{\partial \nu} \left(\ln p_Z(z) \right) \right)^2 p_Z(z)\, dz}. \tag{6.1}$$

Note that the CRLB for the shape parameter does not depend on the scale parameter [68].

We numerically computed the CRLB in (6.1) and compared it to the sample variance of the shape parameter estimates obtained from the LIM, NCF, and the new NEIM and CEFIM estimators. The comparison for $\nu = 1$ and varying CNR is provided in Fig. 6.1(a); these results were obtained using $N_s = 10,000$ intensity observation samples and 1,000 Monte Carlo simulations. For the LIM estimate, Equation (3.16) was used with ν_{eff} obtained from the estimated moments in (3.12). As it can be seen in this figure, the CEFIM and NCF

sample variances are closest to the CRLB for high CNR. In order to investigate whether the estimators are unbiased, Fig. 6.1(b) provides the squared-bias of the estimated shape parameter. This bias decreases with increasing CNR. The CEFIM has the lowest bias at high CNR. The lowest estimation MSE in Fig. 6.1(c) is achieved by the NCF; however, as this method requires a 3-D search, it is more computationally intensive when compared to the CEFIM. Similar results are provided in Fig. 6.2 for varying shape parameter ν and 5 dB CNR. The IM performance is also included in this figure in order to demonstrate that, even with 10,000 samples, its estimation accuracy is low. As mentioned in [12], the FIM estimator is also expected to perform poorly when estimating all three ICKD parameters without pulse-to-pulse integration.

For the comparisons in this section we first note that Brent's method [50] in Fig. 4.3(a) has the better function count and computation CT performance compared to the Mathews and $\mathrm{fminbnd}$ routines, therefore the results in this section for the NEIM and CEFIM methods were obtained using MATLAB'S mex API with the method provided by [51]. We also compared mex implementation of Nelder-Mead [48] used in the NCF but did not see any performance improvements, therefore we are using MATLAB'S $\mathrm{fminsearch}$ for all NCF comparisons.

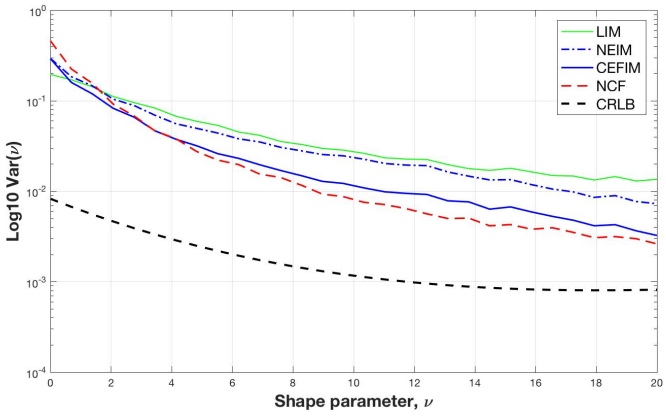

(a)

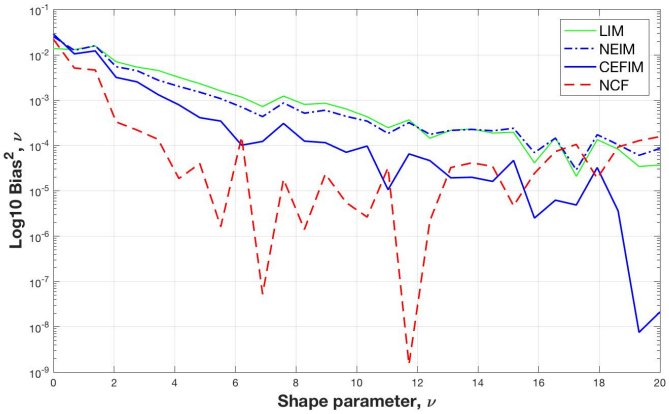

(b)

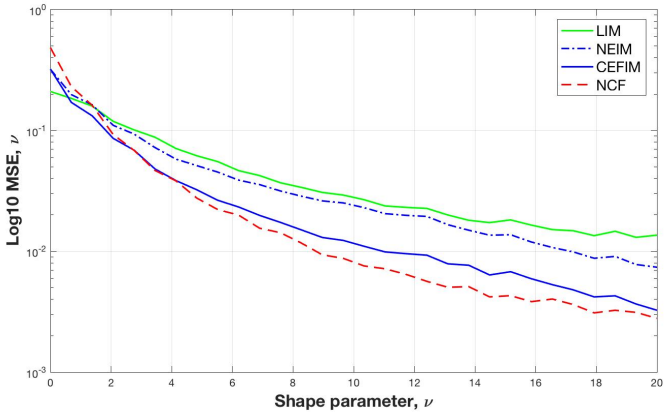

(c)

Fig. 6.1: Estimated Shape Parameter: (a) Variance; (b) Squared-bias; and (c) MSE for Varying CNR and $\nu = 1$.

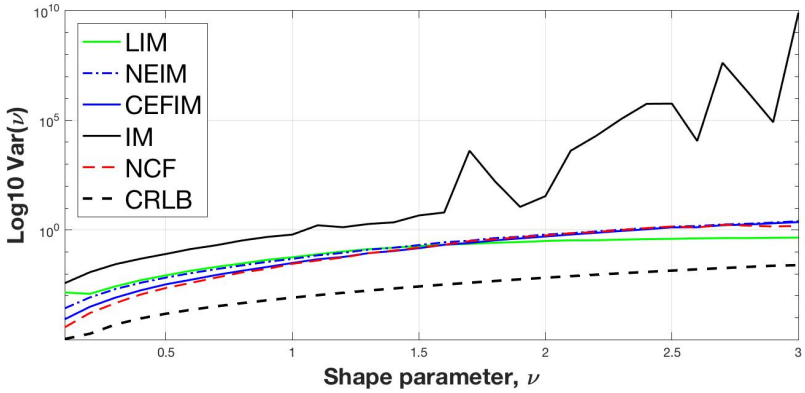

(a)

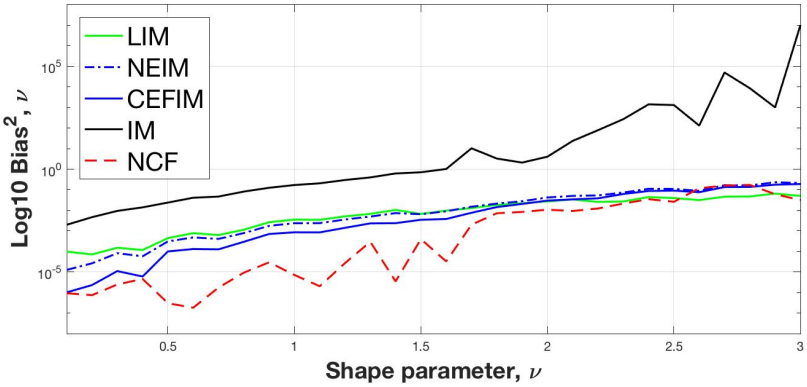

(b)

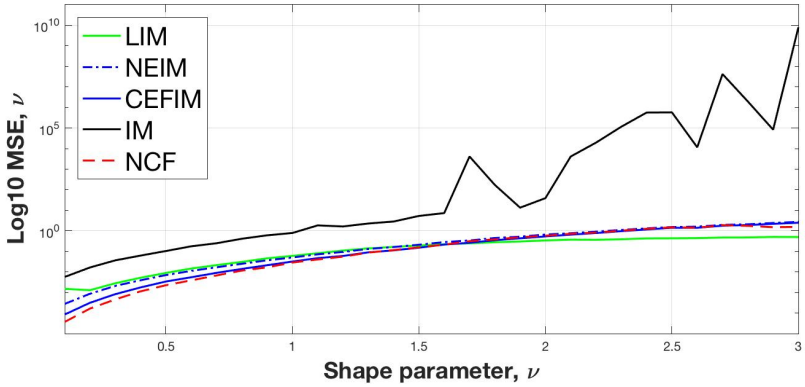

(c)

Fig. 6.2: Estimated Shape Parameter: (a) Variance; (b) Squared-bias; and (c) MSE for Varying ν and 5 dB CNR.

6.2 Mean-squared Error Performance Analysis

The MSE performance of the IM, NCF, LIM, NEIM and CEFIM estimators was compared using 1,000 Monte Carlo simulations. Using $\nu = 0.1$ and varying the thermal noise power as in (4.8), Fig. 6.3 shows the estimation MSE for the shape and noise power parameters and each method's computational time (CT). As expected, the IM is the fastest to compute but results in the largest overall MSE without the use of very large data vectors. Compared to the LIM and NCF, the new NEIM and CEFIM methods have the lowest CT. For this very small value of the shape parameter, the LIM does not perform as well as for $\nu = 1$ in Fig. 6.1(c). Also, both the NCF and CEFIM shape estimation performance decreases after about 12 dB CNR. The performance of all the methods is as expected when the same figures are provided for $\nu = 1.5$ in Fig. 6.4.

For the comparisons in this section we first note that Brent's method [50] in Fig. 4.3(a) has the better function count and computation CT performance compared to the Mathews and `fminbnd` routines, therefore the results in this section for the NEIM and CEFIM methods were obtained using MATLAB'S `mex` API with the method provided by [51]. We also compared `mex` implementation of Nelder-Mead [48] used in the NCF but did not see any performance improvements, therefore we are using MATLAB'S `fminsearch` for all NCF comparisons.

In Tables 6.1 and 6.2, additional performance results are provided for varying values of ν and CNR. In some cases, the number of samples were reduced to determine the effect of data record size on the MSE performance. We selected four shape parameter values, $\nu = 0.1,\ 0.5,\ 1,\ 1.5$.

Computational Time: Using a large number of samples, $N_s = 10,000$, the NCF CT (in green) is between 20 to 50 times larger than the NEIM and CEFIM CTs (in red); the difference in CT appears to increase with increasing ν and increasing CNR. The LIM CT

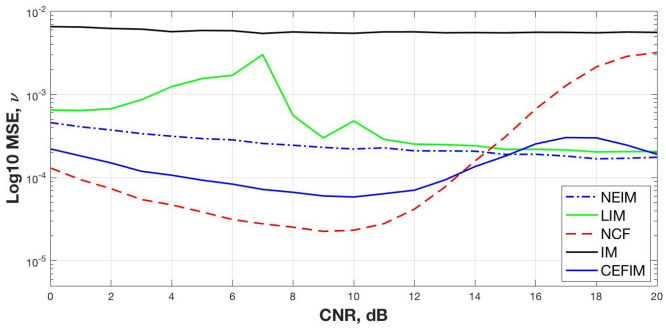

(a)

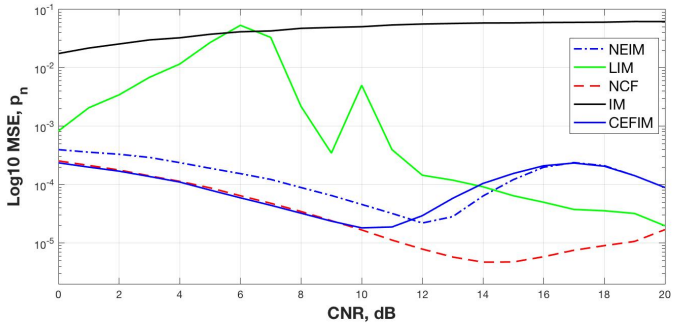

(b)

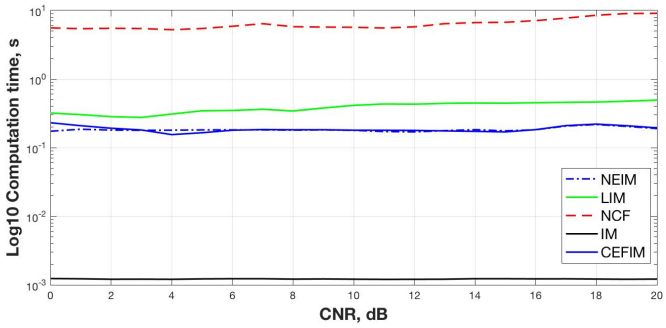

(c)

Fig. 6.3: Estimated Shape for Varying CNR and $\nu = 0.1$: (a) Shape MSE; (b) Thermal Noise Power MSE; (c) CT.

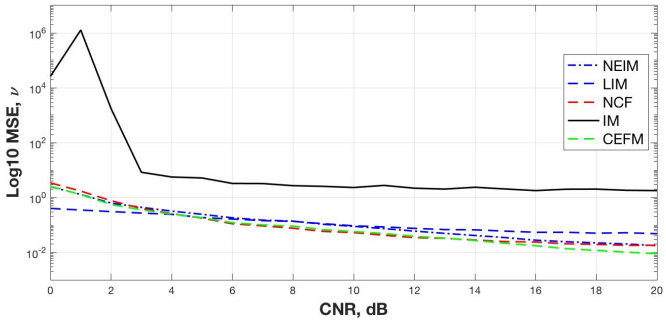

(a)

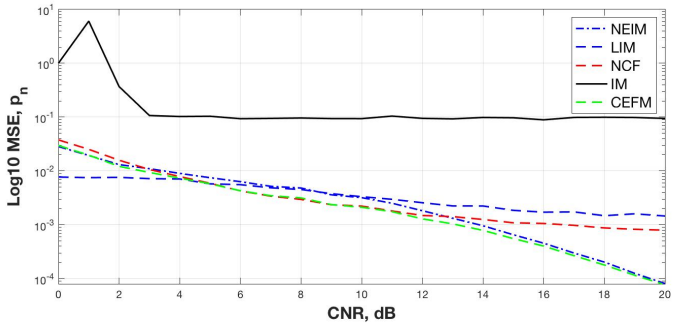

(b)

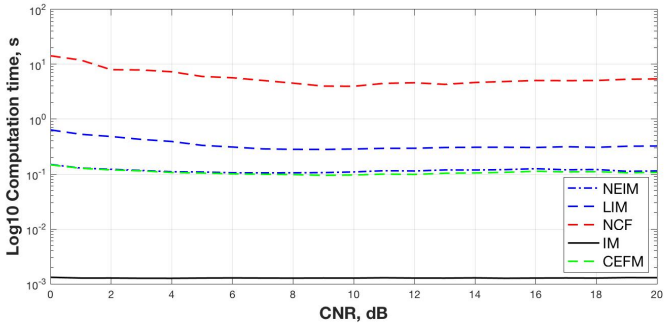

(c)

Fig. 6.4: Estimated Shape for Varying CNR and $\nu = 1.5$: (a) Shape MSE; (b) Thermal Noise Power MSE; (c) CT.

is about 1.5-3.5 times larger than the NEIM and CEFIM CTs. The NEIM and CEFIM CTs appear to be relatively robust to increases in ν and CNR values; the CTs remain around 0.1 to 0.2 s and slightly increase with decreasing ν, CNR and the sample number. Note that the NEIM and CEFIM CTs appear to be very similar.

MSE Estimation Accuracy: As the MSE is computed using semilog scale, the larger the negative number, the better the performance. For $N_s = 10,000$ and the ν values considered, the NCF method performs somewhat better than the new methods. The difference in shape estimation MSE performance varies from -3.90 to 0.02 for the NCF and -3.68 to 0.11 for the CEFIM. As with the CT, the CEFIM MSE performance is slightly better than the one for the NEIM, and they are both close in accuracy to the NCF. Note that the accuracy of the LIM appears to be dependent on the value of ν; the shape estimate MSE improves higher ν values and smaller number of samples. Similar results are observed for the noise power estimate MSE using the NEIM and CEFIM in that the accuracy improves for smaller ν values, larger sample sizes, and increasing CNR. The table also shows that overall, the CEFIM has the best noise power MSE, considering all simulated shape, CNR and samples sizes.

Simulation Parameters	**Estimation method**	**Estimation Results**		
		$\log_{10}$ MSE$_{\hat{\nu}}$	$\log_{10}$ MSE$_{\hat{p}_n}$	Time, s
$\nu = 0.1$	IM	-2.21	-1.76	0.0012
$p_n = 0.5$	NCF	-3.90	-3.61	**5.1746**
0 dB CNR	LIM	-3.18	-2.65	0.3116
$N_s = 10,000$	CEFIM	-3.68	-3.63	**0.2148**
	NEIM	-3.37	-3.41	**0.16**
$\nu = 0.1$	IM	-0.62	-0.43	0.0001
$p_n = 0.2403$	NCF	-3.05	-2.71	**5.6341**
5 dB CNR	LIM	-2.12	-1.79	0.2912
$N_s = 500$	CEFIM	-2.65	-2.80	**0.1493**
	NEIM	-2.27	-2.60	**0.155**
$\nu = 0.5$	IM	-1.04	-1.37	0.0012
$p_n = 0.0909$	NCF	-3.16	-4.14	**3.3571**
10 dB CNR	LIM	-2.32	-3.18	0.2809
$N_s = 10,000$	CEFIM	-2.87	-4.05	**0.1062**
	NEIM	-2.42	-3.45	**0.1042**

Table 6.1: Estimated Shape ν and Noise Power p_n, Estimation MSE and Computational Time for IM, NCF, LIM, CEFIM, NEIM Methods.

Simulation Parameters	**Estimation method**	**Estimation Results**		
		$\log_{10}$ MSE$_{\hat{\nu}}$	$\log_{10}$ MSE$_{\hat{p}_n}$	Time, s
$\nu = 1$	IM	-0.31	-1.19	0.0012
$p_n = 0.0099$	NCF	-2.58	-3.96	**4.0322**
20 dB CNR	LIM	-1.88	-3.33	0.3160
$N_s = 10,000$	CEFIM	-2.51	-4.40	**0.0922**
	NEIM	-2.13	-4.32	**0.0934**
$\nu = 1.5$	IM	0.54	-1.08	0.0012
$p_n = 0.2403$	NCF	-0.81	-2.27	**5.3770**
5 dB CNR	LIM	-0.75	-2.24	0.3160
$N_s = 10,000$	CEFIM	-0.80	-2.28	**0.0937**
	NEIM	-0.68	-2.17	**0.0897**
$\nu = 1.5$	IM	13.95	4.96	0.0002
$p_n = 0.2403$	NCF	0.02	-1.45	**5.8762**
5 dB CNR	LIM	-0.32	-1.93	0.5727
$N_s = 1,000$	CEFIM	0.11	-1.57	**0.1134**
	NEIM	0.22	-1.52	**0.115**

Table 6.2: Estimated Shape ν and Noise Power p_n, Estimation MSE and Computational Time for IM, NCF, LIM, CEFIM, NEIM Methods.

6.3 Results Discussion

6.3.1 Estimation Error Analysis

The estimation error comparisons in Section 6.1 and Section 6.2 are provided for the following methods: IM, LIM, CEFIM, NEIM, and NCF. All comparisons are accomplished using $N_s = 10,000$ samples and are averaged over 1,000 Monte-Carlo simulations.

Section 6.1, Cramér-Rao Lower Bound: The comparison for $\nu = 1$ and varying CNR is provided in Fig. 6.1(a). Fig. 6.1(b) provides the squared-bias of the estimated shape parameter. This bias decreases with increasing CNR. The CEFIM has the lowest bias at high CNR. The lowest estimation MSE in Fig. 6.1(c) is achieved by the NCF; however, as this method requires a 3-D search, it is more computationally intensive when compared to the CEFIM. Similar results are provided in Fig. 6.2 for varying shape parameter ν and 5 dB CNR. The IM performance is also included in this figure in order to demonstrate that, even with 10,000 samples, its estimation accuracy is low.

Section 6.2, Mean-squared Error Analysis: Fig. 6.3 shows the estimation MSE for the shape and noise power parameters and each method's computational time (CT). As expected, the IM is the fastest to compute but results in the largest overall MSE without the use of very large data vectors. Compared to the LIM and NCF, the new NEIM and CEFIM methods have the lowest CT. For this very small value of the shape parameter, the LIM does not perform as well as for $\nu = 1$ in Fig. 6.1(c). Also, both the NCF and CEFIM shape estimation performance decreases after about 12 dB CNR. The performance of all the methods is as expected when the same figures are provided for $\nu = 1.5$ in Fig. 6.4.

Chapter 7

CONCLUSION AND FUTURE WORK

7.1 Conclusion

Maritime environment conditions can affect the intensity of sea clutter reflections; thus, different statistical models are needed to characterize the various types of sea clutter in order to maintain high radar performance. Whereas time-varying models need to be used for rapidly-varying sea clutter at very low grazing angles [60, 61], the intensity-based compound K-distribution (ICKD) is a well-matched clutter amplitude distribution model with added thermal noise. In this paper, we considered a new computationally efficient and accurate curve fitting approach to estimate the ICKD model parameters. The method combines the intensity moments estimation method with fitting sea clutter intensity observations to a one-dimensional ICKD model. We also extended this model for use with fractional moments and demonstrated that the new approach is comparable in estimation performance, but more computationally efficient to the multidimensional Nelder-Mead unconstrained optimization method. This was shown with simulated and real sea clutter reflectivity observations. We also compare the estimation accuracy of the shape parameter with the numerically-computed Cramér-Rao lower bound.

7.2 Future Work

7.2.1 Covariance Matrix Estimation

Researchers have been studying both non-coherent and coherent target detection for many years for which the estimation of the sea clutter covariance matrix is necessary. The dynamic time changing nature of the sea surface makes accurate matrix estimation a difficult task [7] and it has recently been reported that compound Gaussian clutter such as the CKD, can provide a CFAR gain provided the underlying texture is correlated [20].

Considering the importance with target detection, additional work is necessary into more advanced covariance matrix estimators such as a space-time covariance matrix estimator provided in [61].

7.2.2 Temporal Correlation Impacts on CKD Parameter Estimation

A goal of real-time target detection is to estimate the needed clutter parameters a quickly as possible using a minimal number of data samples. To this end, we question how much data is necessary to achieve a given P_{FA}? In Fig. 3.5 we show that for a given CKD shape and CNR level, the minimum P_{FA} will decrease with increasing sample size; however the authors in [7] indicate that the strong correlation as depicted in Fig. 4.20 has resulted in the poor curve fit in the tail, caused by a reduction in the effective number of samples. This may suggest that reduced sample sizes are possible if we know the data has strong temporal correlation.

7.2.3 Non-stationary Sea Clutter

The non-stationary, or temporal variations of the sea clutter Doppler spectra has remained an active area of research [57, 58, 59, 31] and has been attributed to order of magnitude differences between the P_{FA} of measured and modeled sea clutter data [62]. In addition, the temporal variations cause non-Gaussian amplitude statistics near the spectrum edges resulting in spiky CKD estimates. In this work, we have estimated the non-Gaussian amplitude statistics using our proposed NEIM estimator, however additional work needs to be completed to understand aspects like sample size, correlation, Doppler frequency, CNR, spikiness attributes, and temporal impacts to accurate estimation results.

REFERENCES

[1] M. Skolnik, *Introduction to Radar Systems*, 3rd ed. McGraw-Hill, New York, NY, 2001.

[2] K. D. Ward, R. J. A. Tough, and S. Watts, *Sea Clutter: Scattering, the K Distribution and Radar Performance*, 2nd ed. Inst. Engineering and Technology, 2013.

[3] T. Nohara and S. Haykin, "Canadian east coast radar trials and the K-distribution," *IEE Proceedings F - Radar and Signal Processing*, vol. 138, no. 2, pp. 80–88, April 1991.

[4] P. Lombardo and C. J. Oliver, "Estimation of texture parameters in K-distributed clutter," *IEE Proceedings - Radar, Sonar and Navigation*, vol. 141, no. 4, pp. 196–204, August 1994.

[5] I. Antipov, "Statistical analysis of northern Australian coastline sea clutter data," http://dspace.dsto.defence.gov.au/dspace/handle/1947/3993, Surveillance Systems Division, Tech. Rep. DSTO-TR-1236, November 2001, accessed: 2016-11-24.

[6] A. Mezache, M. Sahed, and T. Laroussi, "K-distribution parameters estimation based on the Nelder-Mead algorithm in presence of thermal noise," in *International Conference on Advances in Computational Tools for Engineering Applications*, 2009, pp. 553–558.

[7] S. Watts, "Modeling and simulation of coherent sea clutter," *IEEE Transactions on Aerospace and Electronic Systems*, vol. 48, no. 4, pp. 3303–3317, October 2012.

[8] A. Farina, F. Gini, M. Greco, and L. Verrazzani, "High resolution sea clutter data: Statistical analysis of recorded live data," *IEE Proceedings - Radar, Sonar and Navigation*, vol. 144, no. 3, pp. 121–130, June 1997.

[9] D. J. Crisp, L. Rosenberg, N. J. Stacy, and Y. Dong, "Modelling X-band sea clutter with the K-distribution: Shape parameter variation," in *International Radar Conference*, 2009, pp. 1–6.

[10] S. Watts, "Radar detection prediction in K-distributed sea clutter and thermal noise," *IEEE Transactions on Aerospace and Electronic Systems*, vol. AES-23, no. 1, pp. 40–45, January 1987.

[11] S. Bocquet, "Parameter estimation for Pareto and K distributed clutter with noise," *IET Radar, Sonar & Navigation*, vol. 9, pp. 104–113, 2015.

[12] M. Sahed and A. Mezache, "Closed-form fractional-moment-based estimators for K-distributed clutter-plus-noise parameters," *IEEE Transactions on Aerospace and Electronic Systems*, vol. 53, no. 4, pp. 2094–2100, August 2017.

[13] M. Sahed, A. Mezache, and T. Laroussi, "A novel [z log(z)]-based closed form approach to parameter estimation of K-distributed clutter plus noise for radar detection," *IEEE Transactions on Aerospace and Electronic Systems*, vol. 51, pp. 492–505, 2015.

[14] D. Blacknell and R. J. A. Tough, "Parameter estimation for the K-distribution based on [z log(z)]," *IEE Proceedings - Radar, Sonar and Navigation*, vol. 148, no. 6, pp. 309–312, 2001.

[15] A. Mezache, M. Sahed, T. Laroussi, and D. Chikouche, "Two novel methods for estimating the compound K-clutter parameters in presence of thermal noise," *IET Radar, Sonar & Nav.*, vol. 5, pp. 934–942, 2011.

[16] J. Yang, Q. Zhou, C. W. Qu, and H. P. Hou, "Fast estimation of multilook K-distribution parameters via the least-squares nonlinear curve-fitting," in *IEEE International Conference on Signal Processing*, vol. 2, October 2012, pp. 856–860.

[17] P. Lombardo, C. J. Oliver, and R. J. A. Tough, "Effect of noise on order parameter estimation for K-distributed clutter," *IET Radar, Sonar & Nav*, vol. 142, pp. 33–40, 1995.

[18] J. Northrop and A. Papandreou-Suppappola, "Estimation of compound K-distribution modeling parameters of sea clutter with unknown thermal noise power," in *Asilomar Conference on Signals, Systems, and Computers*, 2018, pp. 2091–2095.

[19] ——, "Computationally efficient estimation of compound K-distribution sea clutter in thermal noise and its application to sea echo reflectivity observations," *IEEE Transactions on Aerospace and Electronic Systems,* submitted, March 2019.

[20] Y. Dong, "Optimal non-coherent detection in K-distributed clutter environment," in *International Conference on Radar*, September 2013, pp. 252–257.

[21] M. Skolnik, *Radar Handbook*, 2nd ed. McGraw-Hill, New York, NY, 1990.

[22] F. Nathanson, J. Reilly, and M. Cohen, *Radar Design Principles*, 2nd ed., ser. Signals and Comunication Technology. Mendham, NJ: Scitech Publishing, 1999.

[23] I. Antipov, "Simulation of sea clutter returns," Tactical Surveillance Systems Division, Tech. Rep. DSTO-TR-0679, June 1998.

[24] T. Lamont-Smith, K. D. Ward, and D. Walker, "A comparison of EM scattering results and radar sea clutter," in *International Radar Conference*, October 2002, pp. 439–443.

[25] D. Walker, "Experimentally motivated model for low grazing angle radar Doppler spectra of the sea surface," *IEE Proceedings - Radar, Sonar and Navigation*, vol. 147, no. 3, pp. 114–120, June 2000.

[26] ——, "Doppler modeling of radar sea clutter," *Radar, Sonar and Navigation, IEE Proceedings* -, vol. 148, no. 2, pp. 73–80, April 2001.

[27] H. J. de Wind, J. E. Cilliers, and P. L. Herselman, "Dataware: Sea clutter and small boat radar reflectivity databases [best of the web]," *IEEE Signal Processing Magazine*, vol. 27, no. 2, pp. 145–148, March 2010.

[28] K. D. Ward, C. J. Baker, and S. Watts, "Maritime surveillance radar. I. Radar scattering from the ocean surface," *IEE Proceedings F - Radar and Signal Processing*, vol. 137, no. 2, pp. 51–62, 1990.

[29] S. Watts, "Radar detection prediction in sea clutter using the compound K-distribution model," *IEE Proceedings F - Communications, Radar and Signal Processing*, vol. 132, no. 7, pp. 613–620, 1985.

[30] L. Rosenberg and S. Bocquet, "Non-coherent radar detection performance in medium grazing angle X-band sea-clutter," *IEEE Transactions on Aerospace and Electronic Systems*, vol. PP, no. 99, pp. 1–1, 2017.

[31] C. Sutour, J. Petitjean, S. Watts, J. M. Quellec, and S. Kemkemian, "Analysis of K-distributed sea clutter and thermal noise in high range and Doppler resolution radar data," in *2013 IEEE Radar Conference*, April 2013, pp. 1–4.

[32] Y. Dong and B. Haywood, "High grazing angle X-band sea clutter distributions," in *IET International Conference on Radar Systems*, October 2007, pp. 1–5.

[33] L. Rosenberg, D. J. Crisp, and N. J. Stacy, "Analysis of the KK-distribution with medium grazing angle sea-clutter," *IET Radar, Sonar Navigation*, vol. 4, no. 2, pp. 209–222, April 2010.

[34] D. Blacknell, "Comparison of parameter estimators for K-distribution," *IEE Proceedings - Radar, Sonar and Navigation*, vol. 141, no. 1, pp. 45–52, February 1994.

[35] G. Davidson, "Simulation of coherent sea clutter," *IET Radar, Sonar Navigation*, vol. 4, no. 2, pp. 168–177, April 2010.

[36] D. Iskander and A. Zoubir, "Estimation of the parameters of the K-distribution using higher order and fractional moments [radar clutter]," *IEEE Transactions on Aerospace and Electronic Systems*, vol. 35, no. 4, pp. 1453–1457, October 1999.

[37] D. Abraham and A. Lyons, "Reliable methods for estimating the K-distribution shape parameter," *IEEE Journal of Oceanic Engineering*, vol. 35, no. 2, pp. 288–302, April 2010.

[38] M. Sahed, A. Mezache, and T. Laroussi, "A novel [z log(z)]-based closed form approach to parameter estimation of K-distributed clutter plus noise for radar detection," *IEEE Transactions on Aerospace and Electronic Systems*, vol. 51, no. 1, pp. 492–505, January 2015.

[39] K. Ward, "Compound representation of high resolution sea clutter," *Electronics Letters*, vol. 17, no. 16, pp. 561–563, August 1981.

[40] F. J. Harris, "On the use of windows for harmonic analysis with the discrete Fourier transform," *Proceedings of the IEEE*, vol. 66, no. 1, pp. 51–83, 1978.

[41] W. Carrara, R. Goodman, and R. M. Majewski, *Spotlight Synthetic Aperture Radar: Signal Processing Algorithms*. Artech House, London, U.K, 1995.

[42] P. Thompson, D. E. Wahl, P. H. Eichel, D. C. Ghiglia, and C. V. Jakowatz, *Spotlight-Mode Synthetic Aperture Radar: A Signal Processing Approach*. Norwell, MA, USA: Kluwer Academic Publishers, 1996.

[43] J. C. Lagarias, J. A. Reeds, M. H. Wright, and P. E. Wright, "Convergence properties of the Nelder-Mead simplex method in low dimensions," *SIAM Journal of Optimization*, vol. 9, pp. 112–147, 1998.

[44] L. Devroye, *Non-Uniform Random Variate Generation*. Springer-Verlag New York Inc, 1986.

[45] J. H. Mathews and K. D. Fink, *Numerical Methods Using Matlab*. Upper Saddle River, NJ: Prentice Hall, Inc., 2004.

[46] E. Fan, "Global optimization of Lennard-Jones atomic clusters," Master's thesis, McMaster University, 2002.

[47] R. O'Neill, "Algorithm AS 47: Function minimization using a simplex procedure," *Journal of the Royal Statistical Society. Series C (Applied Statistics)*, vol. 20, no. 3, pp. 338–345, 1971.

[48] J. Burkardt, "Function minimization using a simplex procedure Matlab," http://people.sc.fsu.edu/jburkardt/m-src/asa047/asa047.html, accessed: June 2017.

[49] W. H. Press, S. A. Teukolsky, W. T. Vetterling, and B. P. Flannery, *Numerical Recipes: The Art of Scientific Computing*, 3rd ed. Cambridge University Press, 2007.

[50] R. Brent, *Algorithms for Minimization Without Derivatives*. Prentice-Hall, Englewood Cliffs, NJ, 1973.

[51] J. Burkardt, "Algorithms for minimization without derivatives with Matlab," http://people.sc.fsu.edu/jburkardt/m-src/brent/glomin.m, accessed: June 2017.

[52] P. L. Herselman and C. J. Baker, "Analysis of calibrated sea clutter and boat reflectivity data at C-and X-band in South African coastal waters," in *IET International Conference on Radar Systems*, October 2007, pp. 1–5.

[53] M. A. Ritchie, K. Woodbridge, and A. G. Stove, "Analysis of sea clutter distribution variation with Doppler using the compound K-distribution," in *IEEE Radar Conference*, May 2010, pp. 495–499.

[54] S. Haykin, R. Bakker, and B. Currie, "Uncovering nonlinear dynamics-the case study of sea clutter," *Proceedings of the IEEE*, vol. 90, no. 5, pp. 860–881, May 2002.

[55] H. J. Thiébaux and F. W. Zwiers, "The interpretation and estimation of effective sample size," *Journal of Climate and Applied Meteorology*, vol. 23, no. 5, pp. 800–811, 1984.

[56] L. Rosenberg, D. J. Crisp, and N. J. Stacy, "Analysis of the KK-distribution with X-band medium grazing angle sea-clutter," in *International Radar Conference "Surveillance for a Safer World"*, October 2009, pp. 1–6.

[57] S. Haykin and D. J. Thomson, "Signal detection in a nonstationary environment reformulated as an adaptive pattern classification problem," *Proceedings of the IEEE*, vol. 86, no. 11, pp. 2325–2344, November 1998.

[58] M. Greco, F. Gini, and M. Rangaswamy, "Non-stationarity analysis of real X-band clutter data at different resolutions," in *IEEE Conference on Radar*, April 2006, pp. 44–50.

[59] S. Watts, L. Rosenberg, S. Bocquet, and M. Ritchie, "Doppler spectra of medium grazing angle sea clutter; Part 1: Characterization," *IET Radar, Sonar Navigation*, vol. 10, no. 1, pp. 24–31, 2016.

[60] Y. Li, W. Moran, S. P. Sira, A. Papandreou-Suppappola, and D. Morrell, "Monte-Carlo based estimation methods for rapidly-varying sea clutter," in *Digital Signal Processing Workshop*, 2009, pp. 256–261.

[61] S. P. Ebenezer and A. Papandreou-Suppappola, "Low RCS target tracking in estimated rapidly-varying sea clutter using a Kronecker product approximation algorithm," *IEEE Journal of Selected Topics in Signal Processing*, vol. 9, pp. 1639–1649, 2015.

[62] M. Greco, P. Stinco, F. Gini, and M. Rangaswamy, "Impact of sea clutter nonstationarity on disturbance covariance matrix estimation and CFAR detector performance," *IEEE Transactions on Aerospace and Electronic Systems*, vol. 46, no. 3, pp. 1502–1513, July 2010.

[63] S. A. Tretter, *Introduction to Discrete-Time Signal Processing*. John Wiley & Sons, Incorporated, 1976.

[64] E. Conte, A. D. Maio, and C. Galdi, "Statistical analysis of real clutter at different range resolutions," *IEEE Transactions on Aerospace and Electronic Systems*, vol. 40, no. 3, pp. 903–918, July 2004.

[65] I. Antipov, "Statistical analysis of northern Australian coastline sea clutter data," http://dspace.dsto.defence.gov.au/dspace/handle/1947/3993, accessed: 2016-11-24.

[66] "Council for scientific and industrial research small boat detection," http://www.csir.co.za/small_boat_detection/, accessed: 2016-09-26.

[67] H. Cramér, *Mathematical Methods of Statistics*. Princeton, 1946.

[68] S. Kay and C. Xu, "CRLB via the characteristic function with application to the K-distribution," *IEEE Transactions on Aerospace and Electronic Systems*, vol. 44, no. 3, pp. 1161–1168, July 2008.

[69] "Fynmeet OTB 2006 Measurement Trial," http://www.csir.co.za/small-boat-detection/mtrials02.html, accessed: September 2016.

[70] S. Haykin, Ed., *Adaptive Radar Signal Processing*. Hoboken, New Jersey: Wiley-Interscience, 2007.

APPENDIX A

LIST OF SYMBOLS AND ABBREVIATIONS

Symbols:

$\Gamma(\cdot)$	Gamma function
$\Gamma(\cdot,\cdot)$	incomplete Gamma function
ΔR	delta range
ε_X	lower bound of the function step size
ε_F	lower bound of the function difference
ζ	normalized threshold
η	clutter-plus-noise ratio
θ_s	is the aspect angle with respect to swell direction
λ	radar wavelength
μ_1, μ_2, μ_3	first three intensity moments
μ_c,	pulse compression gain
ν, $\hat{\nu}$	shape parameter (estimated) for Gamma and K-distribution
ρ_μ	ratio of KK-distribution scale parameters
σ^0	area reflectivity (normalized clutter RCS)
$\Phi(\cdot)$	complementary cumulative distribution
ϕ_{gr}	grazing angle in degrees
A	sea clutter amplitude
A_c	radar resolved area
b, $\hat{b}$	scale parameter (estimated) for Gamma and K-distribution
dB	decibel
dBc	decibel relative to the carrier
$\mathscr{E}_Z(\cdot)$	goodness of fit measure
G	antenna gain
GHz	gigahertz
H	horizontal polarization
I	in-phase component out of quadrature detector
$I_{\max}$	maximum number of function iterations
k	Boltzmann's constant
k_{pol}	radar transmit and receive polarization parameter
k_r	distribution ratio parameter
kHz	kilohertz
km	kilometer

kW	kilowatt
L_μ	microwave losses
L_a	atmospheric and propagation loss
L	number of distribution points
M	number of MSE distribution points
m	meters
MHz	megahertz
µs	microseconds
N	number of pulses non-coherently integrated
ns	nanoseconds
$\bar{n}$	number of nearly constant-level sidelobe levels for the Taylor window
N_s	number of samples
N_T	number of Taylor weighting coefficients
p	fractional moment order
$p_A(A)$	PDF of the sea clutter amplitude
$p_A(A\|\cdot)$	conditional PDF of sea clutter amplitude
$p_Z(z)$	PDF of clutter intensity
$p_Z(z\|\cdot)$	conditional PDF of sea clutter intensity
p_c	mean clutter power
$P_{\text{FA}}(\zeta)$	probability of false alarm for normalized threshold ζ
p_n	thermal noise power
p_t	peak transmit power
Q	quadative-phase component out of quadrature detector
SLL	maximum Taylor window sidelobe level
V	vertical polarization
x	local mean clutter power
z, $\hat{z}$	clutter intensity (normalized)
$\langle z \rangle$	mean clutter intensity

Abbreviations:

1-D	one-dimensional
3-D	three-dimensional
CC	correlated coherent
CCDF	complementary cumulative distribution function
CD	compact disk
CDF	cumulative distribution function
CEFIM	clutter-to-noise ratio estimated fractional intensity moment
CRLB	Cramér-Rao lower bound
CNR	clutter-to-noise ratio
CSIR	Council for Scientific and Industrial Research
CT	computation time
CW	continuous wave
FFT	fast Fourier transform
FIM	fractional intensity moment
ICKD	intensity-based compound K-distribution
IDL	interactive data language
IFS	intermediate frequency sampler
IM	intensity moment
IPIX	Intelligent PIXel Processing Radar
LIM	log-based intensity moment
MC	Monte-Carlo
MSE	mean-squared error
NCF	nonlinear curve fitting
NEIM	noise-power estimation intensity moment
NM	Nelder-Mead
RCS	radar cross section
rpm	revolutions per minute
ROC	receiver operating characteristic
STFT	short-time Fourier transform
TFR	time-frequency representation
TWT	traveling-wave tube

APPENDIX B

DESCRIPTION OF FYNMEET RADAR

The CSIR Fynmeet dynamic Radar Cross Section (RCS) measurement facility is a calibrated, coherent, staring, pulsed radar system that was deployed along the coast of South Africa at Measurement Station 3 in the Overberg Test Range [52] to conduct small boat reflectivity and sea clutter trials, between 25 July and 4 August 2006 [27]. The system relevant parameters are depicted below, and can also be found in [69, 52].

1. *Transmitter*

    - Frequency range: 6.5-17.5 GHz
    - Peak power: 2 kW
    - PRF range: 0-30 kHz
    - Waveforms: 100 ns, 300 ns and 4 μs pulsed CW, fixed/pulse-to-pulse frequency agile
    - Agile bandwidth: 500 MHz pulse-to-pulse

2. *Receiver*

    - Dynamic range: 60 dB (instantaneous) / 120 dB (total)
    - Sensitivity: 0.1 m^2 at 10 km
    - Instrumented range: 200 m - 15 km
    - Range gates: 1 - 64; ΔR = 100 ns, 300 ns or 4 μs
    - Sampler type: Intermediate frequency sampler (IFS)
    - Encoding type: Quadrature
    - Image rejection: $\leq$ -41 dBc

3. *Antenna*

    - Type: Dual-offset reflector
    - Gain: $\geq$ 30 dB
    - Beamwidth: $\leq 2^\circ$ (3 dB beamwidth)
    - Sidelobes: $\leq$ -25 dB

APPENDIX C

DESCRIPTION OF IPIX RADAR SYSTEM

The McMaster University Intelligent PIXel Processing Radar (IPIX) System is a transportable experimental coherent, dual polarized, X-band system that provides datasets with configurable range resolutions. A brief description of the datasets and pertinent IPIX radar parameters is provided in References [54, 70] and the information below is a duplicate of Table 1.1 in Reference [70].

1. *Transmitter*
    - 8 kW peak power TWT
    - H or V polarization, switchable pulse-to-pulse
    - Frequency fixed (9.39 GHz) or agile over 8.9 to 9.4 GHz
    - Pulse width 20-200 ns (20 ns steps), 200 ns to 5000 ns (200 ns steps)
    - Pulse repetition frequency up to 20 kHz, limited by duty cycle (2%) or polarization switch (4 kHz)
    - Pulse repetition interval, configurable on a per-pulse basis
2. *Receiver*
    - Fully coherent reception
    - Two linear receivers: H or V on each receiver (usually one H and V for dual polarized reception)
    - Instantaneous dynamic range > 50 dB
    - 4 A/Ds: I and Q for each of two receivers
    - Range sampling up to 50 MHz
    - Full-bandwidth digitized data saved to disk, archived onto CD
3. *Antenna*
    - 2.4 m diameter parabolic dish
    - Pencil beam, beamwidth 0.9°
    - 44 dB gain
    - Sidelobes < -30 dB
    - Cross-polarization isolation
    - Computer controlled positioner
    - $-3°$ to 90° in elevation
    - Rotation through 360° in azimuth, 0 to 10 rpm
4. *General*
    - Radar system configuration and operation completely under computer control
    - User operates radar withing an IDL environment